The Dissertation Committee for Ki Hyun Kim Certifies that this is the approved version of the following dissertation:

Development of high-speed imaging techniques

for *C. elegans* nervous system studies

Committee:

Adela Ben-Yakar, Supervisor

Edward Yu

James Tunnell

Jonathan Pierce-Shimomura

Seth Bank

Development of high-speed imaging techniques
for *C. elegans* nervous system studies

by

Ki Hyun Kim, B.S.; B.S.E.; M.S.E.

Dissertation

Presented to the Faculty of the Graduate School of

The University of Texas at Austin

in Partial Fulfillment

of the Requirements

for the Degree of

Doctor of Philosophy

The University of Texas at Austin

May 2016

Dedication

To my family

Acknowledgements

I would like to express my gratitude to my advisor Dr. Adela Ben-Yakar for her enthusiasm, support, and guidance throughout my Ph.D. study. I would like to thank my fellow labmates for our productive discussions and their valuable advice for me. Last but not least, I would like to appreciate my family for their unconditional love and support for me.

Development of high-speed imaging techniques
for *C. elegans* nervous system studies

Ki Hyun Kim, Ph.D.

The University of Texas at Austin, 2016

Supervisor: Adela Ben-Yakar

We report high-speed imaging techniques for *C. elegans* nervous systems studies.

We introduce *C. elegans*, the main model organism in this dissertation, and neuroscientific and biomedical studies using *C. elegans* involving calcium imaging, nerve regeneration, and drug screening. We review technologies including confocal microscopy and microfluidic devices used in the neuroscientific and biomedical studies

We discuss development of a high-speed laser scanning confocal microscope capable of flexible control of imaging conditions, fast imaging speed, and large field-of-view. We provides the design principles used in the development of the confocal microscope including the optical, electrical, and software implementation, and the details of the confocal microscope we built based on the design principles. We present the performance characterization of the confocal microscope, then a few sample images obtained with the confocal microscope.

We present development of time-lapse volumetric confocal imaging of whole animal *C. elegans* Ca^{2+} dynamics. We provide the design of the time-lapse volumetric confocal imaging system including a microfluidic device to accommodate the whole animal within the field-of-view of the imaging system. We examine the feasibility of the volumetric confocal imaging of a whole animal, and demonstrate imaging of the whole

animal *C. elegans* neurons' response to NaCl within a $630 \times 150 \times 25 \ \mu m^3$ volume at 2 Hz rate.

We report a high-throughput automated imaging platform for *C. elegans* nerve regeneration study. We describe the design of the automated imaging platform and the automation flow, and characterizes the performance of the platform. The imaging platform can obtain high-resolution 3D confocal images of 20 animals in 10 minutes. We show sample images of *C. elegans* anterior lateral microtubule nerve regeneration examples acquired via the automated imaging platform.

We demonstrate a planar laser activated neuronal scanning platform (PLANS), a high-throughput animal examination system for drug screening. We explain the construction of PLANS involving the optics, the microfluidic device, and the electronics. The PLANS system can scan an animal in less than 5 ms with a spatial sampling resolution of 3 μm FWHM. We show sample scanning results of a Huntington's disease model of *C. elegans*.

We summarize the studies discussed in this dissertation, and suggest relevant future research to follow up on the studies.

Table of Contents

List of Figures

Chapter 1: Introduction

One topic of importance in neuroscience is functional mapping of neurons using Ca^{2+} imaging. Ca^{2+} signals are essential for intracellular and neuronal communication such as synaptic transmission, mandatory for complex processes such as learning and memorizing, and involved in birth and death of neurons [1]–[4]. Hence, monitoring Ca^{2+} enables direct investigations of neuronal activities [5]. The development of Ca^{2+} imaging has been driven by parallel advancement of calcium indicators and imaging technologies. The latest Ca^{2+} imaging technology is capable of *in vivo* real-time monitoring of Ca^{2+} signals in localized regions or targeted neurons of model organisms, yet, whole-brain and whole-animal Ca^{2+} imaging remains challenging.

Another topic of huge interest in neuroscience is neurodegenerative diseases. Neurodegenerative diseases including Huntington's, and Alzheimer's diseases are the most common causes of life-quality-threatening dementia [6], [7], and the number of patients suffering neurodegenerative diseases has been increasing as the life expectancy prolongs. For instance, 5.1 million American people over 65 years old are affected by Alzheimer's disease in 2015, and the number is projected to reach 13.5 million by 2050, while the total costs of care for these patients are estimated to be $1.1 trillion in 2050 [8]. Comprehension of the molecular mechanisms administering nerve degeneration and regeneration will accelerate development of remedies and drugs to cure the diseases, however, the mechanisms are substantially unidentified. Hence, a good model organism for *in vivo* study of those mechanisms is essential.

Caenorhabditis elegans (*C. elegans*), a tiny worm, is a versatile neuroscience model organism suitable for researching both neurodegenerative diseases and functional mapping of all neurons in the whole animal. Based on *C. elegans*, a variety of neurodegenerative disease models have been invented [9] as well as a huge inventory of

fluorescent strains and calcium indicators for *C. elegans* are available through *Caenorhabditis* Genetics Center (CGC, NIH Office of Research Infrastructure Programs (P40 OD010440)). The high reproduction rate and the short generation period of *C. elegans* allow high-throughput disease studies, and the small size and the simple physiological neural structure of *C. elegans* suggest a possibility of *in vivo* real-time whole-animal Ca^{2+} imaging.

Realization of both the high-throughput disease studies and the *in vivo* real-time whole-animal Ca^{2+} imaging require novel *C. elegans* imaging modalities facilitating a fast imaging speed, a large field-of-view, a high resolution, and optical sectioning. We present high-speed imaging techniques we have developed for optical *in vivo* inspection of *C. elegans*.

1.1. DISSERTATION OVERVIEW

The primary objective of this dissertation is to report high-speed imaging techniques for *C. elegans* nervous system studies.

Chapter 2 provides background knowledge to assist readers to comprehend the subjects of the following chapters. **Chapter 2** shortly introduces *C. elegans*, the main model organism in this dissertation, and neuroscientific and biomedical studies using *C. elegans* involving calcium imaging, nerve regeneration, and drug screening. Subsequently, **Chapter 2** briefly explores technologies including confocal microscopy and microfluidic devices, which are used in the neuroscientific and biomedical studies.

Chapter 3 thoroughly discusses development of a high-speed laser scanning confocal microscope. **Chapter 3** provides the design principles used in the development of the confocal microscope including the optical, electrical, and software implementation, and the details of the confocal microscope we built based on the design principles. **Chapter 3**

2

also presents the performance characterization of the confocal microscope, then a few sample images obtained with the confocal microscope.

Chapter 4 presents development of time-lapse volumetric confocal imaging of whole animal *C. elegans* Ca^{2+} dynamics using the confocal microscope in **Chapter 3**. **Chapter 4** provides the design of the time-lapse volumetric confocal imaging system including a microfluidic device to accommodate the whole animal within the field-of-view of the imaging system. **Chapter 4** examines the feasibility of the volumetric confocal imaging of a whole animal, and demonstrates an example experiment to observe whole animal *C. elegans* neurons' response to NaCl including the experimental procedures.

Chapter 5 reports a high-throughput automated imaging platform for *C. elegans* nerve regeneration study. **Chapter 5** describes the design of the automated imaging platform and the automation flow, and characterizes the performance of the platform. **Chapter 5** shows sample images of *C. elegans* anterior lateral microtubule (ALM) nerve regeneration examples acquired through the automated imaging platform.

Chapter 6 presents a planar laser activated neuronal scanning platform (PLANS), a high-throughput animal examination system for drug screening. **Chapter 6** explains the construction of PLANS involving the optics, the microfluidic device, and the electronics. **Chapter 6** shows sample scanning results of a Huntington's disease model of *C. elegans*.

Chapter 7, the last chapter of this dissertation, summarizes the studies discussed in the previous chapters, and suggests relevant future research to follow up on the studies in this dissertation.

Chapter 2: Background

2.1. *C. ELEGANS* AS A MODEL ORGANISM

Caenorhabditis elegans (*C. elegans*, **Fig. 2.1**), a soil nematode, has desirable characteristics as a model organism for biology and neuroscience studies. *C. elegans* is easy to culture in the laboratory environment. *C. elegans* permits large population studies because it grows very rapidly, has a short generation time of 3 days, reproduces abundantly, and is a hermaphrodite. *C. elegans* enables observation of neuronal processes in living animals with the use of *in vivo* fluorescent markers due to its transparent body. *C. elegans* is a simple multicellular animal with 959 somatic cells comprising various organs and tissues including muscles, a reproductive system, and a nervous system of 302 neurons [10]–[13]. *C. elegans* is also the very first multicellular organism whose genome is fully sequenced [12], and whole structural neuronal circuitry is mapped [14]

C. elegans homologues have been identified for 60 – 80% of human genes [12], [15]–[18], and counterparts for human disease-related genes are found in *C. elegans* [12], [13]. For these advantages, *C. elegans* have been used as diseases models to study a variety of complex human diseases such as diabetes [19], and aging [19]–[21]. *C. elegans* models for neurodegeneration such as Alzheimer's disease [22]–[25], Parkinson's disease [26], [27], and Huntington's disease [28], [29] were reported. In addition, neuronal regeneration [30] and muscular dystrophy [31] were also researched using *C. elegans* models.

Figure 2.1: Wide-field images of *Caenorhabditis elegans*. (a) Bright-field image of *C. elegans* showing the internal structure of the animal (Credit: The Harman Lab at Kansas State University) (b) Wide-field fluorescent image of a *C. elegans* with a GFP strain. Courtesy of [32].

2.2. CONFOCAL MICROSCOPY

Confocal microscopy has been one of the standard optical imaging techniques to investigate fluorescent specimens for biomedical applications since the introduction of the first commercial confocal microscope [33], [34] due to its significant strengths compared to the conventional wide-field microscopy. Confocal microscopy provides a superior imaging resolution by a factor of up to 1.4 with the confocal pinhole size adjustment. Confocal microscopy optimizes the signal-to-noise ratio (SNR) of images by rejecting out-of-focus signals including background noise from scattered light. Most importantly, confocal microscopy generates optically sectioned images capable of 3D reconstruction of the specimen [35]–[37].

The optical principle of the confocal microscopy is illustrated in **Fig. 2.2**. One of the most efficient ways to understand the optical principle of confocal microscopy is to compare the optical principle of confocal microscopy (**Fig. 2.2b**) to that of the wide-field microscopy (**Fig. 2.2a**). In wide-field microscopy, the light from the object is projected onto the image plane through the lens. Not only does in-focus light from the object reach the image plane, but out-of-focus light from the object and the surroundings also arrives the image plane. Hence, the detector placed on the image plane collects both in-focus and out-of-focus light, and produces low signal-to-noise images blurred by the out-of-focus light as shown in **Fig. 2.2a**. This blurring by the out-of-focus light deteriorates when the objective is inside a dense region filled with other objects.
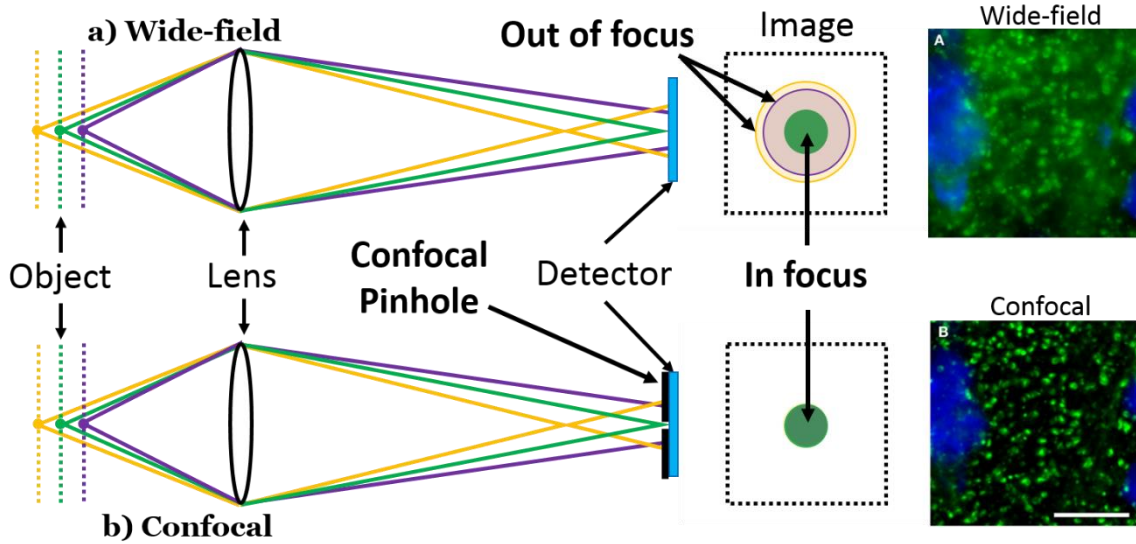
Figure 2.2: Principle of confocal microscopy. (a) Imaging principle of wide-field microscopy. (b) Imaging principle of confocal microscopy. Fluorescent images for wide-field and confocal microscopy comparison are in courtesy of [38]. The green line is in-focus light, and the yellow and purple lines are out-of-focus light.

On the contrary, almost only the in-focus light is detected by the detector in confocal microscopy. Even though both the in-focus and out-of-focus light travels up to the image plane, the confocal pinhole allow most of the in-focus light and a negligible amount of the out-of-focus light to pass as shown in **Fig. 2.2b**. Thus, the detector placed on the image plane collects mostly the in-focus light, and produces high SNR images free of blurring by the out-of-focus light (**Fig. 2.2b**). Additionally, the in-focus light originates only from the object focal plane, and the image that consists only of the in-focus light contains information only about the object focal plane. Hence, confocal microscopy achieves optical sectioning which allows for construction of 3D images.

2.3. *C. ELEGANS* CALCIUM (CA^{2+}) IMAGING

Ca^{2+} imaging is a well-established method for neuronal activity observation since calcium is an essential intracellular messenger in neurons [5], [39], [40]. *C. elegans* is one of the versatile model organisms for Ca^{2+} imaging since the advantages of *C. elegans* as a model organism for neuroscience also apply to Ca^{2+} imaging. Activities of *C. elegans'* chemosensory neurons [41]–[44], motor neurons [45]–[49], thermosensory neurons [50], and olfactory neurons [51] were characterized with diverse stimulus in varied conditions through Ca^{2+} imaging.

In *C. elegans* Ca^{2+} imaging, wide-field microscopy with a CCD or CMOS camera has been the most common imaging method [42], [45]–[47], [51]. Wide-field microscopy is a feasible imaging method for monitoring a single neuron or a few targeted neurons. However, wide-field microscopy is not capable of resolving individual neurons inside the head region of *C. elegans* encoded with pan-neuronal strains. The *C. elegans* head region is densely packed with a majority of tiny *C. elegans* neurons, thus, the wide-field microscopy images suffer severely from out-of-focus fluorescent signals of densely packed

neurons. This challenge necessitates novel imaging methods capable of producing optically-sectioned high-resolution volumetric images at rates higher than the neurons' Ca^{2+} response frequency.

Various approaches to achieve high-speed high-resolution volumetric imaging were reported. Light-sheet microscopy was used to observe activity of all neurons in the zebrafish brain at 0.8 VPS [52]. Spinning disk confocal microscopy [53] and the wide-field temporal focusing technique [44] were used to track all neurons in the *C. elegans* brain at 5 VPS. Light-field microscopy was used to monitor all of the neurons in the whole *C. elegans* [43]. Swept confocally-aligned planar excitation (SCAPE) microscopy was invented to image freely moving *Drosophila* larvae at 10 VPS [54]. These high-speed volumetric imaging methods provide either a small FOV with a high-resolution, or a large FOV with a low resolution. For example, the light-field microscopy [43] provides a FOV large enough to cover the whole body of a bent *C. elegans* yet cannot resolve individual neurons due to its poor imaging resolution. A high-speed high-resolution volumetric imaging method with a large FOV is necessary to perform Ca^{2+} imaging of the whole *C. elegans*, however, no method capable of Ca^{2+} imaging of the whole *C. elegans* with an adequate imaging resolution to capture *C. elegans* neurons' nuclei has been reported.

2.4. NERVE REGENERATION STUDIES OF *C. ELEGANS* USING LASER AXOTOMY

C. elegans was proven to be a feasible model for injured nerve regeneration studies combined with the femtosecond laser surgery technique in 2004 [30]. However, the laser surgery on *C. elegans* axons was conducted on agar plates with no automation, and the regeneration of the severed axons was also manually observed on agar plates while the animal was chemically anesthetized. This labor-intensive and time-consuming process was addressed by development of automated laser axotomy techniques combined with lab-on-

a-chip microfluidic devices. The automated laser axotomy techniques accomplished precise and repeatable laser surgery supported by stable immobilization of animals without the use of anesthetics [55]–[57]. Though those automated laser axotomy techniques significantly expedited the *C. elegans* axotomy process, the examination of axon regeneration was still carried out on agar plates with anesthetics applied to the animal, thus, the manual examination of nerve regeneration remained the major bottleneck of the nerve regeneration research.
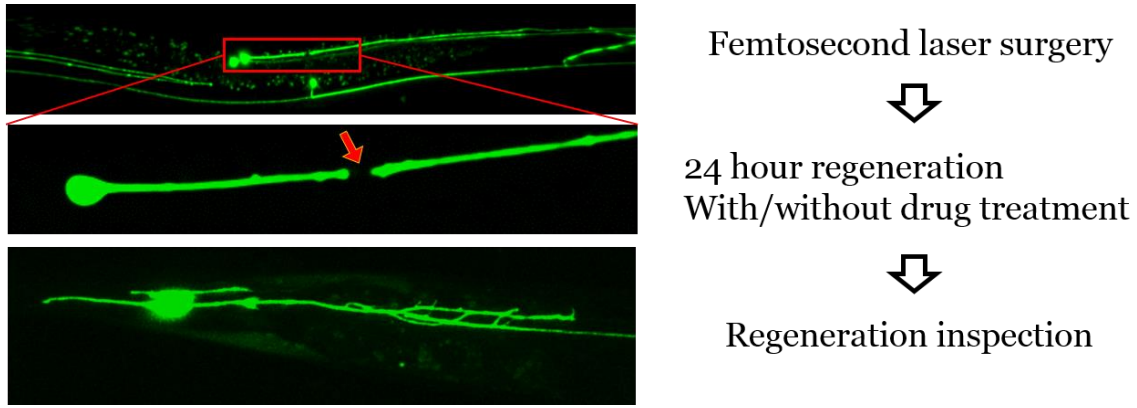
Figure 2.3: *C. elegans* nerve regeneration study. Confocal fluorescent images of ALM and PLM axons labelled with GFP immediately after and 24 hours after a femtosecond laser surgery.

To address the bottleneck of the manual examination, we developed a high-throughput automated confocal imaging platform. Our high-throughput imaging platform consists of a high-speed confocal microscope, and a microfluidic device for multiple animal parallel trapping in desirable orientations for effective imaging. Our imaging platform takes very high-resolution 3D confocal images of regenerated axons of 20 animals in 10 minutes. The high-resolution 3D confocal images allow more accurate evaluation of axon reconnection and regeneration, and the short imaging time prevents the image SNR

drop due to the autofluorescent emission from animals stressed induced by the physical immobilization pressure.

2.5. DRUG SCREENING WITH *C. ELEGANS*

The existence of plentiful *C. elegans* disease models and the aforementioned advantages as a model organism make *C. elegans* an excellent tool for whole-organism high-throughput drug screening (HTS) [9]. Advantages in using *C. elegans* for HTS are: the possibility of modeling sophisticated human diseases which are challenging to duplicate in unicellular models, a large collection of scorable phenotypes, the higher chances of discovering drugs more effective in humans due to the use of the whole multicellular organism, and the support of time-proven genetic tools and resources [13], [58], [59].

Conventionally, chemical compounds have been tested on *C. elegans* on agar plates [10]. This agar plate method consumes a large amount of chemicals, is labor intensive and time consuming, and not applicable for HTS. The first large-volume *C. elegans* drug screening using a Complex Object Parametric Analyzer and Sorter (COPAS^{TM} BIOSORT, Union Biometrica) was reported in 2006 [60] though this method still relied on agar plates for screening, and the phenotypes were manually scored. Between 2006 and 2009, several liquid-based and agar-plate-free screen methods were developed yet they still depended on manual inspection and assessment [61]–[63]. Recently, multi-well plate based [64], [65] and microfluidic device based [60], [66]–[68] drug and chemical compound screening methods were demonstrated. These methods incorporated automated animal delivery, and image acquisition and analysis, hence, significantly reduced the amount of labor and time for assessment. However, these methods are still not compatible with screening for hundreds of thousands of drugs because they use slow-speed snap-shot imaging of the

nervous system, sometimes only partially, with limited resolution. This shortcoming suggests a need for new technologies to achieve ultrafast whole animal scanning.

Our PLANS system scans the whole nervous system of living *C. elegans* rapidly enough for chemical compound screening. Our PLANS system provides a scanning rate of 100's of animals per second, comparable to the performance of commercial biosorters [69], while characterizing the nervous system at a cellular resolution. Our PLANS method will allow us to examine up to one million distinct chemical compounds per year for their effectiveness in preventing or delaying the degeneration of identified neurons through aging and disease.

2.6. MICROFLUIDIC DEVICES

Microfluidics has been extensively adopted as a versatile platform for chemical and biological studies due to its significant strengths since the introduction of the polymer-based soft-lithography and microfluidic devices made out of polydimethylsiloxane (PDMS) [70]. Microfluidic devices allow experiments to use lesser amounts of chemicals, specimens, and space compared to the conventional methods. Microfluidic devices also enable automation, and high-throughput experiments. In addition, PDMS is transparent, biocompatible, and gas-permeable, hence, is highly favorable for biological studies [71], [72]. Thus, PDMS-based microfluidic devices can simulate *in vivo* microenvironments for cells, tissues, and even living organisms [73].

Microfluidics has been considerably contributing to biology and neuroscience studies using *C. elegans* as a model organism. Microfluidics is remarkably functional in precisely controlling and manipulating *C. elegans* whose small size hampers handling of *C. elegans* [74], [75]. The most troublesome task in *C. elegans* experiments is to immobilize the animal. In conventional *C. elegans* experiments on petri dishes, or agar

plates, *C. elegans* is usually chemically anesthetized, or glued to the substrates for thorough inspection and manipulation [76]. The toxicity and influence of the anesthetics and glue to the animal is difficult to determine, hence, the use of anesthetics and glue may disturb the integrity of experiments [46]. On the contrary, microfluidic devices are capable of *in vivo C. elegans* immobilization without using chemicals [46], [55], [57], [77]–[83]. Two example microfluidic devices are shown in **Fig. 2.4**. In addition, microfluidic devices can deliver test chemicals to the target animal in a finely controlled and automated manner, and can manage a large population of animals either in parallel or in series on top of the aforementioned advantages of microfluidic devices in the previous paragraph.

We developed a microfluidic device to immobilize a single *C. elegans* in predefined geometry, and to apply various chemical stimuli to the immobilized *C. elegans* for our high-speed functional volumetric imaging platform (**Chapter 4**), a microfluidic device to immobilize multiple *C. elegans* in parallel for our high-throughput automated confocal imaging platform (**Chapter 5**), and a microfluidic device to transport and scan *C. elegans* in series for our PLANS system (**Chapter 6**).
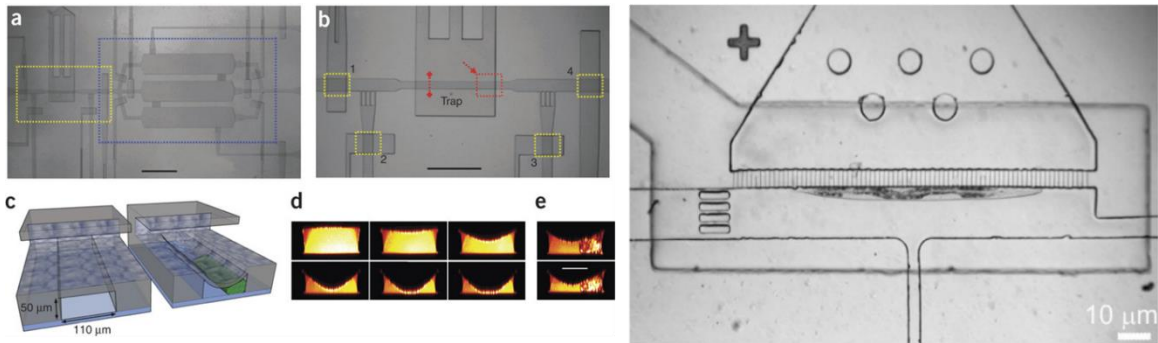
Figure 2.4: Microfluidic devices for single *C. elegans* immobilization. Courtesy of [55] (left) and [57](right).

Chapter 3: High-speed laser scanning confocal microscope

3.1. INTRODUCTION

Most mirror scanning confocal microscopes including state-of-the-art commercial products generate a single image at $1 - 4$ FPS [84] due to the movement velocity limit of the galvanometric scanners in the confocal microscopes. This $1 - 4$ FPS rate could be too slow for 3D volume stack imaging and real-time *in vivo* applications where rapid dynamics need to be captured. Common scanning methods to increase the imaging rate are the disk scanning [85], [86], the acousto-optic deflector (AOD) scanning [87], the polygon mirror scanning [88], [89], and the resonant galvanometric mirror scanning [90]–[93].

The disk scanning method achieves very high imaging rates, typically 200 FPS. However, 1% transmission of excitation and emission light through the disk disallows observation of weak fluorescent specimens. The weak fluorescent signal can be compensated with a longer exposure, however, that nullifies the imaging speed advantage of the disk scanning method. In addition, the rather large pinhole size, the crosstalk among pinholes on the disk, and the back-reflection of the excitation light by the disk deteriorate the imaging resolution, and the image SNR of the disk scanning confocal microscope. AOD scanning is impractical for confocal microscopy. The wavelength-dependent nature of AOD prohibits the de-scanning of fluorescent emission from the specimen, and demands complicated and costly optical compensation in the system. The polygon mirror scanning generates unstable and deformed images due to the vibration from the high-velocity rotation of the heavy polygon mirror, and the mirror surface variation of different polygon facets.

The resonant galvanometric mirror scanning provides 16 kHz bi-directional line scanning rate while following the conventional galvanometric mirror's scanning principle.

Thus, the resonant scanning can be easily integrated into the well-established galvanometric mirror scanning system. The only drawback of the resonant mirror scanning is the image stretching due to the sinusoidal scanning velocity attribute [92], [93], yet, the image stretching can be easily corrected with simple computation [92]–[94].

The previously reported resonant scanning confocal microscopes share one common limit in imaging. Those confocal microscopes can generate only up to 512 pixels per line, hence, 512×512 pixels per image, which limits the FOV of the confocal microscope due to the Nyquist criterion. This limit stems from the low data acquisition rate of the frame grabber they used, and the synchronization and control method based only on electronic hardware. We developed a hardware and software hybrid control and synchronization system, and used a high-speed digitizer to realize flexible control of our confocal microscope, and a huge number of pixels per image up to $7,000 \times 7,000$ pixels. This high-speed laser scanning confocal microscope functions as the core imaging method for the systems in **Chapter 4** and **Chapter 5**.

3.2. DESIGN OF THE CONFOCAL MICROSCOPE

3.2.1. Overall system

Our resonant scanning confocal microscope is a complex optical imaging system comprised with optical, electrical, and mechanical components as shown in **Fig. 3.1**. Those components are largely separated into two categories: (1) Optical setup and (2) Electrical setup. The optical setup consists of lenses, mirrors, scanners, a laser, optical fibers, detectors, stages, and mechanical mounts to hold the components in the optical setup. The electrical setup includes stage controllers, scanner drivers, a custom electronic circuit, a

transimpedance pre-amplifier (pre-amp), and a computer equipped with a high-speed digitizer, a multifunction data acquisition card (MDAQ), and software to control the high-speed digitizer, and MDAQ. The optical setup excites the fluorophores in the specimen, collects the emitted photons from the fluorophores, and converts the photons into electrical signals via the detectors. Then, the electrical setup controls the scanners and the stages to enable efficient specimen excitation and photon collection, receives, and converts the electrical signals from the detectors into digital signals to save, and display. The subsequent chapters explain these processes in detail.

3.2.2. Optical system

The optical setup of our resonant laser scanning confocal microscope is illustrated in **Fig. 3.2**. We use the continuous wave (CW) diode laser with a 488 nm wavelength (Spectra Physics, Cyan 488) as the excitation light source to efficiently excite the green fluorescent protein (GFP) in the specimen. The single-mode optical fiber (Thorlabs, P1-460B-FC-5) delivers the CW laser to the confocal microscope.

The use of the optical fiber has two advantages. Firstly, the single-mode optical fiber prevents degradation of imaging resolution by filtering out multi-mode components in the laser. The multi-mode components in the laser enlarges the laser spot size on the focal plane hence degrades the imaging resolution of the microscope. Secondly, the optical fiber protects the confocal microscope from deviation of the CW laser output angle. Without the optical fiber delivery of the CW laser, the deviation of the CW laser output angle affects the laser beam propagation along the confocal microscope's optical path thus causes microscope malfunction. On the contrary, with the optical fiber delivery, the deviation of the CW laser output angle has no effect on the laser beam propagation along

the microscope's optical path, because the laser beam output of the optical fiber is unaffected by the CW laser output angle deviation.
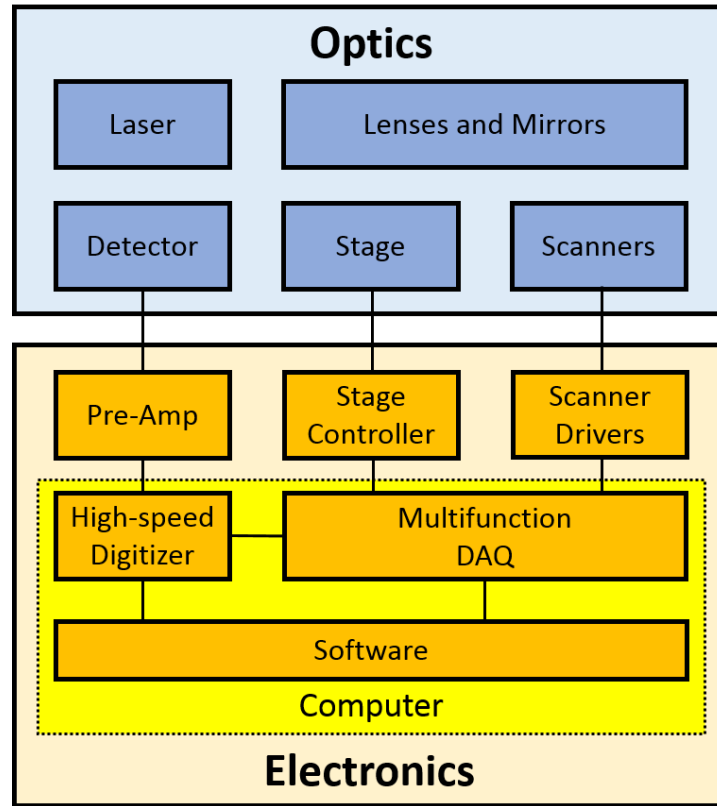
Figure 3.1: Schematics of the overall laser scanning confocal microscope. Optics, electronics, and software. The optics consist of lenses, mirrors, scanning mirrors, a light source (laser), a detector, and opto-mechanical components. The electronics consist of a transimpedance pre-amplifier, a motorized and piezo stage controller, scanning mirror controllers, and a computer equipped with a high-speed digitizer, a multifunction data acquisition card (DAQ), and software to control the digitizer and the DAQ.

The CW laser beam from the optical fiber output is collimated to be 4 mm in diameter by an aspherical collimation lens (Thorlabs, C560TME-A, f = 13.86 mm). The collimated laser beam is reflected by the dichroic mirror (Thorlabs, MD499), then, scanned by the XY scanner. The XY scanner is comprised of the resonant mirror (Cambridge

Technology, CRS 8 kHz) for the X scanner as the fast axis, and the galvanometric mirror (Cambridge Technology, 6215H) for the Y scanner as the slow axis. The resonant mirror has a clear aperture diameter of 4 mm that decides the collimated CW laser beam diameter.

The scanned laser beam is relayed and expanded 3.3 times to be 13.2 mm in diameter by the scan lens (Thorlabs, AC508-075-A, f = 75 mm) and tube lens (Thorlabs, AC508-250-A, f = 250 mm) pair. The enlarged laser beam is focused onto the specimen by the objective, and excites the fluorophores inside the specimen mounted on the motorized stage. Both of the scan lens and the tube lens are achromatic doublet lenses of 2 inch in diameter. The use of the achromatic lenses minimizes the chromatic aberration by two dissimilar wavelengths of the 488 nm excitation laser and the 500 − 520 nm GFP emission. If the chromatic aberration is not minimized, either the excitation efficiency, the efficiency of emission collection, or both drop, hence, the overall imaging performance of the confocal microscope degrades. The use of the 2 inch lenses is essential to utilize the full tilting angle of the XY scanner thus to maximize the field-of-view (FOV) of the confocal microscope. The 3.3x laser beam expansion to 13.2 mm ensures the laser beam slightly overfills the back aperture of the objective. Overfilling of the back aperture of the objective assures the laser beam uses the full numerical aperture (NA) of the objective, thus forms the smallest focal spot down to the diffraction limit. If the back aperture of the objective is underfilled, the laser beam experiences an effective NA lower than the full NA of the objective, hence forms a focal volume larger than the diffraction limited volume size both laterally and axially. A larger focal volume downgrades the imaging resolution since the excitation focal volume size determines the unit excited volume in the specimen.

The excited fluorophores within the excitation focal volume emit fluorescent photons isotropically. A portion of the emitted fluorescent photos are collected by the objective. The collected photons travel backwards through the optical propagation path of

the excitation laser beam from the objective to the scan lens. After the scan lens, the scanning mirrors send fluorescent photons back to the dichroic mirror on the exact position where the excitation laser beam has been reflected. This process of delivering the fluorescent photons to the initial position of the excitation laser beam is called 'descanning.' Having reached the dichroic mirror, the fluorescent photons pass through the dichroic mirror, then, are focused onto the confocal pinhole (Thorlabs, P15S, 15 μm diameter) by the pinhole lens (Thorlabs, AC254-75-A, f = 75 mm). The confocal pinhole allows only the in-focus fluorescent photons from the excitation focal volume to pass while blocking the out-of-focus photons from the vicinity of the excitation focal volume and unwanted noise light from the surroundings of the confocal microscope. The size of the confocal pinhole is decided to be approximately 1 Airy Unit (AU) for various objectives to achieve optimal SNR. For a 488 nm laser, 1 AU of a 40x 1.3NA oil objective and a 20x 0.95 NA water immersion objective are 18.3 μm and 12.5 μm, respectively. Lastly, the in-focus fluorescent photons propagate into the photomultiplier tube (PMT, Hamamatsu, H10770PA-40)

The PMT detects the in-focus fluorescent photons, and converts the detected photons into an electric current. The PMT also amplifies the electric current by several orders of magnitude. The amplified electrical current travels to the high-speed transimpedance amplifier (pre-amp, Femto, DHPCA-100) that converts and amplifies the electric current into a voltage signal. The voltage signal from the pre-amp is delivered to the high-speed data digitizer (AlazarTech, ATS9462) where the voltage signal is sampled into 16-bit digital data. The sampled data is processed and reconstructed into 2D images by our custom software written with LabVIEW (National Instruments, 2013, 64bit). The 2D images are display on the display, and saved in the storage device when necessary.
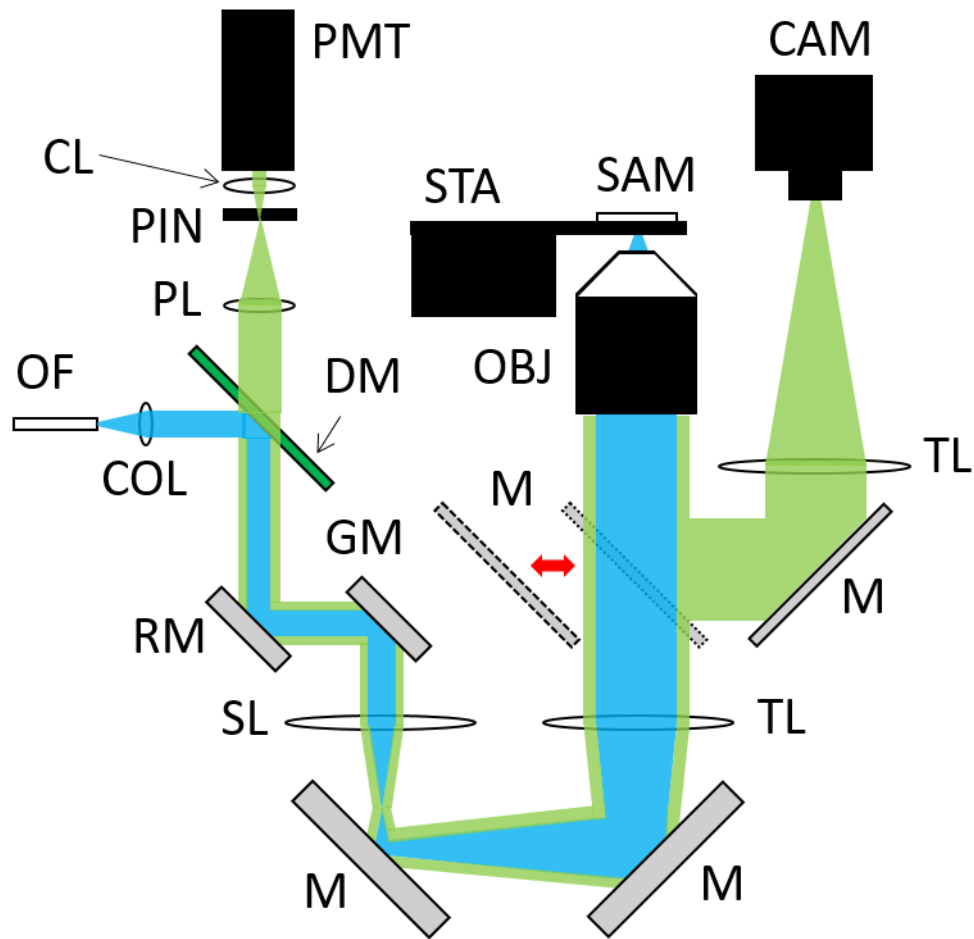
Figure 3.2: The optical setup of the laser scanning confocal microscope. The laser scanning confocal microscope and the wide-field microscope. OF: Optical fiber output, COL: Collimation lens, DM: Dichroic mirror, RM: Resonant scanning mirror (fast axis), GM: Galvanometric scanning mirror (slow axis), SL: Scan lens, TL: Tube lens, OBJ: Objective, SAM: Specimen, STA: Motorized stage with stepper motors and a piezo module, PL: Pinhole lens, PIN: Pinhole, CL: Collection lens, PMT: Photomultiplier tube, CAM: Camera, M: Mirror. SL, TL, and M are of 2 inch optics.

Our laser scanning confocal microscope is also capable of wide-field microscopy. A mirror mounted on a motorized translational stage, a tube lens, and a camera are added to construct a wide-field microscope. When the mirror is placed between the tube lens and the objective, the confocal microscope operates as a wide-field microscope. The capability

of wide-field microscopy is essential for the following reasons. Firstly, placing a specimen in the field-of-view of the confocal microscope is practically impossible without wide-field microscopy. Until the specimen is correctly positioned within the field-of-view and on the focal plane, the confocal microscope shows nothing due to the optical sectioning of the confocal microscope. Secondly, the wide-field microscopy provides useful additional information about the specimen such as the structure while the confocal microscope shows fluorescent images.

One of the most crucial elements in building a point scanning microscope is the design of the scanning system. Among various eligible scanning system designs, our confocal microscope uses an optical scanning system design that consists of scanning mirrors, a scan lens, a tube lens, and an infinity-corrected objective as shown in **Fig. 3.3**. For simplicity, **Fig 3.3** illustrates only one axis of the scanning system since the scanning mechanism is identical for both axes except they are orthogonal in direction. The scan lens and the tube lens together convert the deflection angle (θ), at which the scanning mirror pivots the excitation laser beam, into the incident angle where the excitation laser beam enters the back aperture of the objective. Additionally, the scan lens and the tube lens constitutes a Keplerian beam expander to expand and collimate the excitation beam since the infinity-corrected objective requires a collimated excitation laser beam, and the back aperture of the objective must be overfilled to achieve the best imaging resolution the objective can potentially provide.
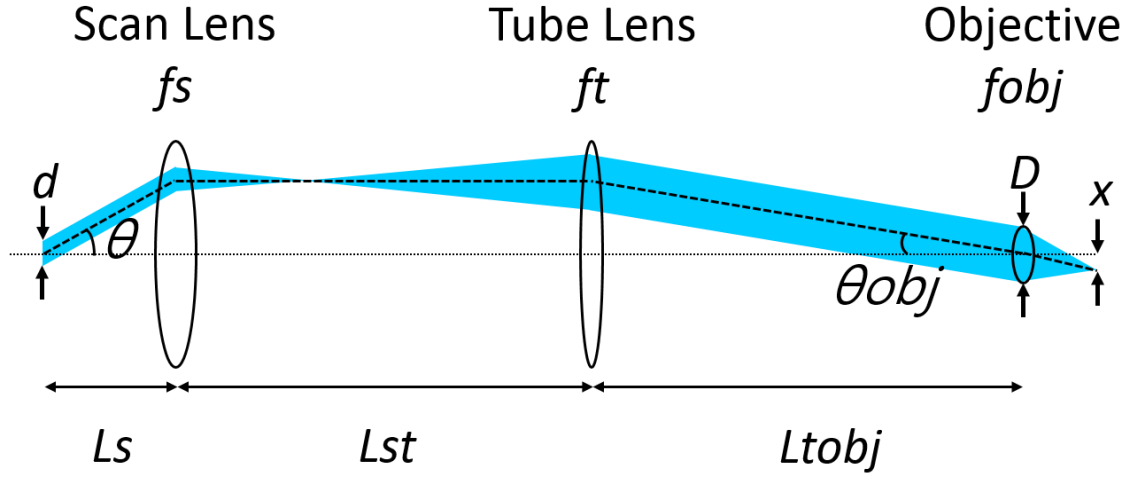
Figure 3.3: Scanning optics design. $fs \equiv$ the focal length of the scan lens, $ft \equiv$ the focal length of the tube lens, $fobj \equiv$ the focal length of the objective, $d \equiv$ the beam diameter at the scanning mirror, $D \equiv$ the beam diameter at the back aperture of the objective, $\theta \equiv$ the maximum deflection angle of the excitation laser beam with respect to the optical axis, $\theta obj \equiv$ the maximum incident angle of the excitation laser beam on the objective back aperture, $x \equiv$ the half field-of-view, $Ls \equiv$ the distance between the scanning mirror and the scan lens, $Lst \equiv$ the distance between the scan lens and the tube lens, $Ltobj \equiv$ the distance between the tube lens and the back aperture of the objective.

From now, the optical scanning system used in our confocal microscope is mathematically described. The related variables are

$fs \equiv$ Focal length of the scan lens (mm)

$ft \equiv$ Focal length of the tube lens (mm)

$fobj \equiv$ Focal length of the objective (mm)

$Ls \equiv$ Distance between the center of the scanning mirror and the scan lens (mm)

$Lst \equiv$ Distance between the scan lens and the tube lens (mm)

$Ltobj \equiv$ Distance between the tube lens and the objective (mm)

$d \equiv$ Diameter of the excitation beam on the scanning mirror (mm)

21

$D \equiv$ Diameter of the back aperture of the objective (mm)

$Dcol \equiv$ Diameter of the collimated excitation laser beam (mm)

$\theta \equiv$ Max. deflection angle of the excitation beam with respect to the optical axis

$\theta obj \equiv$ Max. incident angle of the excitation beam on the objective back aperture

$x \equiv$ Half field-of-view ($2x \equiv$ Full field-of-view)

The scan lens and the tube lens must construct a Keplerian beam expander to expand and collimate the excitation laser beam. Hence, the distance between the scan lens and the tube lens must be equal to the addition of the focal lengths of the two lenses.

$$Lst = fs + ft \tag{3.1}$$

The center of the scanning mirror clear aperture should be imaged onto the center of the objective back aperture. Assuming that the center of the excitation laser bean is well aligned onto the center of the scanning mirror, imaging the center of the scanning mirror onto the center of the objective back apertures ensures the center of the excitation laser beam enters the center of the objective back aperture regardless of the scanning mirror tilting angle. This imaging requirement is mathematically described by

$$Ls = \frac{fs^2}{ft} + fs - Ltobj\left(\frac{fs}{ft}\right)^2 \tag{3.2}$$

Analyzing Eqn. (3.2), Ls solely depends on $Ltobj$ since fs and ft are constants once the scan lens and the tube lens are selected. Additionally, Lst is a constant as well by Eqn. (3.1). Hence, the scan lens and the tube lens should be mounted on translational stages for precise alignment when building the confocal microscope. Eqn. (3.2) is easily derived by the ABCD ray tracing method.

As mentioned before, the excitation laser beam must fill or slightly overfill the objective back aperture to use the entire NA of the objective and the best imaging resolution the confocal microscope can potentially achieve. Mathematically speaking,

$$Dcol > D \tag{3.3}$$

Back apertures of typical microscope objectives are approximately 10 to 12 mm in diameter. On the contrary, clear apertures of typical scanning mirrors are 3 to 6 mm in diameter. Assuming the excitation laser beam fills the clear aperture of the scanning mirror, the required magnification, M, is given by

$$M = D/d \cong 2 \text{ to } 4 \tag{3.4}$$

The clear aperture of the fast axis scanning mirror used in our confocal microscope is 4.7 mm in diameter. However, we design the excitation laser beam diameter incident on the fast axis scanning mirror to be 4 mm, because it should be smaller than the clear aperture of the scanning mirror to prevent a laser power loss and any laser beam scattering and diffraction, which may cause a laboratory hazard.

The Keplerian beam expander, or the telescope, consists of the scan lens and the tube lens must accomplish the required magnification, M, governed by Eqn. (3.4). Hence, the magnification by the scan lens and the tube lens, Mts is given by

$$Mts = \frac{ft}{fs} \geq M \tag{3.5}$$

Though *Mts* must be either equal to or higher than *M*, *Mts* must not be exceedingly large because *Mts* increase reduces the field-of-view for a given deflection angle, *θ*. The half field-of-view, *x*, is given by

$$x = fobj \cdot \tan(\theta obj) \cong fobj \cdot \tan(\theta/Mts) \qquad (3.6)$$

As shown in Eqn. (3.6), a larger *Mts* results in a smaller *θobj* due to the angular demagnification by the telescope, then consequently reduces the field-of-view. Thus, the focal lengths of the scan lens and the tube lens must be carefully selected considering the trade-off between the size of the expanded excitation laser beam and the field-of-view of the confocal microscope. We choose a 2-inch achromatic doublet with a 75 mm focal length for the scan lens (Thorlabs, AC508-075-A, *fs* = 75 mm). The clear aperture diameter of 2 inch is critical to take advantage of the full deflection angle provided by the scanning mirrors, then to accomplish the largest field-of-view with the given scanning mirrors, and optics. The chromatic aberration correction is essential to minimize the optical path length difference between the excitation laser beam and the fluorescent photons, then diminish the chromatic aberration. Since the excitation laser beam diameter on the scanning mirror is 3.8 mm, *Mts* has to be at least 3.15 to fill the objective back aperture of 12 mm in diameter. By Eqn. (3.5), the focal length of the tube lens must be over 235 mm (*ft* > 235 mm). We choose a 2-inch achromatic doublet with a 250 mm focal length for the tube lens (Thorlabs, AC508-250-A, *ft* = 250 mm). This tube lens with a rather long focal length restricts objective options for the confocal microscope.

The standard focal lengths of the tube lenses vary according to the objective manufacturer. Zeiss, Olympus, and Nikon objectives use tube lenses of 165 mm, 180 mm, and 200 mm focal lengths, respectively. Olympus, and Nikon objectives allow use of non-

standard tube lenses while Zeiss objectives must be paired with the Zeiss proprietary tube lens, because Olympus, and Nikon objectives achieve all aberration corrections within the objectives while Zeiss objectives achieve correction of chromatic aberration via the Zeiss proprietary tube lens. As a result, our laser scanning confocal microscope uses only Olympus, and Nikon microscope objectives.

Using Eqn. (3.1) – (3.6), we characterize the optical scanning system of our confocal microscope. The focal lengths of the scan and the tube lenses are already given above, and make Mst = 3.33. We choose 200 mm for the distance between the tube lens and the objective ($Ltobj$ = 200 mm) so that the space between the tube lens and the objective can accommodate the motorized translational stage to mount a mirror for the wide-field microscope. Setting $Ltobj$ slightly less than ft increases Ls hence gives an extra room to install an opto-mechanical component such as an iris to assist the alignment process in building the confocal microscope. Eqn. (3.2) computes the distance between the scanning mirror and the scan lens is 79.5 mm (Ls = 79.5 mm). The maximum deflection angle of the resonant mirror (θ) is ±7.5º referring to the manufacturer's specification. Knowing all the variables required to calculate the field-of-view, the full field-of-view (FOV) is given by

$$FOV\left(\text{mm}\right) = 2 \times Cobj\,\frac{200}{Mobj} \times 0.039 = 2 \times fobj \times \tan\left(\frac{\theta}{Mst}\right) \qquad (3.7)$$

where $Cobj$ is an objective coefficient, $Mobj$ is the magnification of an objective when combined with the objective's standard tube lens, and the 200 is the standard focal length of the tube lens for Nikon objectives. $Cobj$ is 0.9 for Olympus objectives, and 1.0 for Nikon objectives. The full field-of-views estimated by Eqn. (3.7) are 390 μm for a Nikon 40x 1.3NA oil immersion objective, and 700 μm for an Olympus 20x 0.95NA water immersion objective.

25

The design principle for the other scanning axis is identical to the design process described in the previous paragraphs. Designing a two-dimensional scanning system needs to meet a couple of conditions more than designing a one-dimensional scanning system. However, those conditions are minor and easily fulfilled when the separation between the two scanning mirrors (Ssm) is significantly smaller than the focal length of the scan length ($fs \gg Ssm$). In our confocal microscope, $Ssm \fallingdotseq 7$ mm, while $fs = 75$ mm. Hence, the two-dimensional scanning system works properly assuming building the two-dimensional scanning system is equivalent to combining two one-dimensional scanning systems. Tsai *et al*. discuss the conditions in designing a two-dimensional scanning system more in-depth in [95]. Additionally, [95], and [96] provide quality consultation on designing and building a laser scanning microscope, which can be applied to both confocal and multi-photon microscopes.

3.2.3. Electrical system

The electrical system of our confocal microscope accomplishes the fastest scanning speed that the resonant scanning mirror can potentially achieve, and provides flexible control of scanning to meet requirements for various scanning applications. The electrical system of our confocal microscope consists of the resonant scanning mirror driver (Cambridge Technology, CRS 8 kHz driver board), the galvanometric scanning mirror driver (Cambridge Technology, MicroMax 671215HHJ-1FHP), the motorized stage controller (Thorlabs, BSC203), the piezo module controller (Thorlabs, MDT693A), and the custom electrical circuit, and the multifunction data acquisition card (MDAQ, National Instruments, NI PCIe-6353), the high-speed digitizer (HSDG, AlazarTech, ATS9462), and the custom-built computer that contains the MDAQ, the HSDG, and the custom confocal

software written by LabVIEW (National Instruments, 2013). The connections and the signal flow directions among the electrical system components are shown in **Fig. 3.4a**. The core function of the electrical system of our confocal microscope is to control and synchronize the optical, mechanical and electrical components in the confocal microscope.

The control and synchronization achieved by three major components (the control and synchronization unit): the MDAQ, the custom electrical circuit, and the custom confocal software. The control and synchronization unit requires two input signals, and generates two internal signals and five output signals. The two input signals are the resonant mirror reference clock signal (*Rclk*), and the user input for the scanning condition (*Uin*). The internal signals are the line trigger signal (*Ltrig*), and the waveforms (*Wfm*) for the output signals that MDAQ generates. The outputs are the enhanced resonant mirror reference clock signal (*Rclk'*), the resonant mirror scanning angle control signal (*Rsig*), the frame trigger signal (*Ftrig*), the galvanometric mirror control signal (*Gsig*), and the motorized and piezo stage control signal (*Ssig*). The custom electronic circuit of our controller receives *Rclk*, enhances *Rclk* into *Rclk'*, converts *Rclk'* into *Ltrig*, and relays *Rclk'* and *Ltrig* to MDAQ. The custom confocal software generates *Wfm* based on *Uin*, and transmits *Wfm* to MDAQ. Receiving *Rclk'*, *Ltrig*, and *Wfm*, MDAQ generates *Rsig*, *Ftrig*, *Gsig*, and *Ssig*.
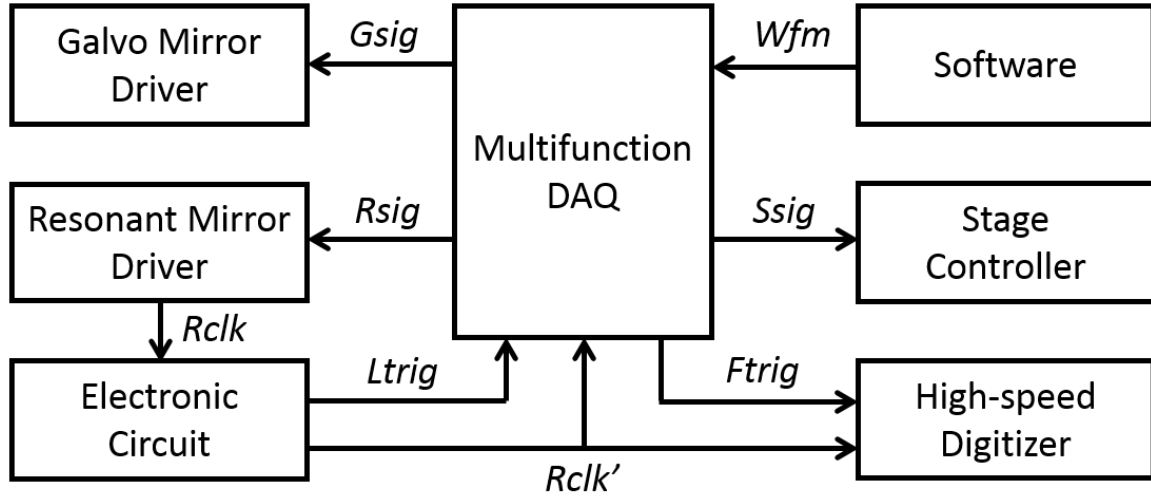
Figure 3.4: The schematics of control and synchronization electronics of the laser scanning confocal microscope. *Gsig*: Galvanometric mirror control signal, *Rsig*: Resonant mirror control signal, *Ltrig*: Line trigger signal, *Rclk*: Resonant mirror timing signal, *Rclk'*: Refined resonant mirror timing signal, *Ftrig*: Frame trigger signal, *Ssig*: Stage control signal, *Wfm*: waveforms of control and synchronization signals.

Multifunction data acquisition card (MDAQ)

The multifunction data acquisition card (MDAQ) is the core component of the control and synchronization unit. The MDAQ generates the output electrical signals using the signal waveforms, *Wfm* in **Fig. 3.4**, provided by the custom software, and the electrical signals, *Rclk'* and *Ltrig*, from the custom electrical circuit. The MDAQ uses *Rclk'* as the start trigger. The MDAQ begins generating the output electrical signals only when MDAQ detects the rise signal transition from off-state to on-state in *Rclk'*. MDAQ uses *Ltrig* as the reference timing clock for signal generation.

The MDAQ enables flexible control and synchronization of the confocal microscope. The MDAQ is a versatile device that works as a data acquisition device and a function generator simultaneously. The MDAQ accepts both analog and digital signal inputs, and generate analog and digital signal outputs concurrently. In addition, the

operations of the MDAQ is fully software-programmable. Hence, the MDAQ can interact with various devices altogether through both analog and digital channels. Previous laser scanning microscopy systems reported in academic journals employed entirely hardware-based control and synchronization systems [84], [88], [92], [97]–[101]. The entirely hardware-based systems tend to be less adaptable and modifiable in their operations, thus the previous scanning microscopy systems could image under the restricted configurations pre-defined by the designs of the hardware-based systems. Additionally, updating the configurations and adding new functions often require designing and building new hardware-based systems. In contrast, our control and synchronization system using the MDAQ can adopt additional functions and improvements simply by updating the MDAQ software. The MDAQ also has spare analog and digital inputs and outputs for possible additions of new devices to the systems.

Custom electrical circuit

The custom electrical circuit enhances *Rclk* into *Rclk'*, and generates *Ltrig* by processing *Rclk'*. The enhancement makes *Rclk'* a reliable, robust, and clean standard TTL digital signal by filtering the undesirable noise, regulating the maximum and minimum voltages, suppressing the unwanted minor signal fluctuation in *Rclk*, and supplying more current to the signal. We use multiple non-inverting buffer logic gates in parallel to accomplish the enhancement as shown in **Fig 3.5a**. Our method to enhance *Rclk* into *Rclk'* is one method out of many other feasible methods to enhance *Rclk*.

The custom electrical circuit generates *Ltrig* through the frequency doubler electrical circuit shown in **Fig 3.5a**. The frequency doubler generates a short square pulse when the *Rclk'* shows a state transition either from off-state to on-state (rise) or from off-state to on-state (fall) as illustrated in **Fig 3.5b**. The train of the short square pulses

comprises *Ltrig*. We build the frequency doubler electrical circuit with multiple non-inverting buffer logic gates, multiple capacitors, and one XOR logic gate. The non-inverting buffer logic gates and the capacitors introduce a delay to *Rclk'*. The original *Rclk* without the delay and the *Rclk'* with the delay are sent to the two input terminals of the XOR logic gate. The output of the XOR gate results in *Ltrig*. Our design of the frequency doubler is one design to realize the frequency doubler among many other possible designs.

Scanning mirror drivers

The resonant scanning mirror driver controls only the tilting amplitude of the resonant scanning mirror based on the *Rsig* provided by the MDAQ. Simultaneously, the resonant scanning mirror driver provides *Rclk* to indicate the beginning of one tilting period of the resonant scanning mirror. However, the resonant scanning mirror driver cannot fix the resonant scanning mirror at a tilting position since the resonant scanning mirror must continuously move. The galvanometric scanning mirror driver controls the tilt position of the galvanometric scanning mirror based on *Gsig* given by the MDAQ. Unlike the resonant scanning mirror driver, the galvanometric scanning mirror driver can fix the galvanometric scanning mirror at a tilting position upon the order of *Gsig*. Both the resonant and galvanometric scanning mirror drivers demand heat sinks and fans for thorough cooling. When the scanning mirror drivers are not properly cooled, the scanning mirror drivers malfunction, and cannot provide appropriate laser beam scanning for imaging. The galvanometric scanning mirror driver is especially more susceptible to heat than the resonant scanning mirror driver is.

Stage controller

30

The stage controller drives both the motorized XYZ stage and the z-axis piezo stage obeying the *Ssig* from MDAQ. The stage controller operates the motorized XYZ stage for all movements in the x-axis and the y-axis, and over 100 μm movements in the z-axis, and commands the piezo stage for z-axis movements shorter than 100 μm, especially for high-resolution z-stack imaging, and high-speed time-lapse volumetric imaging since the piezo stage is far superior in precision and responsiveness to the motorized stage. The stage controllers also receives commands directly from the custom confocal computer when appropriate.

High-speed digitizer

The high-speed digitizer acquires and samples the specimen's fluorescent photon intensity information given in the form of an electrical signal from the preamp. The high-speed digitizer is capable of a sampling rate up to 180 mega samples per second (MS/s), which our confocal microscope uses. The high-speed digitizer uses *Rclk'* and *Ftrig* as trigger signals to synchronize the high-speed digitizer's data sampling with the laser beam specimen scanning in the optical system. The high-speed digitizer uses a sampling bit depth of 16 bit. Hence, our confocal microscope can provide images with pixel intensity precision higher than imaging systems using cameras, and data acquisition methods with bit depths less than 16 bit.

The high-speed digitizer is capable of continual data acquisition and sampling uninterrupted by the data transfer between the high-speed digitizer memory and the computer memory. This uninterrupted continual data acquisition and sampling is crucial in achieving a fast imaging speed. The data acquired and sampled by the high-speed digitizer is temporarily stored on the high-speed digitizer memory, and the data must be transferred to the computer memory to be either stored or processed by the computer before the high-

31

speed digitizer memory is overflown by new incoming data. Certain high-speed digitizers or data acquisition cards have to halt data acquisition and sampling while they transfer data from their memory to the computer memory. That data acquisition and sampling halt significantly decreases the imaging speed of a scanning microscopy system, moreover, the duration of the halt is proportional to the amount of data that needs to be transferred. Hence, the uninterrupted continuous data acquisition and sampling is critical in achieving a fast imaging speed by preventing a possible time waste.

Custom confocal software

The custom confocal software (confocal software) written by LabVIEW (National Instruments) is the main interface for microscope users to interact with the confocal microscope. Upon receiving *Uin*, The confocal software written by LabVIEW computes and creates the waveforms (*Wfm*) of the electrical signals that MDAQ generates based on the user input (*Uin*) for the imaging condition. The *Wfm* that the confocal software creates are *Rsig*, *Ftrig*, *Gsig*, and *Ssig*. The following sub-chapter, **3.2.4. Control signal generation**, explains the principles of the waveform computation for *Rsig*, *Ftrig*, *Gsig*, and *Ssig* in detail. The confocal software can control the MDAQ, the stage controllers, and the high-speed digitizer independently outside the confocal imaging operations when users need them for non-imaging purposes such as aligning the optical system, and calibrating the control and synchronization signals.

Additionally, the confocal software processes raw data sampled by the high-speed digitizer into human-recognizable two-dimensional (2D) images. The confocal software saves both the raw data and the 2D images upon user requests. The confocal software displays the 2D images, and also performs modest real-time image processing to assist users with convenient image viewing such as setting an appropriate intensity look-up table,

or adjusting the dynamic range window of pixel intensity. Lastly, the confocal software is written to be prepared for any additional modification for future applications involving the confocal microscope as a substantial advantage in developing a piece of custom software. Thus, the confocal microscope is a basis for the studies in **Chapter 4** and **Chapter 5**.

Custom confocal computer

The custom confocal computer (confocal computer) houses the MDAQ, the high-speed digitizer, and the confocal software. The confocal computer incorporates an Intel core i7-4790 (3.6 GHz) CPU, 32 GB DDR3 memory, and a 500 GB solid-state drive (SSD), and a 1 TB SSD. The Intel CPU, the most powerful CPU with the most cores at the time of purchase, enables prompt and efficient data processing for the confocal software designed to benefit from multicore processors. The 32 GB memory provides plenty of buffer memory space where the confocal software safely keep unprocessed or unsaved data even under unexpected delays in data processing and saving, and abrupt lags caused by random processes in the operating system. The 32 GB memory also enables image processing and numerical analysis tools to handle a large amount of image data at once when image data needs extensive post-processing or data analysis.

The SSDs enable the confocal software to continuously and stably save data from the high-speed digitizer in real time. The high-speed digitizer acquires data at 180 MS/s rate, thus generates 360 MB of new data every second because one sample is 2 bytes (16 bit). In order to save data at 360 MB/s, the data transfer speed between the computer memory and the storage device, and the writing speed of the storage device must be faster than 360 MB/s. If the data transfer and writing speed is slower than 360 MB/s, the high-speed digitizer must cease data acquisition when the computer memory is completely full of data to save, or the confocal software malfunctions due to an error caused by the data

33

overflow in the high-speed digitizer memory. The state-of-the-art mechanical hard disk drives (HDDs) demonstrate a data transfer speed and writing speed of 200 MB/s at best as a single drive bottlenecked by the HDD spindle motor speed, hence cannot achieve the minimum required speed of 360 MB/s. Multiple HDDs can achieve a data transfer and writing speed higher than 360 MB/s when they are striped in parallel on a RAID (redundant array of independent disks) system. However, the multi-HDD striping on RAID is greatly costly, and more cumbersome to manage and maintain compared to a single HDD system.

On the contrary, the recent consumer-level SSDs using the SATA interface easily provide a data transfer and writing speed of 500 MB/s on average as a single drive, and are substantially more economical than building a multi-HDD RAID system. Particular state-of-the-art SSDs using the PCIe interface deliver a data transfer and writing speed of 2,000 MB/s. If our confocal microscope is upgraded to be a multicolor system, the upgraded confocal microscope will generate image data at minimum 720 MB/s, inevitably, only SSDs will be able to transfer and write data at such high speed. Additionally, SSDs are more reliable as a data storage device than mechanical HDDs since SSDs have no mechanical components such as spindle motors that are a common cause of HDD failure due to mechanical degradation over time. The 1 TB SSD in the confocal computer is dedicated only to data saving for the confocal software to further stabilize the data transfer, while the other 500 GB SSD contains and runs the operating system, the confocal software, and miscellaneous data.
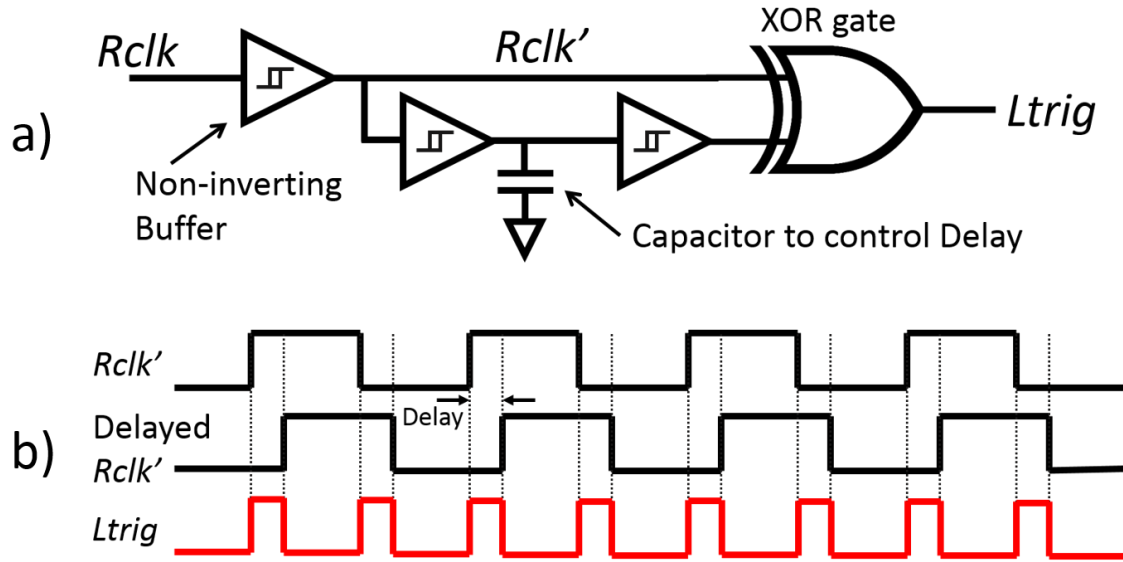
Figure 3.5: Signal refiner and frequency doubler circuit. (a) Frequency doubler logic circuit. (b) *Ltrig* generation by XOR gate.

3.2.4. Control and synchronization signals

This subchapter presents the descriptions and the waveform generation principles of the control and synchronization signals shown in **Fig. 3.4**. The confocal software computes, then creates the control and synchronization signal waveforms (*Wfm*) using the user input (*Uin*) for the MDAQ to generate the control and synchronization signals for the confocal microscope. The *Uin* contains imaging parameters given by users of the confocal microscope. While the confocal software computes *Uin*, the confocal software also calculates additional imaging parameters essential to create *Wfm*. The imaging parameters are as follows:

FOV_X ≡ Field-of-view in x-axis (horizontal field-of-view) (μm)

FOV_Y ≡ Field-of-view in y-axis (vertical field-of-view) (μm)

FOV_Z ≡ Field-of-view in z-axis (imaging depth) (μm)

OBJ_NA ≡ Numerical aperture of the objective

OBJ_M ≡ Magnification of the objective

OBJ_IM ≡ Refractive index of the imaging medium of the objective

OBJ_TF ≡ Standard focal length of the tube lens for the objective

OBJ_WL ≡ Wavelength of the excitation light source (μm)

OBJ ≡ Collection of OBJ_NA, OBJ_M, OBJ_IM, OBJ_B, and OBJ_WL

NV_X ≡ Number of voxels in x-axis

NV_Y ≡ Number of voxels in y-axis

NV_Z ≡ Number of voxels in z-axis (number of imaging planes)

VOX_X ≡ X dimension of the voxel (μm)

VOX_Y ≡ Y dimension of the voxel (μm)

VOX_Z ≡ Z dimension of the voxel (μm)

VOX ≡ Voxel volume size, VOX_X × VOX_Y × VOX_Z (μm × μm × μm)

FOV_X, FOV_Y, FOV_Z, NV_Z, OBJ, NV_Y, and VOX must be given by *Uin* though the confocal software provides theoretically estimated values for NV_X, NV_Y, and VOX to assist users. Then, all of those imaging parameters participate in creating waveforms of the control and synchronization signals.

The confocal software first calculate NV_X, NV_Y, and VOX upon receiving *Uin*. The calculation and generation flow of the imaging parameters, and the control and synchronization signal waveforms is illustrated in **Fig. 3.6**.
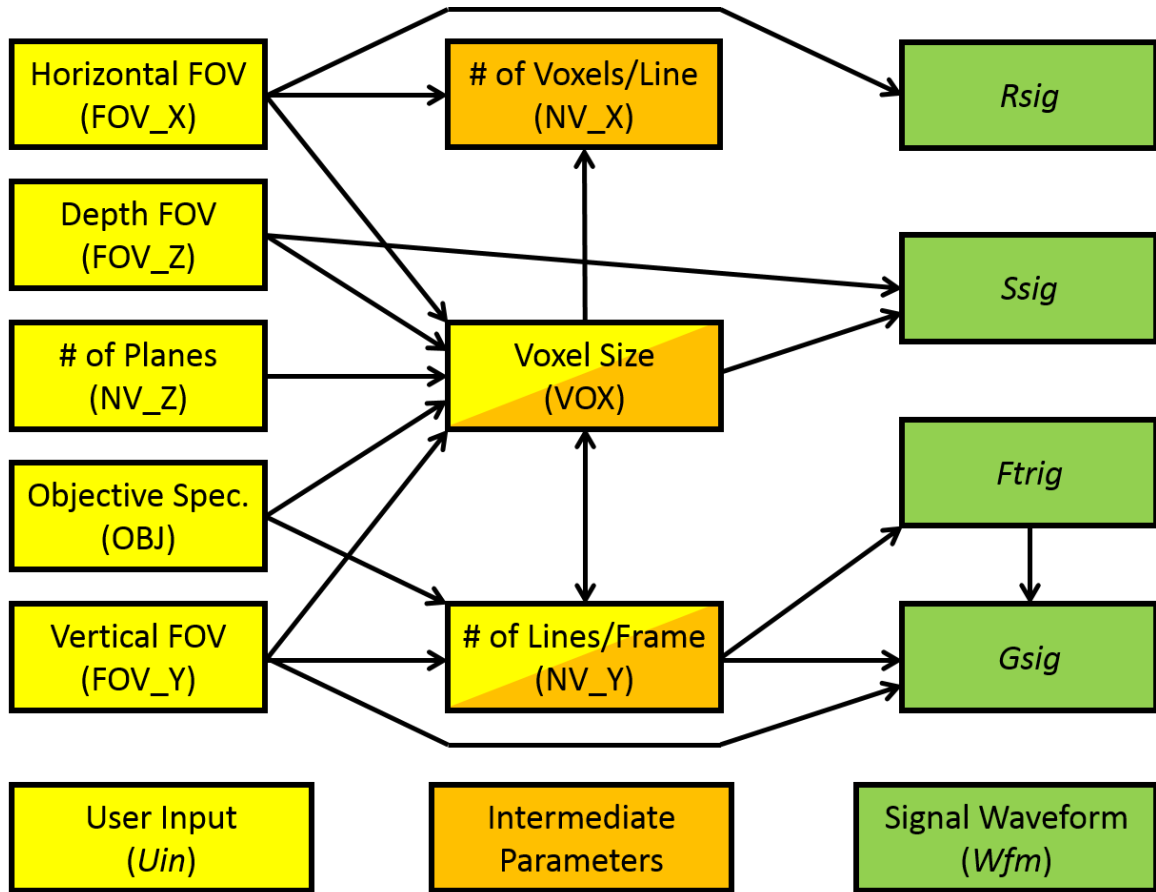
Figure 3.6: Calculation and creation flow of the imaging parameters, and the control and synchronization signal waveforms. The yellow boxes are the imaging parameters given by *Uin*, the orange boxes intermediate imaging parameters calculated by the confocal software, and the green boxes *Wfm*. The arrows indicate the flow of parameter and *Wfm* calculation.

Voxel volume size (VOX)

The confocal software requires users to provide values for the imaging voxel volume size (VOX). At the same time, the confocal software calculates the VOX theoretically ideal for the microscope objective used for imaging to help users decide values for VOX. The VOX must be either equal to or less than half of the imaging resolution determined by OBJ_NA, OBJ_WL, and OBJ_IM [102], [103]. VOX is mathematically given by

$$VOX\_Y = VOX\_X = \frac{0.61 \times OBJ\_WL}{2 \times OBJ\_NA} \tag{3.8}$$

$$VOX\_Z = \frac{OBJ\_IM \times OBJ\_WL}{2 \times OBJ\_NA^2} \tag{3.9}$$

Number of voxels in x-axis, and y-axis (NV_X, NV_Y)

Similar to VOX, the confocal software also requires users to decide NV_Y and NV_Z though the confocal software shows theoretically optimal values for NV_Y and NV_Z to properly sample the field-of-view in y-axis based on OBJ, and FOV_Y obeying the Nyquist criterion. NV_Y and NV_Z that the confocal software automatically estimates are given by

$$NV\_Y = \left\lceil \frac{FOV\_Y}{VOX\_Y} \right\rceil \tag{3.10}$$

$$NV\_Z = \left\lceil \frac{FOV\_Z}{VOX\_Z} \right\rceil \tag{3.11}$$

If users choose NV_Y and NV_Z values dissimilar to the values suggested by the confocal software, then instead of Eqn. (3.8) and (3.9), VOX_Y and VOX_Z are given by

$$VOX\_Y = VOX\_X = \frac{FOV\_Y}{NV\_Y} \tag{3.12}$$

$$VOX\_Z = \frac{FOV\_Z}{NV\_Z} \tag{3.13}$$

38

The confocal software always appoints VOX_X to the same value as VOX_Y in order to keep the voxel aspect ratio one-to-one. Otherwise, the confocal microscope will produce wrongly scaled images. Once both VOX_Y, and VOX_Z are ready, the confocal software calculates NV_X, which is described as

$$NV\_X = \left\lceil \frac{FOV\_X}{VOX\_X} \right\rceil \tag{3.14}$$

NV_X, NV_Y, and NV_Z have to natural numbers, and NV_Y especially has to be an even natural numbers because one period of the resonant mirror's tilting creates two lines in an image frame. After the necessary imaging parameters are ready, the confocal software proceeds to create waveforms (*Wfm*) for the control and synchronization signals. The waveforms of the control and synchronization signals are plotted in **Fig. 3.7**.

Resonant mirror reference clock signal (*Rclk*)

The resonant mirror reference clock signal (*Rclk*) notifies the beginning of each tilting cycle of the resonant mirror. *Rclk* is the electrical voltage signal provided by the resonant mirror driver electronics. *Rclk* mostly follows the TTL (transistor-transistor logic) digital signal standard where the voltage between 0 V and 0.8 V represents the off-state and the voltage between 2 V and 5 V represents the on-state. The one period of *Rclk* is 126.4 μs, and the duty cycle is 50 %, which means 50% of one period is in the on-state, and the other 50% of one period is in the off-state. The on-state and the off-state represent the scanning directions opposite to each other. The quality of *Rclk* could be poorer than the expected standard due to the quality of the resonant mirror driver electronics or electrical

noise from the surroundings, hence, enhancing *Rclk* via an electrical circuit is preferable to achieve a stable operation.
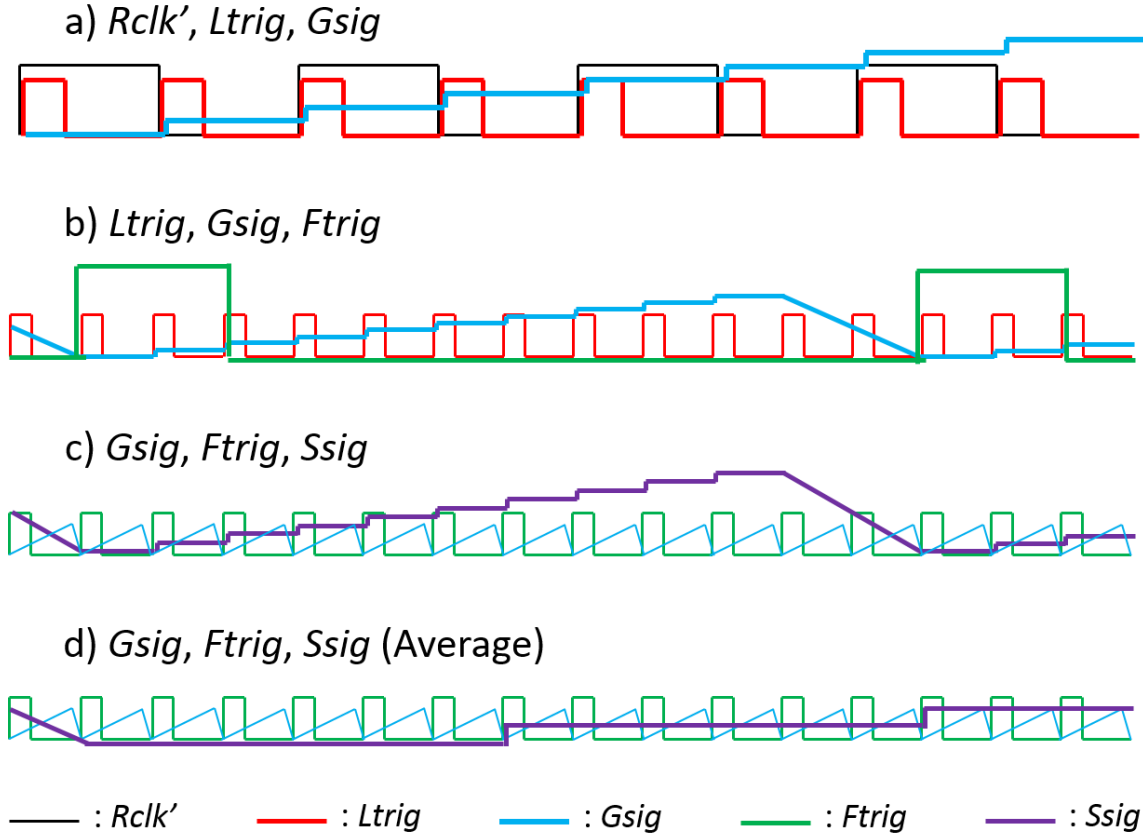
Figure 3.7: Plots of control and synchronization signals. (a) *Rclk'*, *Ltrig*, and *Gsig* for 8 lines of a frame. (b) *Ltirg*, *Gsig*, and *Ftrig*. One full frame (10 lines) and a portion of a frame (3 lines). (c) *Gsig*, *Ftrig*, and *Ssig*. One full volume (10 frames) and a portion of a volume (3 frames). (d) *Gsig*, *Ftrig*, and *Ssig*. 2.5 planes. Each plane consists of 6 averaged frames. The fly-back phase of *Ltrig* is shorted to 2 for simplicity.

Enhanced resonant mirror reference clock signal (*Rclk'*)

The enhanced resonant mirror reference clock signal (*Rclk'*) is the electrical signal generated by the custom electronic circuit by enhancing *Rclk* as shown in **Fig. 3.5**. *Rclk'* strictly follows the TTL digital signal standard, thus, delivers reliability superior to that of

40

Rclk while *Rclk'* delivers the same function as *Rclk* does. However, *Rclk'* may manifest tens of nanoseconds of time delay to *Rclk* introduced by the custom electrical circuit. The delay can be compensated by adjusting the phase delay controller for *Rclk* on the resonant mirror driver.

Line trigger signal (Ltrig)

The line trigger signal (*Ltrig*) notifies the beginning of each line scanning, and also indicates the timing for the galvanometric mirror to move. *Ltrig* is also the base timing unit for the control and synchronization signals. The lengths of the control and synchronization signals are described in the length of *Ltrig*'s period. *Ltrig* is generated by the custom electronic circuit by processing *Rclk'* as shown in **Fig. 3.5**. *Ltrig* obeys the TTL digital signal standard, however the duty cycle of *Ltrig* is significantly less than 50 % though the minute duty cycle does not interfere with *Ltrig*'s function. If necessary, Ltrig's duty cycle can be increased by applying a longer time delay between the two inputs of the XOR gate in **Fig 3.5b**. *Ltrig*'s one period is 63.2 us, which is half of *Rclk*'s one period. *Ltrig* works as the reference timing clock for the frame trigger signal (*Ftrig*), the galvanometric mirror control signal (*Gsig*), and the stage control signal (*Ssig*) when the MDAQ generates the control and synchronization signals.

Resonant mirror scanning angle control signal (Rsig)

The resonant mirror scanning angle control signal (*Rsig*) decides the scanning angle of the resonant mirror. The scanning angle of the resonant mirror is linearly proportional to the voltage of *Rsig*, which is a constant rather than a waveform. The voltage of *Rsig* is determined mainly by FOV_X, and the full field-of-view that the combination of the confocal microscope and the installed microscope objective can provide (Eqn. (3.7)). Thus,

Rsig is proportional to FOV_X and OBJ_M, and inversely proportional to OBJ_TF. *Rsig* accepts a voltage between 0 V and 5 V, and *Rsig* of 5 V sets the resonant mirror's tilting angle its maximum. Therefore, *Rsig* is given by

$$Rsig = 5 \times \frac{\text{FOV\_X}}{FOV_{MAX,x}} = 5 \times \frac{\text{FOV\_X}}{2 \times (\text{OBJ\_TF}/\text{OBJ\_M}) \times 39} \ (\text{V}) \qquad (3.15)$$

where OBJ_TF is 200 mm, and 180 mm for Nikon, and Olympus microscope objectives, respectively. *Rsig* has to be higher than 1 V because *Rsig* lower than 1 V results in a malfunction of the resonant mirror driver. Thus, FOV_X must be higher than 10 % of the full field-of-view.

Galvanometric mirror control signal (*Gsig*)

The galvanometric mirror control signal (*Gsig*) administers the tilting angle of the galvanometric mirror. *Gsig* is a sawtooth waveform whose voltage ranges from negative to positive values. The positive voltage turns the galvanometric mirror clockwise, and the negative voltage counter-clockwise. The amplitude of *Gsig* is linearly proportional to FOV_Y. One period of *Gsig* consists of two phases: the imaging phase, and the fly-back phase. During the imaging phase, the galvanometric mirror discretely alters its deflection angle to shift the scanning excitation laser line along the y-axis of the field-of-view. During the fly-back phase, the galvanometric mirror returns to its initial deflection angle at the beginning of one period. The discrete increment of the galvanometric mirror's deflection angle is determined by FOV_Y, NV_Y, and the full field-of-view in y-axis. The full field-of-view in y-axis is slightly wider than that in x-axis because the maximum deflection angle of the galvanometric mirror is 20 °, which is larger than the resonant mirror's maximum deflection angle of 15 °.

42

One period of *Ltrig* is NV_Y + 12 long. The length of the imaging phase is NV_Y, and the length of the fly-back phase is 12. The length of the fly-back phase is based on the required time for the galvanometric mirror to return. The galvanometric mirror can make a one full round trip within 1 ms referring to the specification of the galvanometric mirror. Since the return process is equivalent to half of one full round trip, the fly-back phase is estimated to take 0.5 ms, which approximately equals the time necessary to scan 8 lines. Having considered an error buffer, and a vibration settling time, the length of the fly-back phase is chosen to be 12. Hence, taking into account the aforementioned conditions, the one unit period of *Gsig* is given by

$$
Gsig = \begin{cases} 10 \times \dfrac{FOV\_Y}{FOV_{MAX,y}} \times \left\{ \dfrac{(n-1) - NV\_Y/2}{NV\_Y} \right\}, & \text{if } 1 \leq n \leq NV\_Y \\[4mm] 10 \times \dfrac{FOV\_Y}{FOV_{MAX,y}} \times \left\{ \dfrac{(NV\_Y - n) + 6}{12} \right\}, & \text{if } NV\_Y < n \leq NV\_Y + 12 \end{cases} \tag{3.16}
$$

where n is a natural number equal or larger than 1, and $FOV_{MAX,y}$ is equal to $FOV_{MAX,x}$ in Eqn. (3.15) except 39 in $FOV_{MAX,x}$ is replaced with 52 due to the maximum deflection angle of the galvanometric mirror larger than that of the resonant mirror. The relationship between *Ltrig* and *Gsig* is illustrated in **Fig. 3.7a** and **Fig. 3.7b**. Every *Ltrig* raises n by 1, hence, updates *Gsig*. n begins at 1, increases by 1, and returns to 1, after the end of one period, NV_Y + 12. In the example shown in **Fig. 3.7b**, the period of *Gsig* is 12, 10 for the imaging phase, and 2 for the fly-back phase being shortened for simplicity.

Frame trigger signal (*Ftrig*)

The frame trigger signal (*Ftrig*) determines the beginning of each frame acquisition. *Ftrig* signals the high-speed digitizer of when the data acquisition of a new frame has to

commence. *Ftrig* obeys the TTL digital signal standards. The length of one period of *Ftrig* is identical to that of *Gsig* since one period of both *Ftrig* and *Gsig* is the required time to complete imaging the field-of-view once. The duty cycle of FT is set 10 % though the duty cycle can be any value between 5 % and 50 %.

$$Ftrig = \begin{cases} 5, & \text{if } 1 \leq n \leq DC \times \left(NV\_Y + 12 \right) \\ 0, & \text{if } DC \times \left(NV\_Y + 12 \right) < n \leq NV\_Y + 12 \end{cases} \tag{3.17}$$

where *n* is the same natural number in Eqn. (3.16). *DC* is the duty cycle between 0.05 and 0.5. An example of *Ftrig* is shown **Fig. 3.7b** where the period of *Ftrig* is 12 equal to that of *Gsig*, and the on-state of *Ftrig* is 2 *Ltrig*'s periods long. Lastly, when *Ftrig* is converted to an electrical signal by MDAQ, and delivered to the high-speed digitizer, the beginning of one period of *Ftrig* must reach the high-speed digitizer earlier than that of *Ltrig* since the high-speed digitizer recognizes *Ltrig* only after the high-speed digitizer receives the on-state from *Ftrig*. Delaying *Ltrig* by a couple of microseconds assures *Ftrig* arrives the high-speed digitizer earlier than *Ltrig*.

Stage control signal (*Ssig*)

The stage control signal (*Ssig*) contains signals for both the motorized XYZ stage and the piezo stage dedicated to specimen's z-axis movement. The confocal software creates a waveform only for the piezo stage by default because the z-axis movement requires synchronized automation for efficient 3D imaging. Movements in x-axis and y-axis are necessary often only at the beginning of an imaging session to locate the specimen. The confocal software also creates two types of *Ssig* waveforms for averaged and non-averaged imaging operations. The averaged imaging obtains high SNR and resolution

44

images, and the non-averaged imaging acquires time-lapse images for monitoring specimens' dynamics.

Ssig is a sawtooth waveform whose amplitude is linearly proportional to the moving range (FOV_Z) given by Uin. Ssig updates its value for every Ftrig on-state transition, and the length of Ssig's one period is NV_Z × (NV_Y + 12) since the stage must stay at a z-position at least for imaging of a frame. One period of Ssig also consists of two phases, the imaging phase, and the fly-back phase though the fly-back phase of Ssig is almost negligible compared to that of Gsig. The discrete increment of Ssig is VOX_Z = FOV_Z/NV_Z. Hence, Ssig for imaging is given by

$$Ssig = \begin{cases} \dfrac{\text{FOV\_Z}^2}{8\text{NV\_Z}} \times \left\lfloor \dfrac{n-0.1}{k(\text{NV\_Y}+12)} \right\rfloor, & \text{if } 1 \le n \le \text{NV\_Z} \times (\text{NV\_Y}+12) \\ 0, & \text{if } \text{NV\_Z} \times (\text{NV\_Y}+12) < n \end{cases} \quad (3.18)$$

where FOV_Z/8 is a coefficient for the stage controller input, and k is the number of frames to average for each plane. k is 1 for non-averaged imaging. Examples of Ssig for non-averaged imaging and averaged imaging are illustrated in **Fig. 3.7c** and **Fig. 3.7d**, respectively. In the example in **Fig. 3.7c**, NV_Z is 10, and the fly-back phase is exaggerated to be 2 Ftrig periods long for illustration purposes, however, the fly-back phase is approximately 40 Ltrig periods (2.5 ms) long in actual operations. In the example in **Fig. 3.7d**, 6 frames are averaged to form an image for a plane, hence Ssig remains the same value for 6 Ftrig periods.

3.2.5. Custom confocal software

The custom confocal software manages the electrical components to control the optomechanical components, and to acquire data. The confocal software processes acquired data into correct human-recognizable 2D images. The confocal software also provides the interface for users to interact with the confocal microscope. The confocal software consists primarily of two parts: (1) imaging software for data acquisition, saving, and display, and (2) processing software for image construction and correction. The confocal software is separated in those two parts to maximize the efficiency of the software since conducting data acquisition, image construction and correction, saving, and displaying altogether requires a great deal of computing power, thus, may cause data flow congestion, and process interruption resulting in software errors, especially data acquisition errors. Hence, the image processing and correction function is divided from the rest of the confocal software because the image construction and correction demands the most computing power. Lastly, the confocal software is written in LabVIEW (National Instruments) for LabVIEW's strength in straight-forward implementation of the graphical user interface (GUI), and LabVIEW's complete support for National Instruments' device, MDAQ, however, the confocal software can be written in any other programming languages.

The structure of the confocal imaging software is shown in **Fig. 3.8**. The imaging software comprises three main threads: (1) the imaging thread, (2) the mirror and stage control thread, and (3) the main control thread. The functions of the three threads are mostly independent from one another yet they can still communicate though the main control thread administers the other threads' operations.

Imaging thread

The imaging thread of the confocal imaging software consists of three sub-threads: (i) the data acquisition thread, (ii) the image processing thread, and (iii) image saving and display thread. The data acquisition thread manages the high-speed digitizer for data acquisition. The data acquisition thread configures the high-speed digitizer according to the imaging condition (*Uin*) given by users, and collects and temporarily stores data in the onboard memory of the high-speed digitizer. Subsequently, the data acquisition thread transfers the collected data temporarily stored in the onboard memory to the image processing thread (*DF1* in **Fig. 3.8a**). In this process, the data in the onboard memory is also conveyed to the main memory of the confocal computer (*DF1* in **Fig. 3.8b**). The high-speed digitizer uses the PCIe 4× interface to communicate with the main memory (DDR3, PC-8500). The PCIe 4× interface can theoretically transfer data at 3.6 GB/s rate, and the main memory can theoretically transfer data at 8.5 GB/s. Hence, the data transfer rate between the onboard memory of the high-speed digitizer and the main memory of the confocal computer is sufficient to handle the data acquisition rate of 360 MB/s by the high-speed digitizer.

The image processing thread of the imaging thread transforms the data delivered from the data acquisition thread into 2D images which human eyes easily recognize. The data from the data acquisition thread are 1D arrays of 16 bit unsigned integers. These 1D arrays provides no direct information of specimens' features. Thus, those 1D arrays needs to be converted into human-eye identifiable 2D images. However, the image processing thread conducts only simplified and abridged image construction because the thorough image construction and correction demands a great amount of computing power and time, thus may cause the buffer overflow error in the imaging thread. Another function of the image processing thread is to correct the pixel shift offset between the odd lines and the

even lines due to a minute difference in the number of pixels between the odd and the even lines. This pixel shift offset correction is discussed in detail later. Lastly, the image processing thread passes both the 1D array data and the constructed 2D data onto the image saving and display thread.

The image saving and display thread saves image data and displays images processed by the image processing thread. The image saving function of the thread saves the 1D array data with no applied processing in the storage device, the SSD, in our confocal computer. Saving the unprocessed 1D array is more preferable than saving the processed 2D images since the unprocessed 1D arrays can be reprocessed repeatedly in case any error is found in the processing algorithm, or a more accurate processing method is developed. In the course of 1D array data saving, the data travels from the main memory of the computer to the storage device in the computer as shown as *DF2* in **Fig. 3.8b**. As explained in **3.2.3. Electrical system**, the data transfer rate between the main memory and the storage device (500 MB/s) must be higher than the data acquisition rate in the data acquisition thread (360 MB/s).

The image display function shows the constructed 2D images from the image processing thread on the display device such as a LCD monitor. The image display function also enlarges, or reduces the displaying image size upon users' requests for convenient viewing. The image display function also enables users to define a region-of-interest (ROI) on the image display, and shows the image of the ROI separately. Additionally, the image display function applies various lookup tables and intensity dynamic windows upon users' requests to assist users' visual inspection of the constructed images.

The three sub-threads of the imaging threads execute in parallel. The data transfers among the threads are pipelined with sufficient buffer memory so that the whole pipelined multi-threading is protected from data transfer congestion and buffer overflow errors.
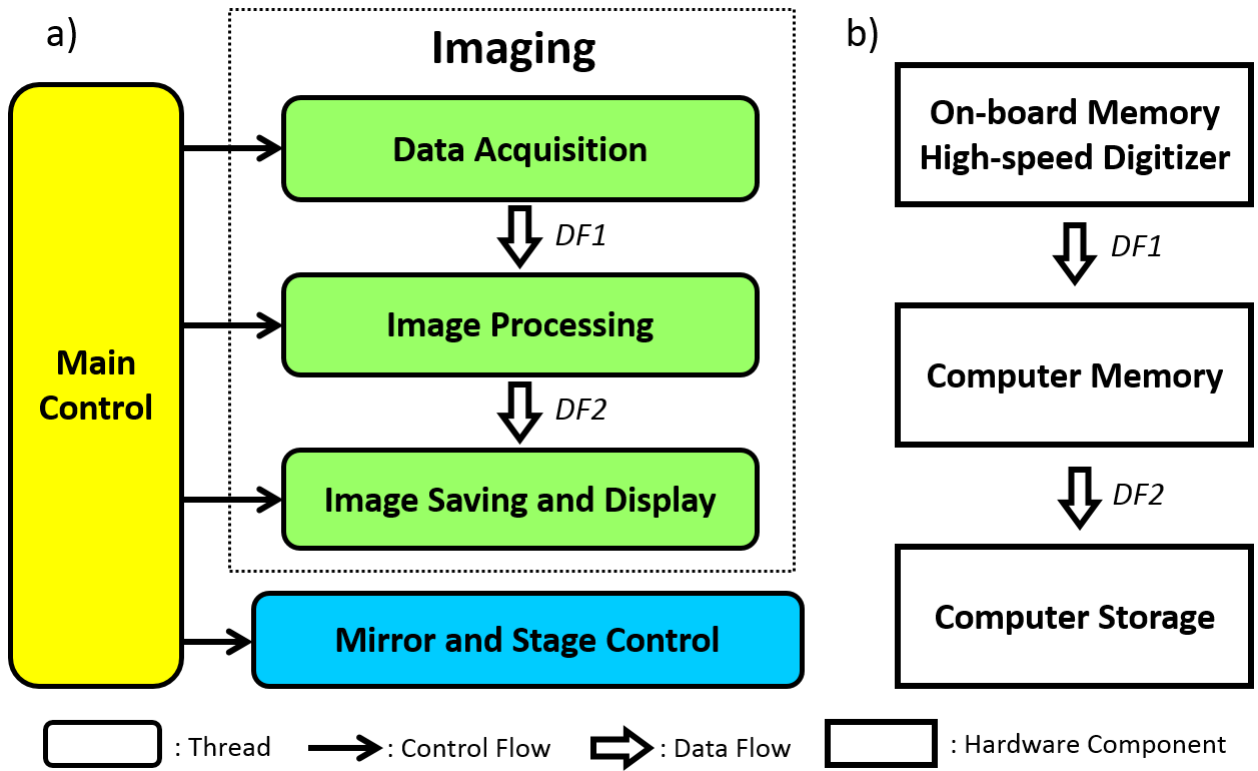
Figure 3.8: The structure of the confocal imaging software and the image data flow in the software and the computer. (a) The confocal imaging software structure. Imaging and data acquisition process and control process. (b) The image data flow from the high-speed digitizer to the computer storage.

Mirror and stage control thread

The mirror and stage control thread is in charge of the control and synchronization of the scanning mirrors and the motorized and piezo stages. The mirror and stage control thread creates the control and synchronization signal waveforms described in **3.2.4. Control and synchronization**, generates the control and synchronization signals through the MDAQ. The stage control function of the thread also commands the motorized and piezo stages independent of the control and synchronization signals upon users' requests. The mirror and stage control thread is prepared for custom control and synchronization

signal sequences designed for specific imaging applications such as automated sequential imaging of multiple specimens.

Main control thread

The main control thread administers the whole confocal software including the aforementioned imaging, and mirror and stage control threads. The main control thread initializes the confocal software by preparing the devices used by the confocal software, setting the control parameters and variables to their default values, and clearing up the buffer memory for data acquisition and image processing. The main control thread also directs the sub-threads of the imaging threads individually. For instance, the main control thread can turn off the image construction of the image processing thread, and the display function of the image saving and display thread while keeping the saving function on to concentrate the computer's resources on stable data acquisition and image saving. Additionally, the main control thread is capable of executing the sub-threads of the imaging thread and the mirror and stage control thread in timely sequenced manners for custom automation applications. Lastly, the main control thread properly ends the confocal software by emptying the buffer memory, and releasing the devices used by the confocal software from the software so that other software can use them without experiencing glitches.

Post-processing: 1D array to 2D image conversion

Once images are stored as 1D arrays of 16 bit unsigned integers, the 1D arrays must be transformed into 2D images that present proper information of target specimens, and human eyes intuitively recognize. To correctly transform 1D arrays into 2D images, the formation principle of the 1D arrays must be first accurately comprehended. **Figure 3.9a**

and **Figure 3.9b** show an example specimen simplified for efficient explanation, and the 1D array that the confocal software generates by imaging the example specimen, respectively. The example specimen consists of two lines who comprise 10 pixels each. The first line incorporates from 0 (left) to 9 (right), and the second line from A (left) to J (right). When the example specimen is imaged, the excitation laser beam scans the first line from left to right, while the second line from right to left since the resonant mirror scans the beam bidirectionally. However, the data acquisition of the high-speed digitizer is unidirectional, hence the second line is saved in the opposite direction in the 1D array as shown in **Fig. 3.9b**.

In addition, a small portion in the leftmost part of the second line is not saved in the 1D array. In **Fig. 3.9b**, 2 pixels (A, and B) are missing, which are exaggerated as 20 % for convenience. The resonant mirror takes 126.4 μs to complete one round tilting, 63.2 μs for each direction. However, the high-speed digitizer cannot take advantage of the full 126.4 μs for data acquisition since the high-speed digitizer requires $1 - 2$ μs to rearm its trigger electronics, and that $1 - 2$ μs is also spared for the galvanometric mirror to change its angle. Thus, data worth $1 - 2$ μs, approximately 2 % of one line is unsaved in the 1D array though the missing data portion is significantly less than 1 % in terms of the field-of-view. The missing portion in terms of the field-of-view is discussed in the upcoming paragraphs about correction of image stretching due to the resonant mirror's inconsistent tilting velocity.

The following parameters are used in the 1D array to 2D image conversion.

$N_{HS} \equiv$ Number of pixels per line before stretch correction. 9 in **Fig. 3.9**

$N_H \equiv$ Number of pixels per line (NV_X in **3.2.4.**)

$N_V \equiv$ Number of lines per frame (NV_Y in **3.2.4.**). Even number. 2 in **Fig. 3.9**

$N_{1D} \equiv$ Number of data points in the 1D array, 18 in **Fig. 3.9**

51

$N_S \equiv$ Number of pixels to shift for correction, 1 in **Fig. 3.9**

$N_{ZP} \equiv$ Number of zero-padded pixels, 1 in **Fig. 3.9**

A 1D array of unsigned integer data points saved by the confocal microscope has in total N_{1D} data points, and N_{1D} is given by $N_{1D} = (N_{HS} - N_S) \times N_V$. The 1D array to 2D image conversion (1D to 2D conversion) first arranges the 1D array data points into a 2D array that has N_V rows and $(N_{HS} - N_S)$ columns (**Fig. 3.9b** to **Fig. 3.9c**). The data points in the even numbered rows in the 2D array are oriented in the direction opposite to those of the correct image, thus, the 1D to 2D conversion reverses the even numbered rows (**Fig. 3.9c** to **Fig. 3.9d**). At this point, the odd numbered lines and the even numbered lines have the same number of data points though the even numbered lines have a small portion (N_S) of data points that actually belong to the odd numbered lines above the even numbered lines (9 in **Fig. 3.9d**). Moreover, the data points in the even numbered lines are pushed to the left by $2N_S$, and needs to be shifted to their correct positions (**Fig. 3.9d**). Hence, the 1D to 2D conversion shifts the data points in the even numbered lines to the right by $2N_S$, and moves up to the odd numbered lines the N_S data points that belong to the odd numbered lines, yet are in the even numbered lines (**Fig. 3.9e** to **Fig. 3.9f**).
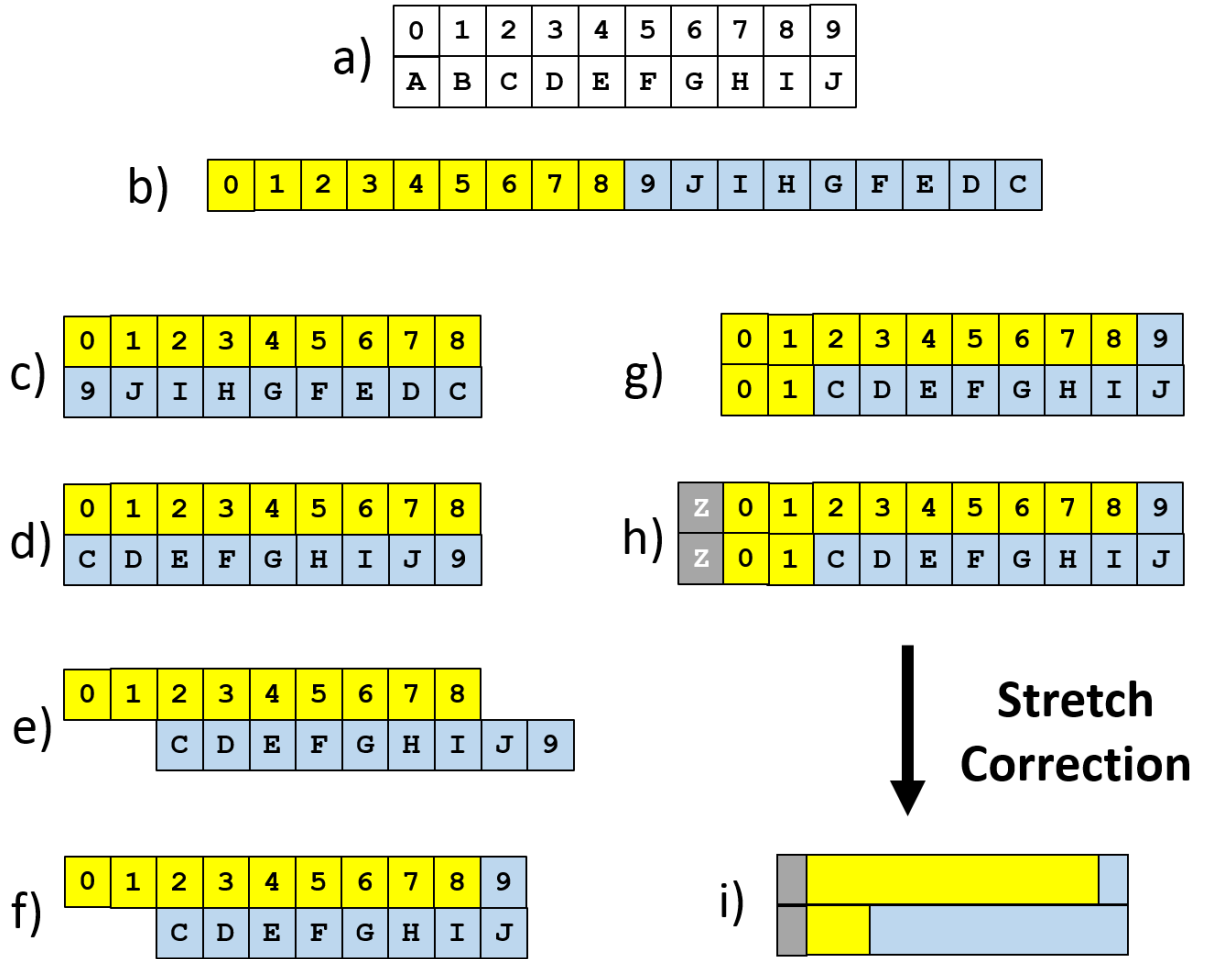
Figure 3.9: The procedures of image construction from 1D array of data points. (a) Example target specimen. (b) – (i) in the order of the procedures. (b) 1D array of data points sampled from the example target specimen. (c) 2D array converted from the 1D array in (b). (d) Reversed even numbered line. (e) Pixel shift correction. (f) Pixel location correction. (g) Filling missing pixels. (h) Padding dummy pixels. (i) Completely constructed image after stretch correction.

After the data point shifting in the even numbered lines, the even numbered lines have empty $2N_S$ data points in the very left, which are missing due to the $1 - 2$ μs discrepancy between the resonant mirror period and the data acquisition time as explained in the previous paragraph (**Fig. 3.9f**). The 1D to 2D conversion fills the empty $2N_S$ data points with the data points in the exactly identical positions in the odd numbered lines (0,

and 1 in **Fig. 3.9g**). This replication method is a simple yet effective fix because (1) the number of the replicated data points is less than 1 % of the total number of the data points per line (N_{HS}), and (2) the information given by the replicated data points is usually insignificant, or even negligible since the replicated data points are on the very left edge of the image, while most critical information and features are generally located in the center of the image. After filling the missing data points in the even numbered lines, the 1D to 2D conversion proceeds to the last stage of the 1D to 2D conversion, the image stretch correction.

The image stretch occurs due to the sinusoidal angular velocity pattern of the resonant scanning mirror. Assuming the resonant mirror is tilting back and forth between one angle -θ, and the other angle θ, the resonant mirror's angular velocity becomes zero at -θ instantly, then the resonant mirror resumes rotating. The resonant mirror accelerates its angular velocity following a cosine function. At angle 0 °, the resonant mirror's angular velocity reaches its maximum. Afterwards, the resonant mirror's angular velocity decreases again exactly following the cosine function. Therefore, the resonant mirror's angular velocity shows exactly a cosine function from -$\pi/2$ to $\pi/2$ in terms of phase (φ). Transforming the angular velocity into the angular position at a given phase, the resonant mirror's angular position shows a sine function. However, the high-speed digitizer acquires data at a fixed sampling rate. As a consequence, the image generated by the confocal microscope is stretched increasingly towards the edges of the image as shown in **Fig. 3.10a** and **Fig. 3.10b**.
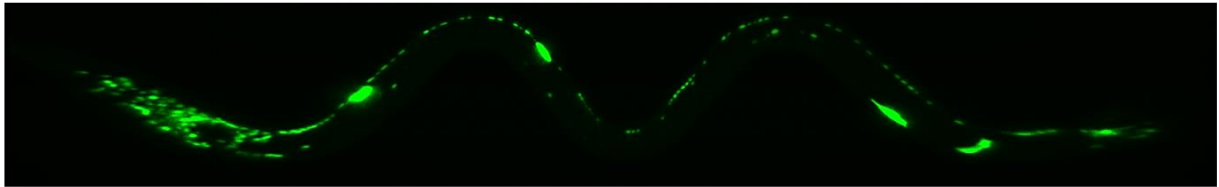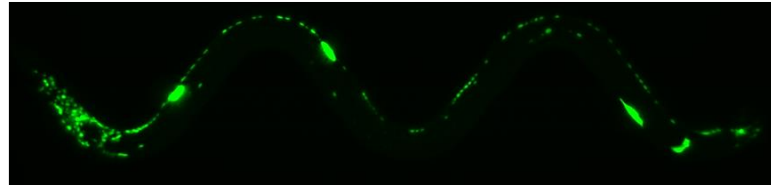
Figure 3.10: Image stretching due to resonant mirror and stretch correction. (a) The target sample. (b) The stretched image taken by resonant scanning. (c) An example of a stretched image. (d) The image corrected from the stretched image in (c).

A couple of hardware based approaches to circumvent the image stretching have been reported [84], [99]. However, the hardware based approaches tend to be difficult and complicated to design and build. On the contrary, the predictable behavior of the resonant mirror enables a software based correction using a pre-calculated look-up table. The look-up table provides information for data point relocation from the stretched images to the corrected images. The look-up table is calculated using a correction factor. The correction factor (C_{cf}) represents the degree of stretching to be corrected for a given data point.

Assuming that the number of data points per line before stretch correction is N_{HS}, the data point positions from $-N_{HS}/2$ to $N_{HS}/2$ corresponds to the phases from $-\pi/2$ to $\pi/2$ having set the center data point position to be 0. Then, the correction factor (C_{cf}) is given by

$$C_{cf} = \varphi/\sin\varphi \tag{3.19}$$

where φ is a phase at a given data point position. Eqn. (3.19) shows that the correction factor is not a constant, but a function of phase. Hence, each data point experiences a dissimilar degree of stretching. A through derivation of the correction factor and in-depth discussion of the image stretching by the resonant mirror is given in [94]. Using the correction factor, the image stretching by the resonant mirror's sinusoidal angular velocity is corrected by

$$\text{Corrected data point position} = \frac{\text{Stretched data point position}}{C_{cf}} \tag{3.20}$$

Once the look-up table is prepared, the look-up table needs not be updated as long as the number of data points per line before stretch correction (N_{HS}) remains constant regardless of the imaging field-of-view, because the sinusoidal angular velocity of the resonant mirror always maintains regardless of its tilting angle.

The 1D to 2D conversion first pads dummy data points to the very left end of each line before conducting the stretch correction (**Fig. 3.9h**). The addition of the dummy data points ensures that one line has the correct number of data points to correspond to the phase from $-\pi/2$ to $\pi/2$. Otherwise, the stretch correction ends up producing distorted images. After the dummy data padding, the 1D to 2D conversion corrects the stretch induced by the resonant mirror using the look-up table generated using the correction factor. Giving

an example, the parameters for the 1D to 2D conversion of our confocal microscope are $N_{HS} = 11008$, $N_S = 182 - 186$, and $N_{ZP} = 182 - 186$. After a successful 1D array to 2D image conversion, N_H ends up being 7292 for our confocal microscope. In the course of the 1D to 2D conversion, those N_S and N_{ZP}, approximately 370, data points are converted to less than 30 data points in the corrected image, which is less than 0.5 % of N_H. **Fig. 3.10c** and **Fig. 3.10d** are an example of before and after the stretch correction. The center of the image in **Fig. 3.10c** shows almost no stretching while the left and right edges of the image manifest significant image stretching. Additionally, the regions around the left and right edges of the images in both **Fig. 3.10c** and **Fig. 3.10d** contain no valuable information as discussed earlier.

3.3. RESULTS

3.3.1. Performance characterization

Having completed designing and building our high-speed laser scanning confocal microscope, we characterized its performance: the imaging resolution, the field-of-view (FOV), and the imaging speed. We used the 40X oil immersion objective (Nikon, 40×, 1.3 NA, oil, S Fluor) to calibration the imaging resolution by measuring the point-spread-function (PSF) of our confocal microscope. We recorded images of 0.1 μm diameter fluorescent microspheres (Invitrogen, F8803) inside the agarose pad, and chose 20 fluorescent microspheres from the images for PSF analysis. We measured and normalized the fluorescent intensity profiles of the fluorescent microspheres, and averaged the intensity profiles with the peak intensity aligned in the center. We acquired the lateral PSF of 275±11 nm FWHM, and the axial PSF of 1.16±0.14 μm FWHM (**Fig. 3.11a, b**). The measured

axial resolution is 30% larger than the expected axial resolution mainly due to the aberration induced by the refractive index mismatch between the oil medium and the agarose pad in the sample.

We characterized the imaging FOV of our confocal microscope. The imaging FOV depends on two variables: the sampling duration of the high-speed digitizer, and the magnification, thereof focal length, of the objective. First, we calibrated the relationship between the maximum FOV and the sampling duration with the 40X oil immersion objective (Nikon, 40X, 1.3NA, S Fluor). The resonant scanning mirror takes 63.2 μs to scan one line. Ideally, 63.2 μs should be set as the sampling duration. However, the sampling duration must be set shorter than 63.2 μs due to the data acquisition trigger delay, and the trigger electronics' rearming time of the high-speed digitizer. In addition, the resonant scanning mirror's sinusoidal angular velocity pattern allows a shorter sampling duration. At the end of the resonant mirror's one round tilting, the angular velocity of the resonant mirror becomes nearly zero. Hence, the image data from the last few μs of one round tilting may not need to be sampled. We measured the maximum FOV corresponding to the data sampling duration, and concluded that the maximum FOV began to level off after the data sampling duration of 59 μs, and any sampling duration over 60 μs gave the maximum FOV of 350 μm as shown in **Fig. 3.11c**. We have eventually chosen 60 μs as the data sampling duration because we have concluded that assigning a couple of microseconds for the high-speed digitizer to rearm its trigger electronics, and for the galvanometric mirror to tilt for the next line is substantially more beneficial than gaining a minutely larger FOV.
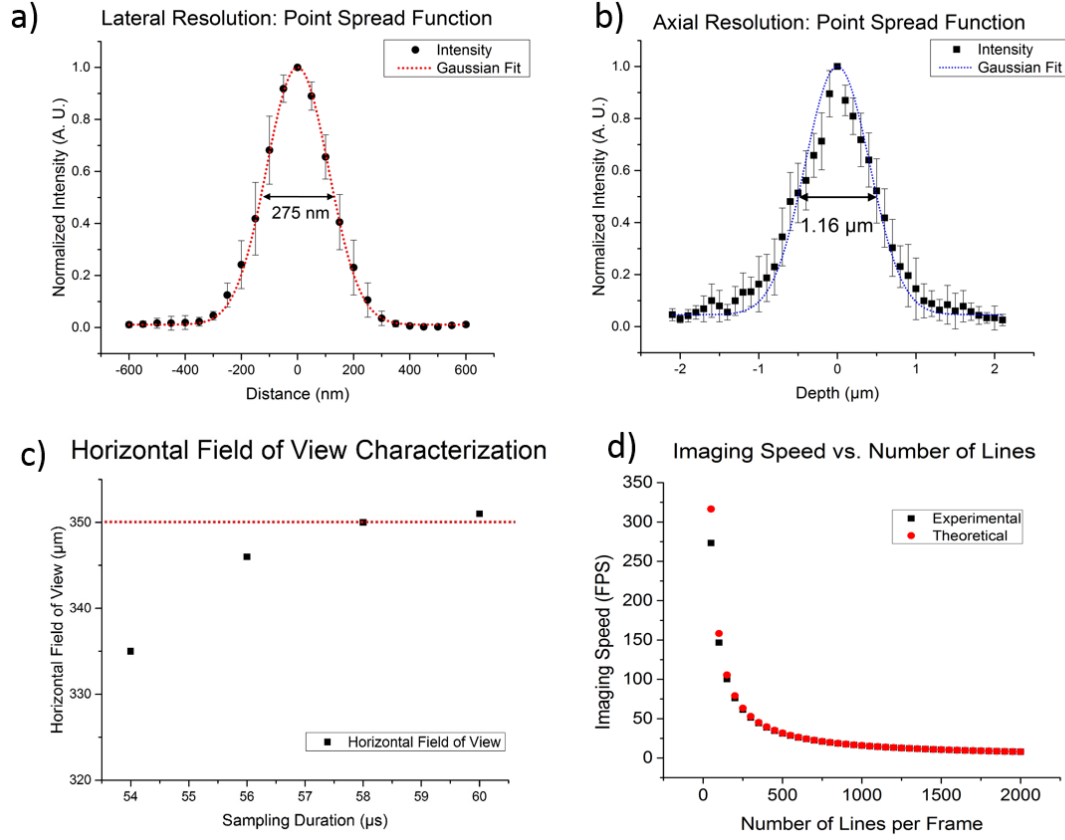
Figure 3.11: The performance measures of our confocal microscope. The performance parameters are measured with the 40x objective lens (Nikon, 1.3NA, Super Fluor). (a) The lateral resolution of 275±11 nm FWHM. (b) The axial resolution of 1.16±0.14 μm FWHM. (c) The horizontal field-of-view characterization. The field-of-view is 350 μm for 58 μs sampling duration, and levels. (d) The imaging speed characterization.

Secondly, we measured the maximum FOV of our confocal microscope, and its linearity with two objectives: 40× oil objective (Nikon, 40×, 1.3 NA, S Fluor), and 20× water immersion objective (Olympus, 20×, 0.95 NA, XLUPLFL20XWCG-SP). We set the tilting angle of the resonant mirror (fast x-axis) to be its maximum value, and the data sampling duration to be 60 μs. We moved the microfluidic device with the features of known dimensions using the pre-calibrated motorized XYZ stage. We find the maximum field-of-view is 350 μm, and 630 μm for 40× objective, and 20× objective respectively.

The measured field-of-views are approximately 10 % narrower than the expected field-of-views based on our design following the model described in **3.2.2**. Other studies using the same resonant mirror report that the maximum tilting angle of the resonant mirror is 14 °, which is roughly 10 % less than the maximum tilting angle given in the specification provided by the resonant mirror's manufacturer. Having considered the discrepancy between the actual and spec-sheet maximum tilting angles of the resonant mirror, the maximum FOV of out confocal microscope agrees well with our design.

Subsequently, we measured the field-of-view with the same objectives and the same method while increasing the tilting angle of the resonant mirror and the galvanometric mirror from 0 ° to 14 ° by 1 °. We verified that the FOV was linearly proportional to the tilting angle of the resonant mirror and the galvanometric mirror. Even though in theory the tilting angle and the field-of-view should show the sinusoidal relationship, the small tilting angle allows the sinusoidal relationship to be approximated as the linear relationship.

We evaluated the imaging speed of our confocal microscope. The time for our confocal microscope to image one frame is linearly proportional to the number of lines per frame (N_H in **3.2.5**). Thus, the imaging speed in frames per second (FPS) is inversely proportional to #line. The imaging speed of our confocal microscope follows $1/(63.2 \ \mu s \times N_H + 1 \ ms)$, where the 63.2 μs is the required time for the resonant mirror to scan one line, and the 1 ms inside the brackets is the fly-back time for the slow axis galvanometric mirror to return to its initial position at the beginning of each frame. We measured the imaging speed of our confocal microscope under these imaging conditions to verify the experimental imaging speed and the effect of the number of pixels per line on the imaging speed. We chose the number of lines per frame from 50 to 2000, and the number of pixels per line from 1000 to 10000. We embodied a timer inside our custom confocal imaging software written with LabVIEW to record the imaging time to take one frame. We find the

60

imaging speed is 59.5, 30.7, 20.7, and 15.6 FPS for 250, 500, 750, and 1000 lines per image respectively, which agrees with the expected speed based on our design (**Fig. 3.11d**). However, the imaging speed with a small number of lines per frame shows a noticeable discrepancy due to the fly-back time of the galvanometric mirror. Additionally, we find the number of pixels per line has no effect on the imaging speed since we observed the same imaging speed for all of the number of pixels per line we examined.

3.3.2. Sample images

We present a few sample high-resolution 3-dimensional (3D) volume images using our confocal microscope. The first sample 3D image we present is a high-resolution confocal fluorescent image of a L4-stage *C. elegans* head with the ZIM294 strain [44] shown in **Fig. 3.12**. Neither deconvolution nor any image filtering has been applied to the image. The ZIM294 strain is a nuclear localization signal green Ca^{2+} indicator (NLS-GCaMP) that Ca^{2+} fluorescent signal is confined inside the nuclei of the neuronal cells. This nuclear localization of the fluorescent signal enables more precise identification of individual neurons. The *C. elegans* head is densely packed with the neurons consisting of nearly 40 % of all of the *C. elegans* neurons. We mounted and anesthetized the animal on an agarose pad. We used the Nikon 40× 1.3 NA S Fluor oil immersion objective to take the images. The volume size of the image is $150 \times 50 \times 40$ μm^3 with $3000 \times 1000 \times 200$ voxels. We took 6 frames for each plane, and averaged the pixel intensity of the 6 frames to form a high-SNR image for the plane. The imaging of the whole volume took 80 seconds in total including the z-axis piezo stage moving time. The maximum intensity projection of the 3D rendered volume image is illustrated in **Fig. 3.12a**, and the maximum intensity projections in the XY, XZ, and YZ planes are given in **Fig. 3.12b, c, d**, respectively. In all of the

images, all neurons' nuclei are clearly resolved as well as the divisions among the nuclei are distinctly present.
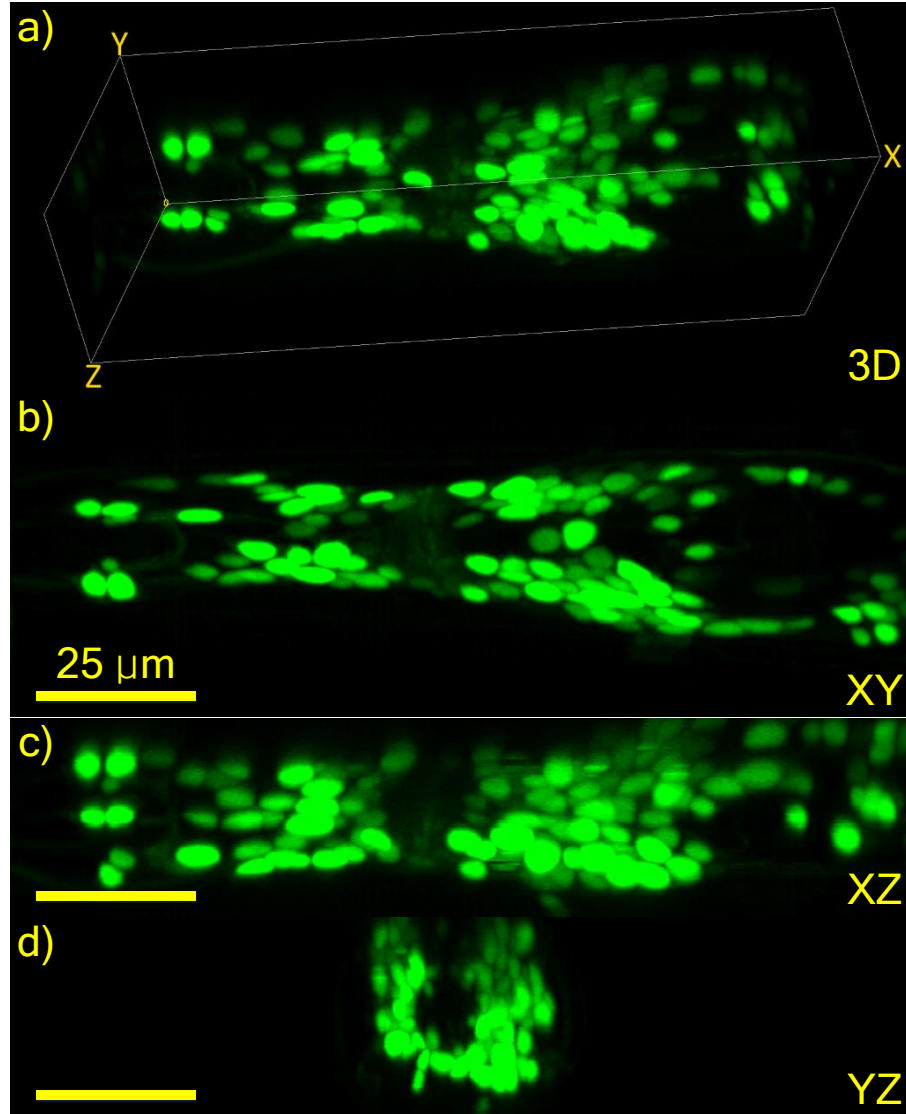
Figure 3.12: Maximum intensity projection of the head of *C. elegans* with ZIM294 Ex [Punc-31::NLSGCaMP5K; Punc-122::gfp] strain. The volume size is 150 μm × 50 μm × 40 μm, and the pixel number is 3000 × 1000 × 200. XY scale is reduced to match the z-axis pixel size (200 nm/pixel). (a) 3D maximum intensity projection, (b) XY plane maximum intensity projection, (c) XZ plane maximum intensity projection, and (d) YZ plane maximum intensity projection. The scale bar is 25 μm.

The second sample image is a z-axis maximum intensity projection image of the early L4 stage *C. elegans* whole animal as shown in **Fig. 3.13**. Neither deconvolution nor any image filtering has been applied to the image. The animal is labeled with the same ZIM294 strain used to label the animal shown in the previous sample image (**Fig. 3.12**). We took this image to examine how many neurons' nuclei the ZIM294 strain could label, and to assess how many ZIM294 labeled neurons' in the whole animal of L4 stage *C. elegans* we could recognize and mark. We placed, straightened, and chemically immobilized the animal on an agarose pad. We used the Nikon 40× 1.3 NA, S Fluor oil immersion objective to take the images. We separated the whole animal into three sections of a $350 \times 100 \times 50 \ \mu m^3$ FOV with $3500 \times 1000 \times 333$ voxels since the largest FOV the Nikon 40× objective can achieve in our confocal microscope is 350 μm while the length of the whole animal is over 700 μm. After taking images of three separate FOVs, we stitched the images of the three separate FOVs together to produce images of a $750 \times 100 \times 50 \ \mu m^3$ FOV containing the whole animal. As shown in **Fig. 3.13**, individual neurons' nuclei are effortlessly distinguishable even in the highly dense areas such as the head and tail regions. We managed to recognize and mark approximately 200 neurons' nuclei from the images.

The third sample image is a high-resolution 3D confocal fluorescent image of a L4-stage *C. elegans* ALM axons with the SK4005: *zdIs5* [*Pmec-4::gfp*] strain, which expresses GFP in the mechanosensory neurons [104] as shown in **Fig. 3.14**. Neither deconvolution nor any image filtering has been applied to the image. We recorded this image right after we performed a femtosecond laser surgery on the ALM axon of the animal. We mounted and anesthetized the animal on an agarose pad. We used the Nikon 40× 1.3 NA S Fluor oil immersion objective to take the images. The volume size of the image is $350 \times 50 \times 30$ μm^3 with $3500 \times 500 \times 150$ voxels. We took 6 frames for each plane, and averaged the

pixel intensity of the 6 frames to acquire a high-SNR images. The high-resolution high-SNR 3D confocal images clearly show the *C. elegans* ALM and anterior ventral microtubule (AVM) axons as well as the ALM axon wound severed by the femtosecond laser surgery.
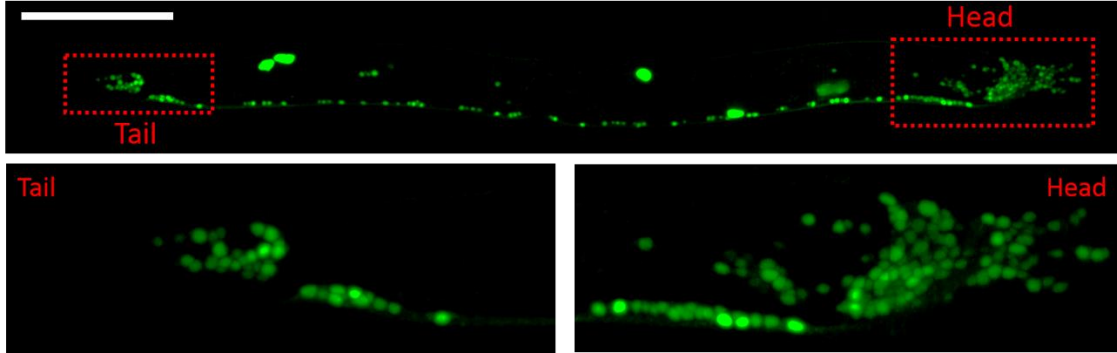
Figure 3.13: Z-axis maximum intensity projection of the whole animal of early L4 stage *C. elegans* with ZIM294 Ex *[Punc-31::NLSGCaMP5K; Punc-122::gfp]* strain. The image size is 750×100 μm², and the pixel number is 7500×1000. The scale bar is 100 μm. The head, and tail regions in the red dashed boxes are enlarged in the bottom half.

3.4. CONCLUSION AND DISCUSSION

We successfully designed, constructed, and characterized the high-speed laser scanning confocal microscope capable of imaging a large FOV with a great number of voxels. We have demonstrated our confocal microscope can image an area of 350×50 μm² (3500×500 pixels) at 30 Hz rate with a Nikon 40× objective. The hardware-software hybrid control and synchronization system of our confocal microscope achieves the fastest imaging speed that the resonant scanning mirror potentially can provides, and enables flexible control of imaging conditions.

The scanning system including the control and synchronization system of our confocal microscope can easily be employed by multi-photon microscopes. The scanning

system multi-photon microscopes use is optically identical, and the multi-photon microscopes' optical design for fluorescent photon collection is even simpler than that of confocal microscopes since multi-photon microscopes do not need to form a conjugate image plane and do not require a confocal pinhole. The major challenge in using our scanning system in multi-photon microscopes is the limited laser pulse repetition rate of ultrafast lasers. Mai Tai (Spectra Physics), a femtosecond laser which is widely used in two-photon microscopy achieves a pulse repetition rate of 80 MHz, one of the highest among commercially available ultrafast lasers. However, our scanning system requires a pulse repetition rate of at least 360 MHz to generate images of an acceptable SNR because multi-photon microscopy demands at least two pulses to generate a voxel, and our scanning system's data acquisition rate is 180 MHz. One feasible approach to increase the pulse repetition rate of ultrafast lasers is to use multiple beam splitters and mirrors, and recent studies have reported pulse repetition rate multiplication by a factor of 8 and 16 [105]–[107]. Thus, multi-photon microscopes potentially can employ our scanning system and achieve faster imaging speed and larger FOV combined with a high repetition rate ultrafast laser and the repetition rate multiplication using beam splitters.

The upcoming plan for our confocal microscope is to upgrade our confocal microscope to a multicolor system. Currently our confocal microscope can image only GFP specimens. Considering various available strains express yellow or red fluorescent proteins rather than GFP, a multicolor confocal microscope is undoubtedly more versatile. The high-speed digitizer our confocal microscope provides two input channels, hence is prepared for the multicolor system upgrade. However, the addition of one more data acquisition channel doubles the required data transfer rate between the computer memory and the storage device. The 500 MB/s data transfer rate of the current storage device cannot

meet the data transfer rate requirement. Thus, the multi-color upgrade necessitates a new storage device with superior performance.

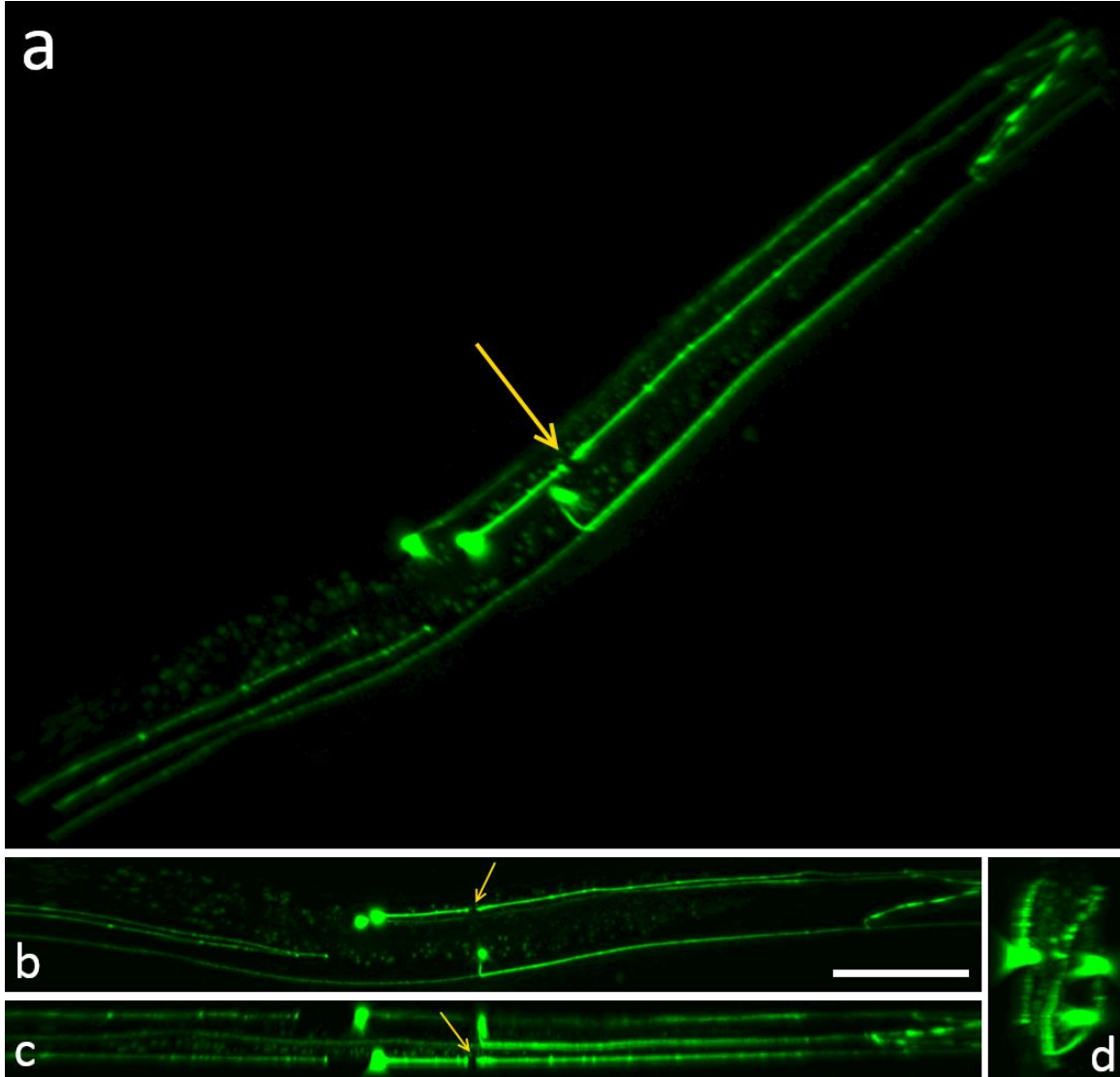**Figure 3.14:** High-resolution 3D image of L4 stage *C. elegans* encoded with *zdIs5 (mec-4::gfp)* after ALM axon femtosecond laser surgery. (a) 3D maximum intensity projection. (b) XY plane maximum intensity projection. (c) XZ maximum intensity projection. (d) YZ maximum intensity projection. The scale bar in (b) is 50 μm. The yellow arrows in (a), (b), and (c) depict the femtosecond laser surgery site.

Chapter 4: *in vivo* functional volumetric imaging of whole animal *C. elegans* Ca²⁺ dynamics

4.1. INTRODUCTION

The nematode *Caenorhabditis elegans* is an excellent model organism for a system level understanding of various aspects of neuroscience including neural circuits. *C. elegans* due to its stereotype cell lineage, well characterized genetics, short life cycle, and optically amenable body has been used intensively in biology. All of its neurons and synaptic connections are fully mapped anatomically using serial electron microscope sections [14]. Current day opto-genetic tools along with the tractable genetics allows researchers to trace individual neuronal cells in *C. elegans* under various context. These accomplishments are a great basis for future endeavors in functional characterization of neurons, and for unveiling of the wholesome picture of anatomical and functional map of all neurons in *C. elegans*. However, monitoring all *C. elegans* neurons simultaneously is challenging because *C. elegans* neurons are tiny, and most of them are concentrated in the head and the tail regions 1 mm apart. The small size of neurons, and high density in small volumes in the head and the tail require a submicron imaging resolution, and the 1 mm separation demands a large field-of-view to image the whole animal. In addition, a volumetric imaging speed faster than 1 Hz is necessary since the timescale of most *C. elegans* neurons' Ca²⁺ dynamics is maximum 1 Hz.

Various high-speed functional volumetric imaging methods have been recently reported. Light-sheet microscopy techniques with deconvolution processes were used to image the brain and the whole body of Zebrafish and Drosophila [52], [108]–[110]. The temporal focusing method and the spinning disk microscopy were used to observe the neuronal activities inside the brain of *C. elegans* [44], [111], [112]. The light-field imaging

and swept confocally-aligned planar excitation (SCAPE) microscopy were demonstrated their strength in whole animal imaging [43], [54]. A two-photon microscope using an ultrasound lens for fast axial scanning was reported [113]. A common issue among these methods is the obvious trade-off amongst the field-of-view (FOV), the resolution, and the speed. The methods with FOVs large enough to image whole animals show imaging resolutions over 1 μm full-width half-maximum (FWHM) while the methods with sub-micron resolutions image only a small fraction of animals due to their small FOVs. When multiple small FOVs are used to image the whole animal, the imaging speed dramatically decreases due to the required additional time for translational movement. No reported methods is capable of functional imaging of the whole L4 stage *C. elegans* to date.

We report a high-speed confocal volumetric imaging platform for monitoring Ca^{2+} response in the whole L4 stage *C. elegans* consisting of a high-speed laser resonant scanning confocal microscope, and a microfluidic device for animal immobilization and chemical stimulus delivery. Using this platform we successfully monitored the Ca^{2+} fluorescent signals of almost 70% of all 302 neurons inside the whole L4 stage *C. elegans*. The spatial imaging resolution of our method identifies individual neurons, and the temporal imaging resolution captures the Ca^{2+} dynamics of the neurons responding to chemical stimuli. Using NaCl stimulus in our stimulation chip, we found a number of neurons related to the animal's response to the stimulus from the whole nervous system calcium recordings. Our achievement demonstrates our high-speed volumetric imaging platform will contribute to whole animal mapping of *C. elegans* nervous system.

4.2. EXPERIMENTS

4.2.1. Overall setup

The *in vivo* functional volumetric imaging system consists of two major components: the high-speed laser scanning confocal microscope introduced in **Chapter 3**, and a microfluidic device for animal immobilization and stimulus delivery. We used an Olympus 20× 0.95 NA water immersion objective (Olympus, XLUPLFL20XWCG-SP) with the confocal microscope to achieve a large imaging FOV and a high imaging resolution simultaneously. We accomplished imaging a $630 \times 150 \times 25$ μm^3 volume (2100 $\times$ 500 $\times$ 15 voxels) at 2 Hz volume rate (30 Hz frame rate). We found the imaging resolutions to be 430 ± 25 nm FWHM laterally and 1.7 ± 0.2 μm FWHM axially, respectively having imaged 0.1 μm in diameter fluorescent beads (Invitrogen, F8803) as described in **3.3.1**.

4.2.2. Microfluidic device

We developed a microfluidic stimulation and imaging chip to enable high-resolution imaging of *C. elegans* neurons' calcium dynamics at high speed from the whole nervous system (**Fig. 4.1a**). An individual larval stage 4 (L4) stage *C. elegans* animal with bright GCaMP fluorescence is pushed through the worm inlet (W_{IN}) and immobilized inside the sinusoidally shaped trapping channel (**Fig. 4.1b**). The amplitude and width of the channel was optimized to fit in L4 stage *C. elegans* completely within the imaging FOV of 630×150 μm^2 (**Fig. 4.1c**). The head of the animal faces the stimulus delivery channel. The microfluidic chip has three stimulus inputs connected to two buffer reservoirs (B_{IN}) and one stimulus reservoir (S_{IN}) to deliver and withdraw chemical stimulus in less than 100 ms to and from the worm nose, respectively.
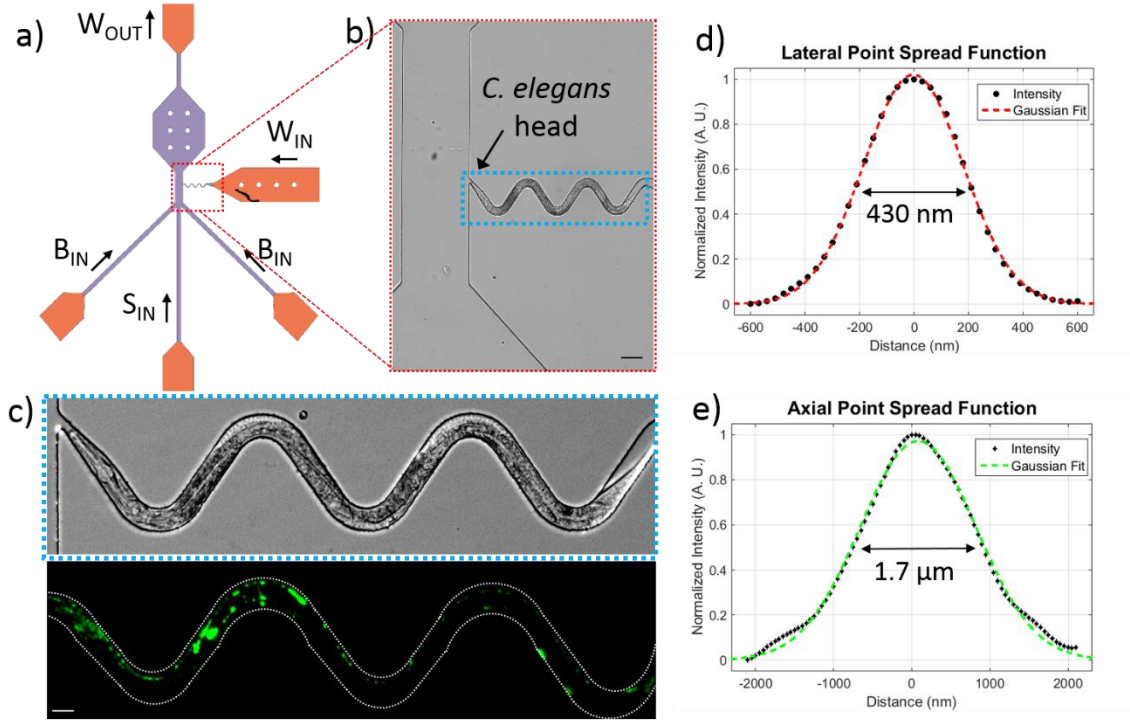
Figure 4.1: Microfluidic device for animal immobilization and controlled stimulation, and imaging resolution of the system. (a) The schematics of the microfluidic device for animal immobilization and stimulus application. (b) The enlarged view of the immobilization and stimulation area. (c) The whole animal fixing within the FOV of $630 \times 150 \ \mu m^2$. Top: brigh-field image. Bottom: z-axis maximum intensity projection of fluorescent confocal image. (d) 430 ± 25 nm FWHM of the confocal microscope's lateral imaging resolution. (e) $1.7 \pm 0.2 \ \mu m$ FWHM of the axial imaging resolution.

To reduce the effect of the pressure variance during the stimulus delivery, we ensure two of the three inlets are always turned on. The animal shows minimal amount of drift during the liquid switching under 2 psig liquid pressure. The tapered design of the channel prevents the animal from escaping and keeps the animal in the desired position during the time-lapse calcium imaging session.

The microfluidic devices were fabricated using standard multi-layer photo-lithography, and single-layer soft-lithography techniques [114], [115]. In brief, the photo

masks for photo-lithography were designed using AutoCAD (AUTODESK) and printed on transparencies using 50K DPI resolution laser-plotter (Fineline Imaging). A layer of SU8-2025 photoresist (Microchem Corp.) was spin coated on a 4 inch silicon wafer at 4,100 rotation per minute (rpm) for 33 seconds to obtain a height of 22 μm (Layer-1). The first layer was exposed to UV light using a photo-mask and developed using SU8 developer solution. Second layer of SU8-2025 was spin coated at 2,250 rpm for 33 seconds to obtain a height of 45 μm (Layer-2). The second layer was exposed to UV using a photo-mask and developed. The SU8 mold was treated with tridecafluoro-1,1,2,2-tetrahydrooctyl-1-trichlorosilane vapor (United Chemical Technologies) in a vacuum chamber at 40 ℃ to reduce surface adhesion during soft-lithography process.

To prepare the microfluidic device mold, Polydimethylsiloxane (PDMS, Dow Corning) was mixed in 10:1 ratio and poured on the salinized SU8 mold. The PDMS was cured at 70 ℃ for 2 hours, peeled off from the SU8 mold, and punched for access holes at four outlets. The PDMS block was cleaned and bonded to a cover glass (grade 1.5, 170 mm thickness) using 100 W oxygen plasma. The chip was finally cured at 70 ℃ for 6 hours to complete the bonding.

4.2.3. Experimental procedures

We first prepare a new PDMS microfluidic device. We connect metal couplers for liquid inputs to the microfluidic device, and fill the device with base buffer through one input while all exits are blocked with metal plugs for priming to remove air bubbles inside the device. We pick a L4 stage *C. elegans* with bright GFP signal in the coelomocyte cells under a stereoscope using a tube connected to a syringe. Once we capture an animal, we send the animal through the input ('W_{IN}' in **Fig. 4.1a**) of the device with the exit ('W_{OUT}' in **Fig. 4.1a**) open. We leave the animal free in the W_{IN} chamber with 45 μm height until

the animal's head goes first inside the trapping channel. Then, we push the animal inside the trapping channel with lateral orientation till the animal's head reaches the tapering region of the trapping channel.

Once the animal is trapped and prepared inside the microfluidic device, we mount the microfluidic device onto the confocal microscope and acquire high-resolution ten-frame-average images of the whole volume to help identify all the neurons in the animal's nervous system. The imaging condition we use for the high-resolution images is $4200 \times 1000 \times 100$ voxels for the same volume of $630 \times 150 \times 25$ μm^3. We stimulate the animal with the excitation laser for 2 minutes prior to the time-lapse calcium imaging to habituate the animal and to minimize the animal's neurons' response to the excitation laser during the time-lapse imaging.

The time-lapse volumetric imaging of *C. elegans* neurons' Ca^{2+} response is in total 4 minutes long, and comprises 3 phases. In the first phase, we image the animal only with the buffer flow but no stimulus for 2 minutes. We use the neurons' fluorescent intensity values in the first 2 minute phase to calculate the base level of the neuronal response. We use the base level to normalize the neurons' responses later in neuron response analysis. In the second phase, we expose the animal to the chemical stimulus for 30 seconds. In the third phase, we stop the chemical stimulation, and image the animal again only with buffer flow yet no stimulus for 1.5 minutes. After we complete the time-lapse volumetric imaging, we repeat the same stimulation experiment but with a wide-field microscope for a shorter time of 2 minutes: no stimulus for 30 seconds, stimulus for 30 seconds, and no stimulus for 1 minute. We use the wide-field microscope observation to quickly verify the animal's neuronal response, and the animal's physical integrity.

We grow and maintain *C. elegans* on nematode growth medium (NGM) agar plates with HB101 bacteria at 20 ℃ according to the standard protocol [116]. We use the

following *C. elegans* strains in this work: CX6632 Ex [*sra-6p::GCaMP*] and ZIM294 Ex [*Punc-31::NLSGCaMP5K; Punc-122::gfp*]. *C. elegans* strain CX6632 has GCaMP labelled in ASH neurons. ZIM294 has pan-neuronally expressed NLSGCaMP in all neuronal nuclei [44]. In both the strains neuronal cells can be visualized with green fluorescent proteins (GFP) under a fluorescence microscope.

All chemicals for *C. elegans* maintenance were bought from Fisher's Scientific and Sigma. Chemotaxis experiments were performed with chemotactic buffer (5 mM potassium phosphate, 1 mM $CaCl_2$, 1 mM $MgSO_4$, and 50 mM NaCl) as base value and +10 mM or +50 mM NaCl as a stimulus. For osmalirity experiments, we treated the animals with S. basal as base line and exposed them to 1M glycerol as stimulus.

4.3. RESULTS

4.3.1. Preliminary: feasibility of volumetric confocal imaging

The core goal is to monitor the Ca^{2+} response dynamics of all of the neurons inside the whole *C. elegans* animal. The size of neurons of *C. elegans* is as small as a few μm, and the distance between two neuron cells can be less than 1 μm, thus, a submicron imaging resolution is required to identify all of the neurons. The length of L4 stage *C. elegans* ranges from 800 μm to 900 μm, and the thickness is approximately between 40 μm and 50 μm. Hence, a quite large imaging FOV is necessary. Lastly, the timescale of the Ca^{2+} dynamics of *C. elegans* neurons is usually a few seconds, and one second at its fastest. Hence, the volumetric imaging speed has to be minimum 2 volumes per second (VPS) to sample the Ca^{2+} dynamics correctly while meeting the Nyquist condition.

We designed a volumetric imaging experiment to assess the feasibility of our laser scanning confocal microscope for high-speed functional volumetric imaging of *C. elegans* Ca^{2+} dynamics. We chose a 20X water immersion objective (Olympus, 20X, 0.95 NA, water, XLUPLFL20XWCG-SP) to achieve a large FOV and an imaging resolution high enough to identify individual neuronal cells. We obtained the maximum FOV of 630 μm horizontally. The measured the imaging resolution by imaging 0.1 μm fluorescent beads, and found the lateral resolution to be 430±25 nm FWHM, and the axial resolution to be 1.7±0.2 μm FWMH. We first set the FOV to be 630 x 70 μm^2, and the number of pixels to be 4200 x 500 to examine the imaging performance such as the image quality, and the imaging speed.

First, we imaged an anesthetized L4 stage *C. elegans* encoded with ZIM294 Ex [*Punc-31::NLSGCaMP5K; Punc-122::gfp*] strain [44]. ZIM294 strain labels all neurons in the animal, yet, restricts the fluorescence expression to the nuclei of the neuron cells. We imaged the animal at 15 different depths over the 30 μm thickness. At each depth, we first took a non-averaged image, then, took a 5-frame-averaged image. Subsequently, we compared the fluorescent intensity profiles of the two images of different averaging conditions at each plane. **Fig. 4.2** shows the maximum intensity projections of the two non-averaged and 5-frame-averaged images. Comparing the two images, they look almost visually identical to each other, especially in the ventral cord region where the neuron density is much lower than the head region. Since the *C. elegans* head region is densely packed with neurons, we investigated the neurons' fluorescent intensity in a few particularly dense areas quantitatively. We present two investigated image samples in **Fig. 4.2b, c**. Comparing the fluorescent intensity profile of the dashed yellow lines in the non-averaged image and the 5-frame-averaged images at both 8 μm and 16 μm depth, their intensity profiles agree very well. The noise level of the non-averaged images is slightly

higher than that of the 5-frame-averaged images, however, it is low enough not to interfere with the neuron identification. Thus, we conclude that the image quality of the non-averaged images are qualified for high-speed volumetric imaging.
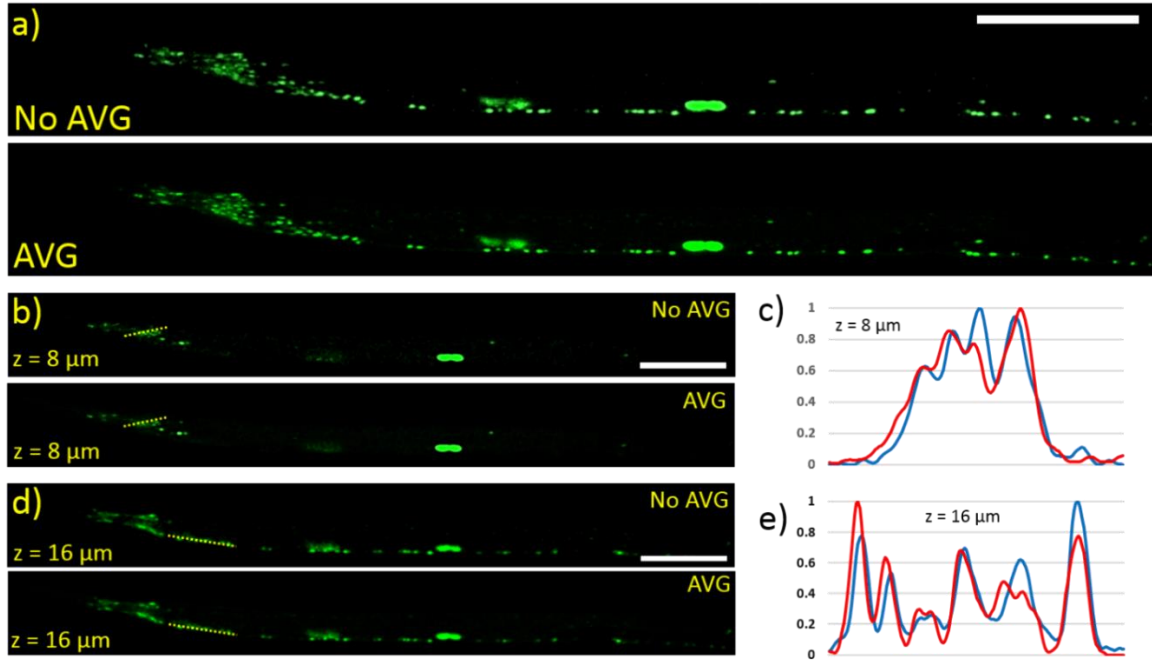
Figure 4.2: Comparison between non-averaged images and 5-frame-averaged images. (a) Maximum z-projection. (b) Selected images at 8 μm depth. (c) Fluorescence intensity plots of the dashed yellow lines in (b). (c) Selected images at 16 μm depth. (e) Fluorescence intensity plots of the dashed yellow lines in (b). In (c) and (e), the blue and red lines represent non-averaged and averaged images respectively. Scale bars are 100 μm in (a), (b), and (d).

Second, we measured the imaging speed. The imaging condition we set is the FOV of 630 x 70 μm², the pixel number of 4200 x 500, and the imaging depth of 30 μm with 15 steps of a 2 μm depth increment. With the 4200 x 500 pixels, our confocal microscope take images at 30 FPS speed. Since the 15 planes constitute one volume (**Fig. 4.3**), our confocal microscope can image 2 volumes per second (VPS) in theory. We performed volumetric

imaging in the aforementioned imaging condition for 2 minutes, and counted the number of images our confocal microscope took to verify the imaging speed. Our confocal microscope took 3500 images on average 100 images short of the expected number of images. This discrepancy stems from the imaging speed decrease by the piezo stage movement, approximately 1 ms between two planes. Considering the piezo stage movement time, the acquired volumetric imaging speed meets the theoretical prediction.

Figure 4.3: Preliminary volumetric images of *C. elegans*. The images represent consecutive planes of the whole animal volume at a 2 μm depth increment. The 0 μm in the middle image describes the center of the whole volume. The FOV is 630 x 70 μm^2

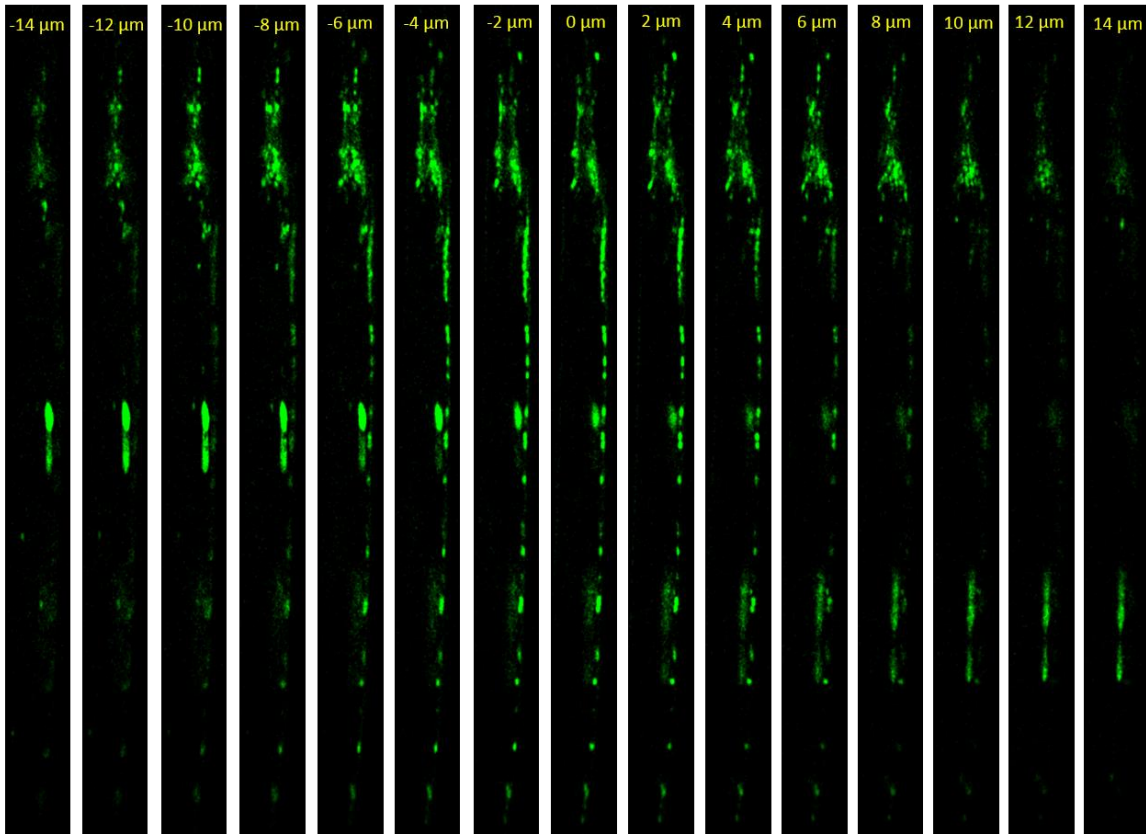We accomplished the imaging speed and the imaging resolution to enable the high-speed volumetric imaging of *C. elegans* Ca^{2+} response dynamics. However, the imaging

FOV covers only 3/4 of the whole L4 stage animal. In the previous imaging experiment, the pixel size we used was 150 nm/pixel. Considering the lateral imaging resolution of our confocal microscope with the 20× objective, we can increase the pixel size up to 300 nm/pixel without sacrificing the imaging resolution severely. With the pixel size of 300 nm/pixel, the imaging resolution will degrade to 600 nm FWHM from 430 nm FWHM, nonetheless, 600 nm FWHM is capable of identifying individual neurons. By increasing the pixel size to 300 nm/pixel, we enlarge the FOV to 630 x 150 μm^2 while keeping the number of lines per frame still at 500 and the imaging speed the same at 2 VPS. The increase in the vertical FOV enables fitting the whole animal inside the FOV by bending the animal. To efficiently bend, fit, and immobilize the whole animal within the FOV, we have developed the microfluidic device shown in **Fig. 4.1a**. Once the microfluidic device has been developed, we record whole animal functional volumetric images of all of the *C. elegans* neurons responding to a chemical stimulus (+10 mM NaCl). Then, we analyze the neurons' fluorescent intensity variation over time, and study the neuronal response to the chemical stimulus.

4.3.2. *C. elegans* neurons' response to +10 mM NaCl

We here present selected L4 *C. elegans* neurons' response to +10 mM NaCl from an *in vivo* functional time-lapse volumetric imaging session. After completing the time-lapse imaging session, we first organized the acquired images plane by plane. The imaging session generated total 7084 images. Since the whole volume consists of 15 planes, each plane was given 472 images for 4 minutes. Then, we inspected the time-lapse images of each plane manually. During the inspection, we selected 18 neurons (1–18 in **Fig. 4.4a**) that showed noticeable brightness change, and 6 neurons (n1–n6 in **Fig. 4.4a**) that showed little brightness difference between before and after 120 second mark when + 10 mM NaCl

77

was applied to the animal. After selecting the neurons we used a MATLAB script to analyze the neurons' fluorescent signal intensity because the neurons shifted about due to the animal's movement throughout the imaging session.
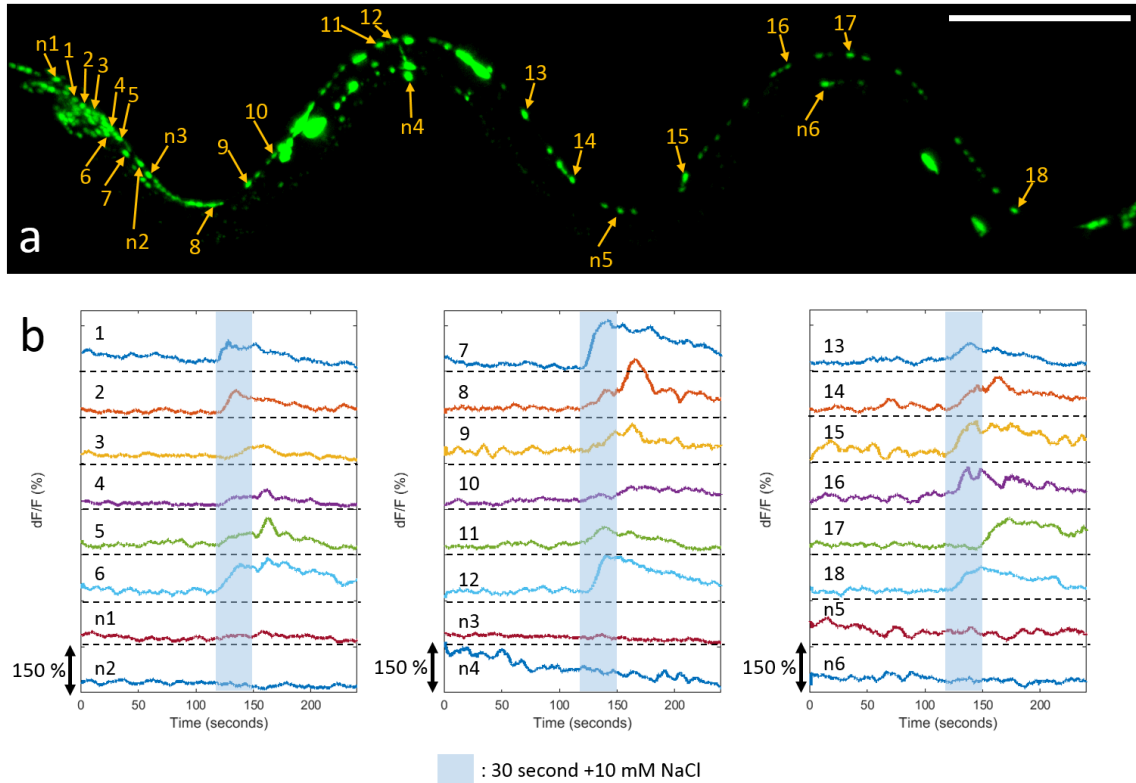
Figure 4.4: Selected L4 stage *C. elegans* neurons' response to +10 mM NaCl. (a) z-axis maximum intensity projection of the whole animal immobilized inside the trapping microfluidic device. Total 24 selected neurons. 18 responsive neurons (1−18), and 6 irresponsive neurons (n1−n6). Scale bar 100 μm. (b) Neuronal response plots for 24 neurons. Total 240 seconds. +10 mM NaCl application at 120 second mark for 30 seconds in the grey-blue box. The black arrow scales 150 % relative change.

The MATLAB script first loaded the 472 images of a plane, and defined a region surrounding one of the neurons we selected on the plane. The MATLAB script detected the highest intensity pixel within the defined region in the first image of the plane. Then,

the MATLAB script averaged the intensity values of the highest intensity pixel and the 8 pixels surrounding the highest intensity pixel. The MATLAB script repeated this process for all 472 images, and recorded the averaged intensity values over the 472 images. Subsequently, the MATLAB script found the minimum value among the 472 averaged values, and normalized the 472 averaged values by the minimum value. The MATLAB script repeated the whole process for all 24 neurons shown in **Fig 4.4a**, and the processed and normalized neuron intensity profiles by the MATLAB script are given in **Fig 4.4b**.

The neurons in **Fig 4.4a** are numbered increasingly from the head to the tail. Neurons 1–7, and n1–n3 are in the head, and the rest are located along the ventral cord. Neurons 1–18 seem to have responded to +10 mM NaCl while neuron n1–n6 do not (**Fig 4.4b**). Neurons 1–5 in the head show moderate response. On the contrary, neuron 6, and 7 in the head show significant response. Neurons 12, 15, and 18 along the ventral cord also show substantial response to +10 mM NaCl. Interestingly, several neurons (4, 5, 6, 8, 9, 10, 14, and 17) noticeably reacted to the cease of +10 mM NaCl at 150 second point. Neurons n1, and n2 show no response to the stimulus though they are located in the vicinity of responsive neurons (1, and 7). Neurons n1–n3 seem constantly inactive throughout the experiment while neurons n4–n6 show a fair amount of activity though irresponsive to +10 mM NaCl.

4.3.3. *C. elegans* **neurons' activity with no stimulus**

We present behavior of 176 neurons in the whole L4 stage *C. elegans* animal with no stimulus application. We conducted an *in vivo* time-lapse volumetric imaging experiment on a L4 stage *C. elegans* immobilized inside the microfluidic device, and we replaced the +10 mM NaCl with the buffer. Unlike the previous +10 mM NaCl experiment,

we exposed the animal to the buffer at 120 second mark. The duration of the experiment was still 4 minutes.
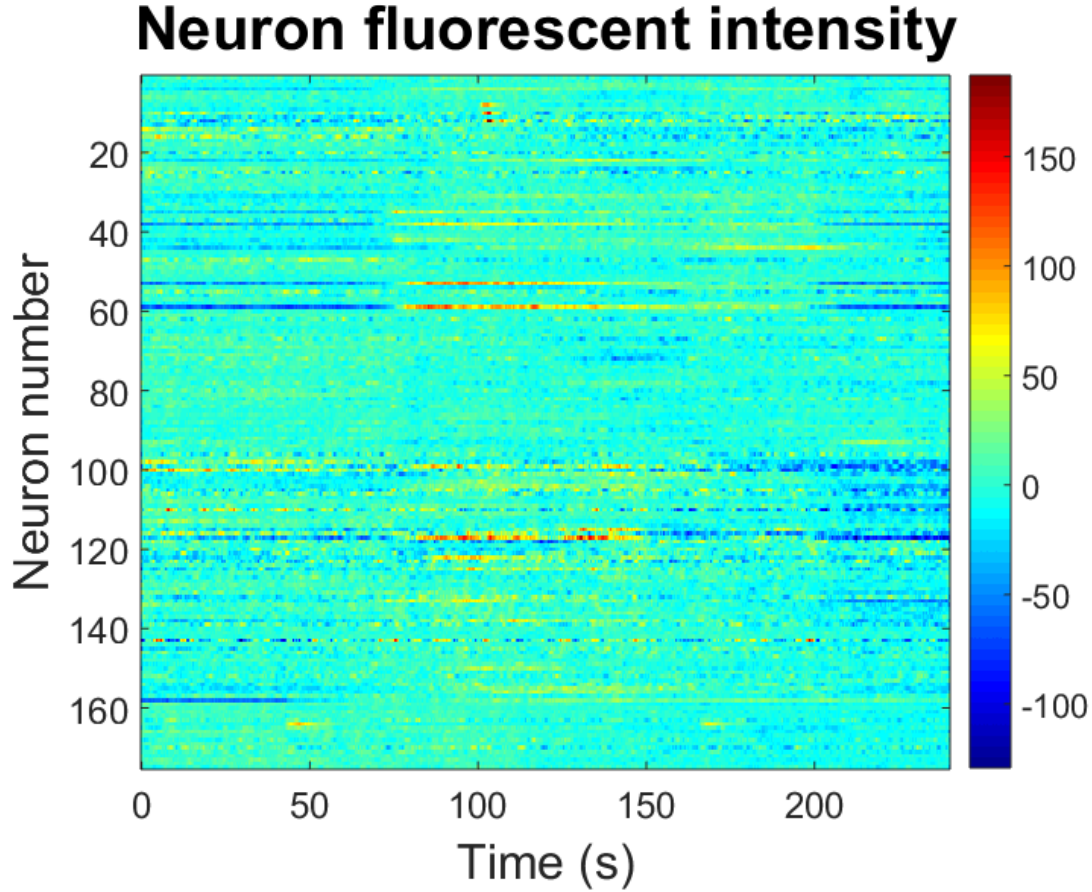
Figure 4.5: Heatmap presentation of 176 neurons' Ca^{2+} dynamics in the whole L4 stage *C.elegans* with no stimulus application. Total 176 neurons. 1–75 in the head region, 76–160 along the body, and 161–176 in the tail region. The neuron activity observation was 240 seconds long. The red-to-blue colored bar scales the relative fluorescent intensity change from -125 % (blue) to 175 % (red).

After completing the *in vivo* time-lapse imaging experiment, we thoroughly analyzed the acquired images. First, we corrected the neurons shifts over time due to the animal's movement using the motion correction algorithms provided by [117]–[119]. The

motion correction played a crucial role in neuron annotation and intensity tracing. The motion correction provided enhanced time-lapse images with higher SNR by reducing the blurring from neurons' motions. The motion correction also affixed the positions of the corrected neurons so that the neuron intensity tracing could be carried out simply by tracking the pixel intensity in the same position and area over time.
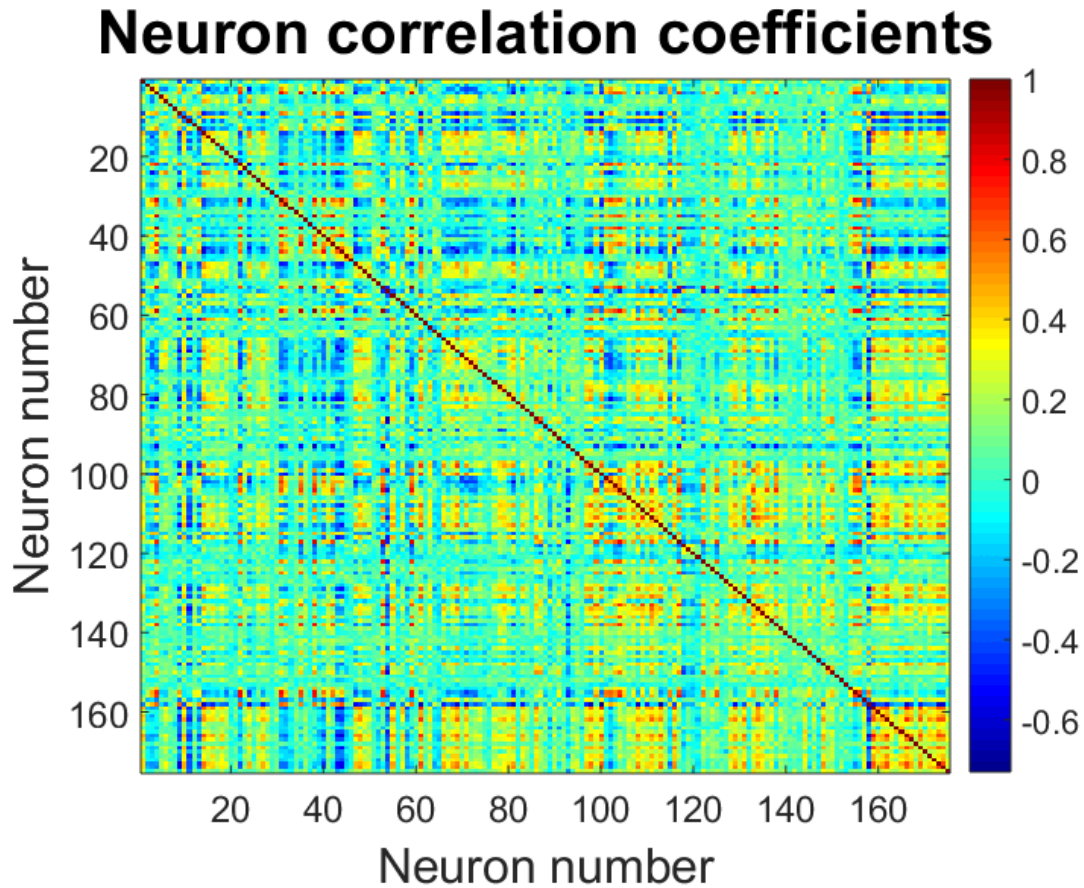

Figure 4.6: Heatmap presentation of correlation coefficients among 176 neurons in L4 stage *C. elegans* with no stimulus application. Total 176 neurons. 1–75 in the head region, 76–160 along the body, and 161–176 in the tail region. The correlation coefficients range from -0.7 (blue) to 1 (red) as shown in the color bar.

Having finished the motion correction of neurons, we scrutinized the time-lapse images, and tried to label as many neuron as we could. We ended up finding 176 neurons in the whole L4 stage *C. elegans*. 176 neurons are approximately 60 % of all neurons in *C. elegans*. After the neuron labeling, we recorded the fluorescent intensity progression of all 176 neurons over time (**Fig. 4.5**). Neurons 1–75 were found in the head region, 76–160 along the body, and 161–176 in the tail region. The fluorescent intensity plot of the 176 neurons clearly illustrates neurons' activities. At around 80 second mark, a number of neurons in the head and along the ventral cord activated, and stayed 'on' for almost 1 minute. At 100 second mark, a few neurons in the head triggered on for a few seconds. We calculated correlation coefficients among neurons' activities (**Fig. 4.6**). The correlation coefficients suggest that a number of neurons in the tail are highly correlated while quite a few neurons in the tail are anti-correlated. The correlation coefficients among the head neurons also suggest that a substantial number of head neurons are correlated and anti-correlated to one another. Additionally, the neurons along the ventral cord are deemed linked to the head and tail neurons to an extent, however, more extensive in-depth studies are necessary to reach credible conclusions.

4.4. CONCLUSION AND DISCUSSION

We successfully demonstrated high-speed confocal functional volumetric imaging of all neurons' activities in the whole L4 stage *C. elegans* at submicron single cell resolution. Previously announced high-speed volumetric imaging methods for *C. elegans* were capable of either high resolution or imaging the whole worm, however, never both. The methods capable of high resolution imaging had a limited FOV suitable for a small part of the animal, while the methods capable of imaging the whole animal had a low imaging resolution incapable of identifying individual neurons in the brain of *C. elegans*

82

where neurons are densely populated. Our imaging method is the first to achieve functional volumetric imaging of the whole L4 stage *C. elegans* at the submicron resolution.

We showed our functional volumetric imaging platform combined with the microfluidic device is feasible for *in vivo* study of chemosensory neurons in whole L4 *C. elegans*. Our platform is highly suitable for applying any liquid chemical stimulus to the animal while observing the response of its all neurons. This significant strength of our platform enables chemosensory experiments on L4 stage *C. elegans* which were impossible. In addition, the imaging principle of our platform is based on the mature confocal microscopy technique. Hence, the adoption of our method is expected to be an easy task.

Despite the aforementioned strengths, our functional volumetric imaging platform also implies clear challenges. Our platform needs powerful and reliable motion correction software. Though the microfluidic device indeed suppresses the animal's movement, the animal still slides along the trapping channel especially at the very moment when the animal senses the stimulus. Completely eliminating a living creature's movement is practically impossible. Our imaging platform undersamples the target volume along the z-axis. Currently, the z-step size for the *in vivo* volumetric imaging is 1.67 μm. Considering the size of *C. elegans* neurons' nuclei is around $2 - 3$ μm in diameter, the z-step size should be 1 μm or less. In addition, our volumetric imaging platform is severely susceptible to shot noise. Out imaging platform is built on the point scanning microscopy, and the exposure time per pixel is extremely short due to its fast scanning speed. As a result, the number of photons the detector collects is exceedingly low, thus the SNR of the images is also poor [120]–[122].

A novel high-speed volumetric imaging method using a multipoint optical detector may address the challenges discussed in the previous paragraph. A multipoint optical

83

detector collects photons through multiple channels in parallel, thus, can extend the exposure time per pixel extensively for the same number of pixels. The extension of the exposure time leads to collection of a larger number of photons, consequently improves the SNR of the images. For example, a line scanning camera of 4,096 pixels can use an exposure time 4,000 times as long as a single point detector can to acquire 4,096 pixels. As a result, the 4,096 pixel image generated by the line scanning camera will show a SNR 60 times as high as the 4,096 pixel image by the single point detector.

A line scanning confocal microscope is a novel imaging method capable of optical sectioning at great imaging speed using a line scanning camera. A line scanning confocal microscope (LSM510, Zeiss) could acquire 512×512 pixel images at 120 Hz rate using a CCD line scanning camera in 2006 [123]. For the last 10 years, camera and sensor technologies have been rapidly developing, cameras' imaging speed and sensitivity have been improving significantly, and state-of-the-art line scanning cameras in 2016 can obtain 4,096 pixel lines at 200 kHz rate. Theoretically speaking, a line scanning confocal microscope using the 4,096 pixels/line at 200 kHz camera will be able to produce $4,096 \times 512$ pixel images at 400 Hz rate while providing a SNR superior to that by a point scanning confocal microscope of the same performance. Additionally, the imaging resolution achieved by a line scanning confocal microscope is only about 20 % inferior to a point scanning confocal microscope. Considering all of the strengths, the line scanning confocal microscope will address the z-axis undersampling issue, and the poor SNR issue of using the point scanning confocal microscope for functional volumetric imaging while achieving a higher volumetric imaging rate.

Chapter 5: High-throughput automated imaging platform for *C. elegans* nerve regeneration study

5.1. INTRODUCTION

We built a high-throughput automated confocal imaging platform to rapidly record high-resolution 3D images of regenerated axons in multiple *C. elegans* after laser axotomy. We used the high-speed laser scanning confocal microscope in **Chapter 3** as the confocal imaging system. To accomplish high-throughput automation combined with the confocal microscope, we developed a microfluidic device to load and immobilize multiple animals in parallel, an image processing algorithm to precisely detect the locations of the immobilized animals, and a software program to generate an automated imaging sequence based on the locations determined by the algorithm.

The microfluidic device immobilizes and aligns 20 animals in certain orientations in which the regenerated axons of interest are efficiently imaged *in vivo*. The animal detection algorithm correctly finds animals' locations with a success rate over 90%. The sequence generation software controls our confocal microscope and the motorized stage to minimize the automated imaging time. Our automated imaging platform successfully achieves taking high-resolution 3D images of 20 regenerated *C. elegans* axons in 10 minutes before the immobilized animals suffer excessive physical stress then release autofluorescent signals which deteriorate the signal-to-noise ratio of images. The FOV of the 3D images is $350 \times 50 \times 30$ μm^3 with $3500 \times 500 \times 150$ pixels, and the imaging resolution is 275 ± 11 nm FWHM laterally, and 1.16 ± 0.14 μm FWHM axially, which is capable of resolving the 300 nm thickness of *C. elegans* axons laterally.

5.2. EXPERIMENTS

5.2.1. Overall setup

We built a high-throughput automated confocal imaging platform based upon our high-speed confocal microscope for visual inspection of *C. elegans* axon regrowth and recovery after ultrafast laser axotomy. The imaging target is the axons attached to the anterior lateral microtubule (ALM) cells shown in the red boxes in **Fig. 5.1a, b**. The thickness of the axons is known to be approximately 300 nm, and the laser surgery cut size is 1–2 μm, hence, a very high imaging resolution is essential to properly capture the fine features of the axons. We usually perform the ultrafast laser axon surgery 30 μm away from the ALM cells. In addition, the regrown axon after the laser surgery could extend longer than 50 μm. Thus, an imaging FOV wider than 150 μm horizontally is required to image the surgery area and the regrown axons adequately. We used the 40× Nikon 1.3 NA S Fluor oil immersion objective to meet the imaging resolution by achieving the 300 nm FWHM and 1.16 μm FWHM lateral and axial resolutions. We set the imaging FOV to be $350 \times 50 \times 30$ μm^3 ($3500 \times 500 \times 150$ pixels) shown in **Fig. 5.1c** to comply with the imaging FOV requirements. The C. elegans animals used in this study are encoded with the transgenic line *zdIs5* (*mec-4::GFP*). The transgenic *C. elegans* animals express GFP in six touch receptor neurons including their cell bodies and axons.

5.2.2. Multi-trapping microfluidic device

To successfully accomplish the automated confocal imaging of multiple animals, we added the microfluidic device for parallel immobilization of multiple animals, and modified the confocal microscope software for automation. We designed and fabricated the microfluidic device that plays a very important role in automation shown in **Fig. 5.1d**.

The microfluidic device immobilizes multiple animals *in vivo* in the straight trapping channels without using anesthetics. The trapping channels immobilize the animals in specific orientations that allow more efficient imaging of the ALM region. The predetermined distance between two consecutive trapping channels enables automated sample movement. The straight shape of the trapping channels helps the efficient use of the rectangular FOV, hence, increases the overall automated imaging process.
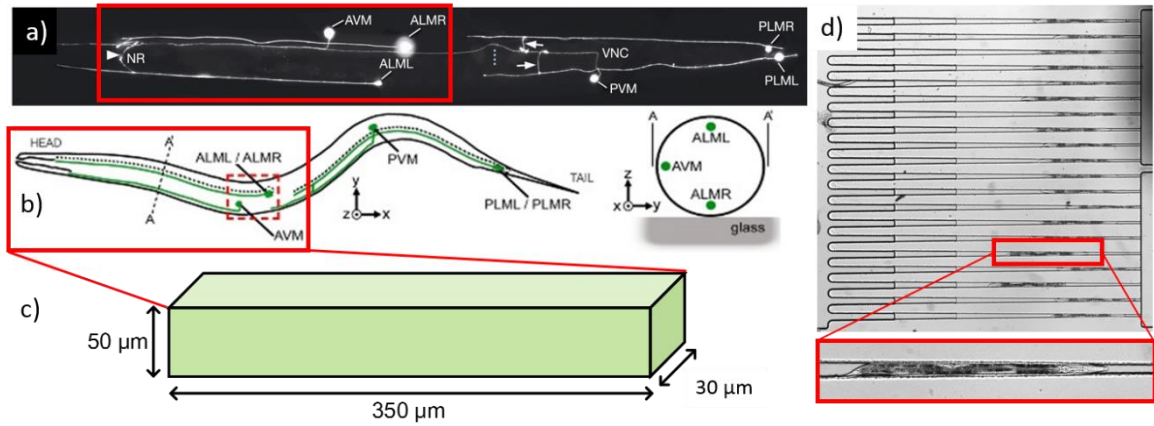
Figure 5.1: High-throughput automated confocal imaging platform. (a), (b) The imaging target is the ALM cell and its axon in the red box. The animal is labeled with the transgenic line *zdIs5* (*mec-4::gfp*) (c) The imaging volume size = $350 \times 50 \times 30$ μm^3 ($3500 \times 500 \times 150$ pixels). The imaging speed is 30 FPS. (d) Microfluidic device for *in vivo* anesthetics-free immobilization in desirable orientations.

5.2.3. Automation flow

The work flow of the high-throughput automated confocal imaging is illustrated in **Fig. 5.2**. First, we mount the microfluidic device where L4 stage *C. elegans* animals are loaded on the motorized XYZ stage, and align the orientation of the microfluidic device to minimize the slant of the trapping channels in the field-of-view. Then, we immobilize the worms inside the trapping channels of the microfluidic device by applying a pressure of

87

approximately 65 kPa, and take a fluorescence image of all of the worms immobilized inside the microfluidic device channels with a low magnification objective (Nikon, 4X, dry), and a large sensor camera (Thorlabs, 8050M-GE-TE). We send the fluorescence image to our custom software for imaging target location analysis.
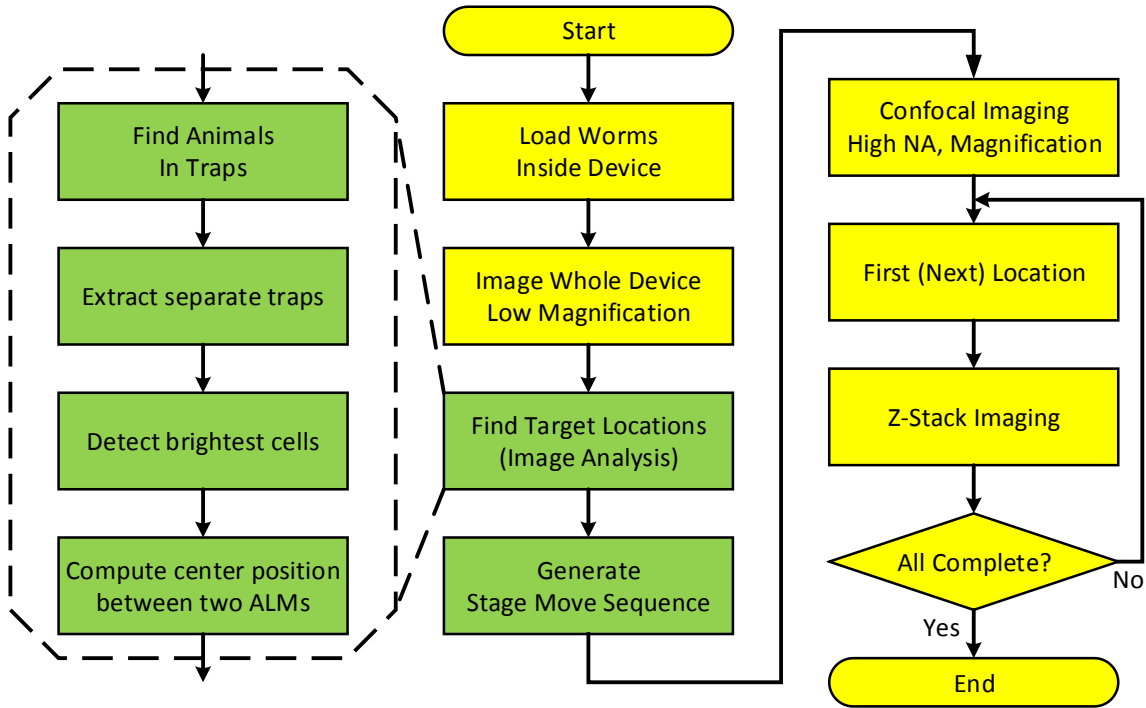
Figure 5.2: Flow chart of the automated confocal imaging process. The green boxes specifically describe the ALM detection algorithm.

The analysis software first applies a smooth filter to the fluorescence image, then, find the highest intensity pixel in each line from the top to the bottom of the fluorescence image, and creates an intensity profile (**Fig. 5.3c**). In the intensity profile, the analysis software finds locations of intensity peaks which depicts the locations of the trapped worms and the trapping channels. While finding the intensity peaks, the analysis software ignores peaks showing low intensity values since intensity values below 30% of the average peak

88

intensity is translated as unhealthy worms which are not worthy of investigation. Based on the intensity peak locations, the analysis software segments the fluorescence image into individual trap images for ALM location analysis.

In each segmented trap image, the analysis software detects the locations of 3 highest intensity peaks which correspond to two ALM cells and two posterior lateral microtubule (PLM) cells (**Fig. 5.3c**). The two PLM cells appear to be one peak because they are very close to each other. The analysis software computes the distances between intensity peaks, and compare the three distances. The analysis software calculates the center location of the two locations with the smallest distance because the smallest distance is the distance between two ALMs. The analysis software repeats calculating the ALM locations for all the segmented trap images. Up to this point, all of the calculated distances are expressed in terms of pixels in the image. However, the pixel size has been already calibrated to the moving distance of the motorized XYZ stage. Thus, based on the calibrated pixel size information, the analysis software generates a sequence of translational moving distances from one ALM location to the next for the motorized xyz stage (**Fig. 5.3b**).

Once the moving sequence for the motorized XYZ stage is ready, we begin the automated confocal imaging session. We first install the 40× microscope objective (Nikon, 40X, 1.3NA, oil immersion, S Fluor) replacing the 4× objective, then, run the automated confocal imaging software. The automated confocal imaging software moves the motorized stage to the ALM positions following the moving sequence given by the analysis software, and takes z-stack images ($350 \times 50 \times 30$ μm^3, $3500 \times 500 \times 150$ pixels) of the ALM axons. Lastly, the automated confocal imaging software completes the automated imaging session after the automated confocal imaging software images the last ALM axon.
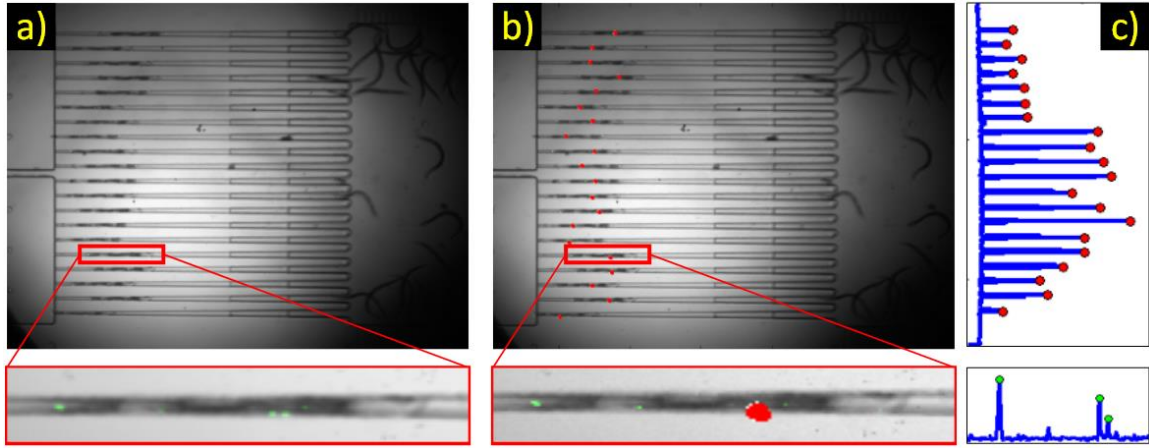
Figure 5.3: Automated detection of ALM locations. (a) Animals trapped inside the device. The green is the fluorescent signal from the animals. The red inlet shows the magnified view of the trapped animal. The two green dots are the ALM cells. (b) The locations of ALM cells depicted by the red dots. The red inlet shows the magnified view of the trapped animal with the red location marker. (c) Maximum intensity profile along the y-axis. The red dots are peaks detected by the analysis software. The small bottom box shows the intensity profile of one animal. The green dots are the three highest peaks.

5.3. RESULTS

5.3.1. Automated imaging performance

The automated confocal imaging session takes 10 minutes in total. We measured the automated imaging session by implementing a timer in the automated imaging software. Imaging one z-stack of an ALM axon takes 29 seconds. We take 6 frames for each plane for averaging, and the piezo stage movement for each step takes 2 ms, hence, 29 seconds are required for imaging the ALM axon of one animal. Moving from one ALM location to the next ALM location takes 1 second. Thus, the whole automated confocal imaging session for 20 worms takes 10 minutes (29 seconds/worm × 20 worms + 20 moves

× 1 second/move = 600 seconds = 10 minutes). Hence, the actual imaging time agrees well with the expected imaging time.

5.3.2. Sample images of axon regrowth and reconnection

We present two sample images of the ALM axons, a reconnected axon in **Fig. 5.4**, and a non-reconnected axon in **Fig. 5.5**. The two largest images on the top are the z-axis maximum intensity projection of two z-stack image sets, and have the 350 μm × 50 μm FOV. The ALM axons are aligned perfectly straight thanks to the straight trapping channels. The unique design of the trapping channels also aligns the *C. elegans* orientation for the ALM axons to locate close to the walls of the trapping channel. The small red rectangles depict the ALM axon femtosecond laser surgery sites, and the magnified images of the surgery sites at different depths are shown in the large red rectangles. The maximum intensity projection image of the reconnected ALM axon in **Fig. 5.4** shows significant amount of autofluorescent light around the femtosecond laser surgery site. The autofluorescence stems from the stress that the animal experience from the physical pressure for immobilization. If this animal had been imaged with a wide-field microscope, the overwhelming autofluorescent light might have extensively interfered with the inspection of the regrown axon. Looking at the depth-resolved images in **Fig. 5.4**, the ALM axon seems disconnected at depth z = 0 nm. However, the depth-resolved images at depth z = 800 nm and 1000 nm, the ALM axon shows profound reconnection. The successful reconnection is also supported by the fact that the ALM axon did not regrow extensively.
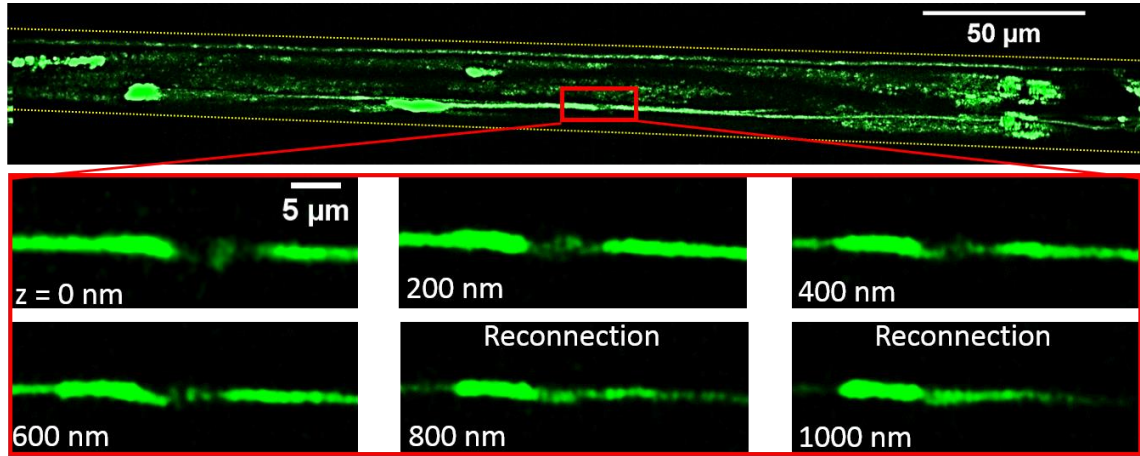
Figure 5.4: High-resolution confocal images of the reconnected ALM axon. The top image is the maximum intensity projection of the whole z-stack. The yellow dotted lines represent the trapping channel walls. The red box depicts the femtosecond laser axon surgery site. The enlarged images of the surgery site is given inside the bottom red box. The axon reconnection is clearly shown in the images at z = 800 nm and 1000 nm planes.

A regrown ALM axon without reconnection is illustrated in **Fig. 5.5**. First examining the maximum intensity projection image on the top, the autofluorescent light is even more pronounced than the reconnected axon image in **Fig. 5.4**. The intensity of autofluorescent light seems high enough to overwhelm the fluorescent light from the regrown axon if the regrown axon is inspected through wide-field microscopy images. Looking at the enlarged and depth-resolved images, the regrown axon from the right distal end of the original axon bends upwards ending up not reconnecting to the left distal end of the original axon as shown in the images at z = 600 nm, and 800 nm.

5.4. CONCLUSION

We developed the high-throughput automated confocal imaging platform for *C. elegans* nerve regeneration study. The automated imaging platform takes high-resolution 3D images of a $350 \times 50 \times 30$ µm^3 volume in 29 seconds, and completes imaging a batch of 20 animals in 10 minutes. The microfluidic device of the automated imaging platform

enables automation because the microfluidic device effectively immobilizes animals in specific orientations appropriate for *C. elegans* ALM axon imaging, and aligns the animals at a regular spacing. The analysis software of the automated imaging system successfully detects ALM axons and their locations, and generate a specimen moving sequence for the automated imaging. The high-resolution confocal images are capable of differentiate between ALM axon reconnection and regrowth with no reconnection even when the autofluorescent signal from the animal's body is substantial.
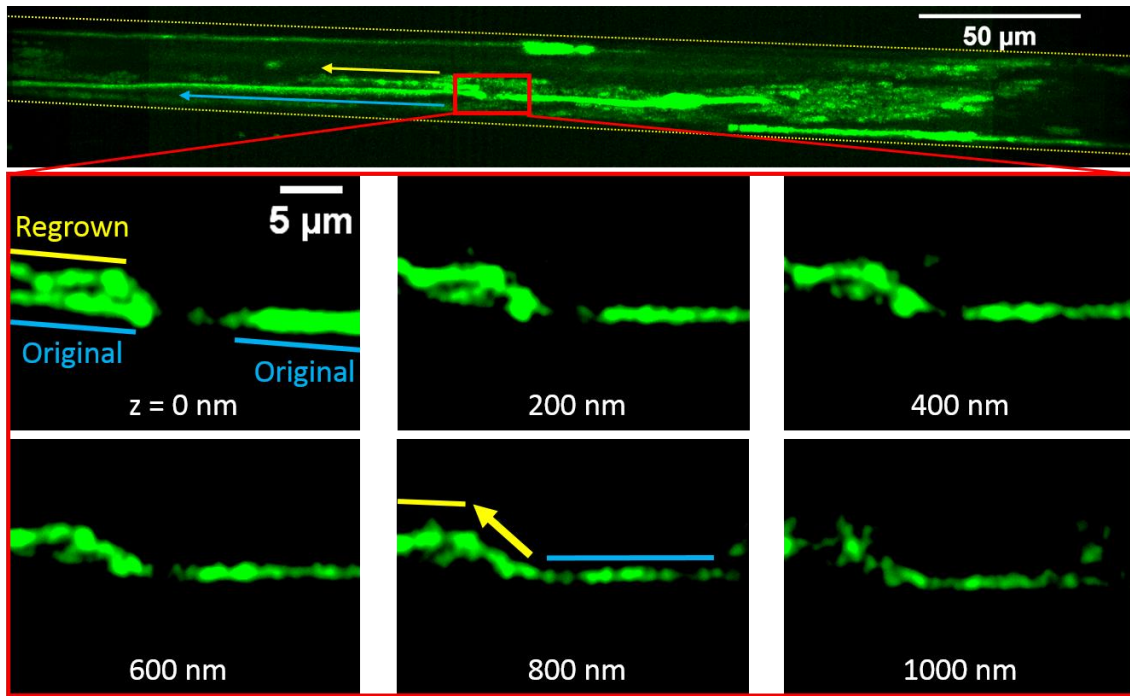
Figure 5.5: High-resolution confocal images of the regrown ALM axon without reconnection. The top image is the maximum intensity projection of the whole z-stack. The yellow dotted lines represent the trapping channel walls. The red box depicts the laser axon surgery site. The enlarged images of the surgery site is given in the bottom images. The axon regrowth direction moves upwards between z = 400 nm and 600 nm. At z = 800 nm, the original axon extends to the regrown axon on the top left while not reconnecting to the original axon on the bottom left.

Chapter 6: Planar laser activated neuronal scanning (PLANS)

6.1. INTRODUCTION

A new drug discovery demands screening of numerous drugs by applying the drugs to a huge number of model organisms. Hence, acceleration of a new drug discovery requires a novel ultrafast model organism scanning technology to reduce the time for drug screening. We developed a novel high-throughput opto-fluidics platform capable of scanning all neurons in the whole nervous system of a model organism *C. elegans* within milliseconds, which we named 'Planar Laser Activated Neuronal Scanning' (PLANS). PLANS uses a tailored light sheet to excite fluorescent protein encoded animals slice by slice, and records the fluorescent emission intensity. We analyze the recorded fluorescent intensity from the animals, and understand the status of the animals.

Our PLANS system consists of a microfluidic device, and an optical detection system. The microfluidic device comprises a loading chamber, and a narrow flow channel. Animals stay in the loading chamber until they are sent to the narrow flow channel where the single animals are optically scanned while rapidly flowing. The optical detection system generates a tailored sheet of light to excite the fluorescent protein molecules inside the neurons of the animals, and record the intensity of the fluorescent emission from the excited fluorescent protein molecules at a sampling rate high enough to complete recording a large population of animals within seconds. The microfluidic platform and the optical detection platform function in synchronization to optimize the entire scanning process, and to minimize any time loss within the process. Currently, our PLANS system is capable of scanning a single animal in 5 ms with a spatial sampling resolution of 2 μm FWHM.

6.2. EXPERIMENTS

6.2.1. Optical setup

The design of PLANS is illustrated in **Fig. 6.1**. We use a continuous wave (CW) 488 nm solid state laser (Spectra Physics, Cyan 488) as the excitation light source. We couple the laser beam into the single mode fiber (Thorlabs, P1-460B-FC-5), and collimate the laser beam output from the fiber end with the collimation lens (Thorlabs, C560TME-A, f = 13.86 mm). The single mode fiber filters unwanted non-$TEM_{0,0}$ modes out of the CW laser, and helps with shaping sharper excitation light. Then, we focus the collimated laser beam in one axis with the cylindrical lens (Thorlabs, LJ1144L1-A, f = 400 mm). We mount the cylindrical lens on the translational stage (Thorlabs, LT1) so that we can slide the cylindrical lens position to adjust the laser beam shape on the specimen. The laser beam is focused onto the animal guiding channel in the microfluidic device by the 10× objective (Olympus, 10×, 0.3 NA, dry). We tailor the focused laser beam shape by finely adjusting the cylindrical lens location relative to the objective. Our goal shape of the laser beam is the thickness of 3–4 μm, and the width of 50–80 μm as shown in **Fig. 6.1b**. The tailored laser beam excites the GFP molecules of the neurons inside the animal slice exposed to the laser beam. The excited GFP molecules emit fluorescent photons. The fluorescent photons are collected by the high NA objective (Zeiss, 63×, 1.4 NA, oil immersion), and sent out of the objective back aperture. The fluorescent photons leaving the objective back aperture are gathered by the collection lens (Thorlabs, LA1131-A, f = 50 mm), and converge into the photomultiplier tube (PMT, Hamamatsu, H10721-110). The PMT generates an electric current whose amplitude is proportional to the number fluorescent photons that the PMT receives. The electric current from the PMT is relayed to the transimpedance amplifier (preamp, Stanford Research Systems, SR570) where the electric current is converted and

amplified to the electric voltage signal. The electric voltage signal from the preamp is recorded as digital data by the high-speed data acquisition card (AlazarTech, ATS9462). The voltage signal data is saved in the storage of the PC for further analysis.
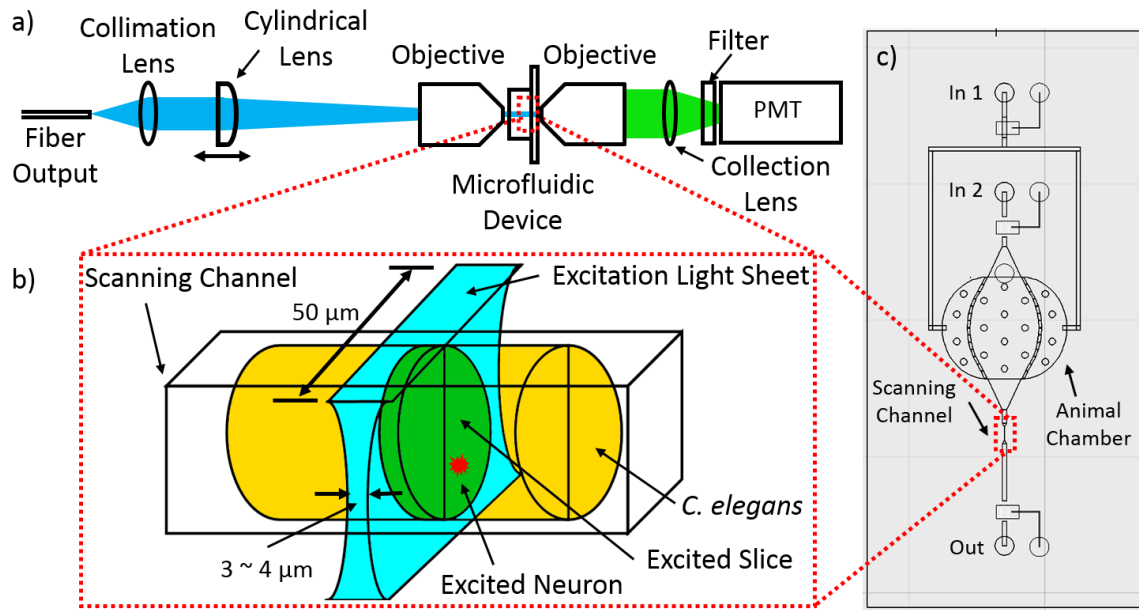
Figure 6.1: PLANS apparatus. (a) The overall optical setup of PLANS. The cylindrical lens position is adjustable for the excitation beam shape control. The blue is the excitation laser beam, and the green is the fluorescent emission. The dashed red box denotes the animal scanning region. (b) The enlarged picture of the dashed red box in (a). The thickness of the excitation light sheet is 3–4 μm, and the width is 50–80 μm. The *C. elegans* is traveling through the light sheet perpendicular to the light sheet. The yellow is the C. elegans, the green is the excited slice of *C. elegans*, the blue is the excitation light sheet, and the red is the excited neuron in the excited slice. (c) The microfluidic device for PLANS. The dashed red box is the scanning channel where the excitation laser beam passes through. The width and the depth of the scanning channel is both 40 μm.

6.2.2. Microfluidic device for scanning

We also developed the microfluidic device for PLANS shown in **Fig. 6.1c**. The core role of the microfluidic device is to guide *C. elegans* specimens to the tailored excitation

laser beam in a controlled fashion. The microfluidic device consists of two inlets, one outlet, valves to control the inlets and outlet, an animal chamber, and a scanning channel. The inlet 2 ('In 2' in **Fig. 6.1c**) is the animal entrance to the animal chamber. The animal chamber is where animals stay and wait to be sent to the imaging channel. The inlet 1 ('In 1' in **Fig. 6.1c**) allows pressured water into the animal chamber. The pressured water gently pushes animals inside the chamber to the center of the chamber. When the animal scanning begins, both of the inlets and the outlet are open, then, the pressured water propel animals to the imaging channel. While the animals travel through the scanning channel, the animals are exposed to the tailored excitation laser beam, and their fluorescent photon emission is scanned. The scanned animals lastly leave the microfluidic device through the outlet ('Out' in **Fig. 6.1c**) after passing the scanning channel.

6.2.3. Scanning laser sheet design

We conducted ZEMAX software simulation of the excitation laser beam shaping before building the optical apparatus. We first realized the 10X objective we used in our apparatus in ZEMAX based on the Olympus patent as shown in **Fig. 6.2a** [124]. We varied the back aperture filling of the objective with a 488 nm laser beam with the M^2 factor of 1.1. The simulation results are shown in **Fig. 6.2b, c**. When the back aperture filling was over 10 mm, the laser beam thickness was the thinnest being less than 2 μm. All laser beam dimensions are in e^{-2} diameter hereafter unless specified otherwise. However, the beam divergence was the most significant that the beam thickness became larger than 10 μm when the beam was ±25 μm away from the focus. This expansion of 5 times is unsuitable for the uniform excitation of the specimen. When the back aperture filling was less than 6 mm, the laser beam thickness was slightly thicker than 2 μm yet still thinner than 4 μm. Though the thickness was rather thicker than 2 μm, the divergence of the laser beam was

97

much less significant that the thickness 25 μm away from the focus was less than 7 μm. Hence, the expansion is smaller than 3 times. When the back aperture filling was 4 mm, the laser beam thickness was 3.5 μm on the focal plane, and 5.5 μm at ±25 μm distance. Based on these results, we concluded the back aperture filling for the thinner dimension should be between 4 mm and 5 mm to maintain the excitation laser beam intensity as uniform in over the height (40 μm) of the device scanning channel as possible.
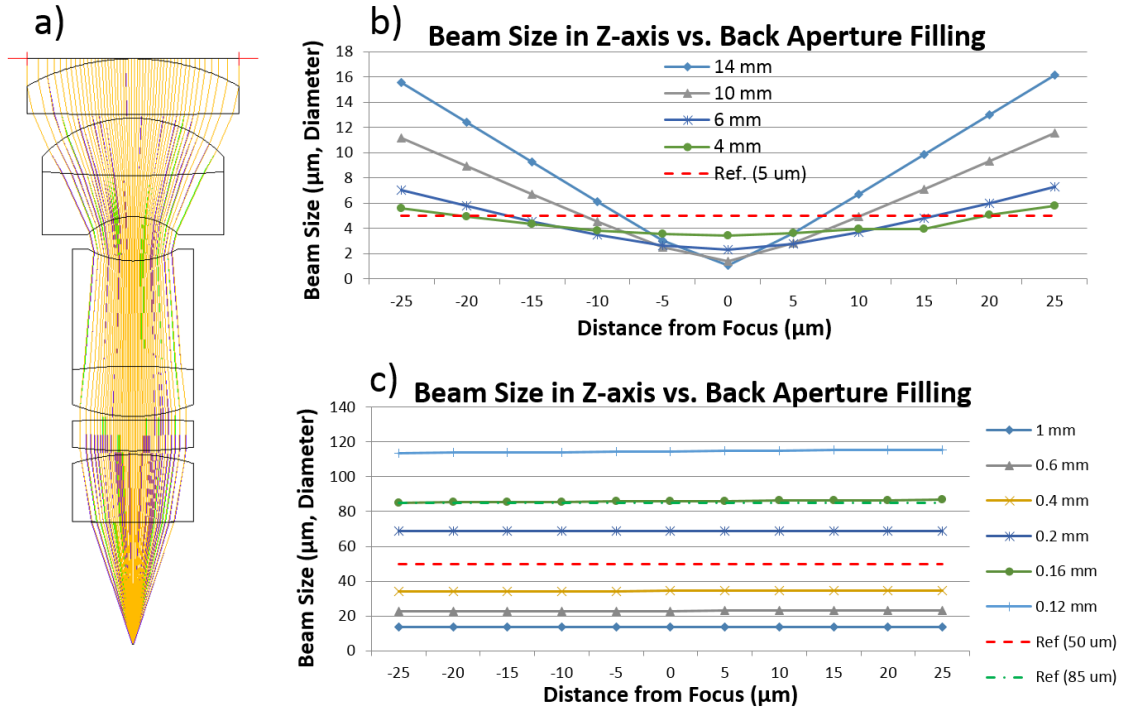
Figure 6.2: Excitation laser beam shape simulation using ZEMAX. (a) The 10X Olympus objective simulated in ZEMAX. (b) The thickness of the laser beam for various back aperture filling. The back aperture filling of 4 mm and 6 mm leads to the thickness close to the beam shape goal. (c) The width of the laser beam for various back aperture filling. The back aperture filling below 1 mm shows no width change over 50 μm distance.

The laser beam divergence disappeared when the back aperture filling was smaller than 1 mm as shown in **Fig. 6.2c**. For all back aperture fillings between 0.12 mm and 1

mm, the laser beam width remained nearly the same over 50 μm distance. The back aperture filling only changed the laser beam width. The laser beam width was 70 μm and 85 μm when the back aperture filling was 0.2 mm and 0.16 mm. The laser beam width greatly fluctuated from 35 μm to 115 μm by a miniscule adjustment of the back aperture filling from 0.4 mm to 0.12 mm. Based on those simulation results, we concluded that the back aperture filling for the laser beam width between 50 μm and 80 μm should be between 0.3 mm and 0.15 mm, and we needed a means to adjust the back aperture filling precisely because the laser beam width is sensitive to the back aperture filling. Thus, we mounted the cylindrical lens on the translational stage to control the laser beam size on the objective back aperture.

6.3. RESULTS

6.3.1. Scanning laser sheet characterization

We built the optical apparatus for PLANS based on the ZEMAX simulation result in **6.2.3**, and characterized the excitation laser beam shape. We built the optical setup in **Fig. 6.1a**. We collimated the excitation laser beam to be 4 mm e^{-2} diameter with the collimation lens. We placed a very thin layer of agarose pad mixed with a diluted fluorescein (FITC) solution at the location of the microfluidic device. We installed a CMOS camera (Allied Vision, Manta G-032C) instead of the PMT to image the excited region of the FITC agarose pad. We adjusted the location of the cylindrical lens to set the excitation laser beam width to be 80 μm. Then, we moved the FITC agarose pad along the z-axis at a 10 μm increment, and recorded the images of the fluorescent emission from the FITC agarose pad (**Fig. 6.3a**).
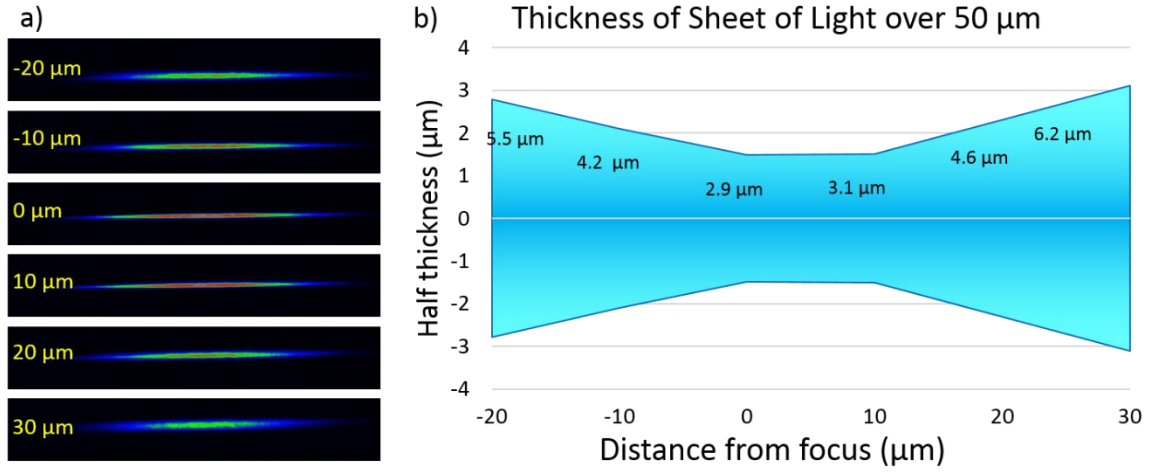
Figure 6.3: Thickness of the excitation laser beam. (a) Images of the excitation laser beam at different distances from the focal plane. The number in each image denotes the distance. (b) Plot of the excitation laser beam thickness. The numbers at each distance is the e^{-2} thickness of the laser beam at that distance. The e^{-2} width of the excitation laser beam is 80 μm.

We analyzed the recorded fluorescent emission images to characterize the excitation laser beam dimensions. We measured the pixel intensity of each of the images vertically, and curve-fit the intensity to the Gaussian distribution. We calculated the 4 deviation width (4σ) from the Gaussian curve-fits to acquire the e^{-2} width of the excitation laser beam. The calculated e^{-2} width at different distances from the focal plane is plotted in **Fig. 6.3b**. The thickness of the excitation laser beam is 3 μm being the thinnest on the focal plane. The thickness of the excitation laser beam expands to 6 μm at a 30 μm distance. Hence, the increase in the beam thickness from the focal plane to the plane at 30 μm is lower than 100%. The beam profile in **Fig. 6.3b** agrees well with the simulation result of the 4mm back aperture filling in **Fig. 6.2b**. This 3–5.5 μm excitation laser beam thickness is expected to provide the spatial scanning resolution of 1.8–3.3 μm full-width half-maximum (FWHM).

6.3.2. Sample animal scanning results

Having completed the PLANS apparatus, we conducted experiments to test the performance of the PLANS method. We prepared a group of *C. elegans* genetically encoded with AM138 strain, and the other group with AM141 strain [125]. Both AM138 and AM141 strain label the body-wall muscle cells with GFP. The difference between AM138 and AM141 is AM141 induces protein aggregation of the body-wall muscle cells, imitating Huntington's disease while AM138 does not. We took images of Day 1 adult *C. elegans* encoded with AM138 and AM141 (**Fig. 6.4a, b**), and scanned those animals with our PLANS system separately to characterize the intensity profiles of the AM138 (healthy) and AM141 (degenerate) animals.

The healthy animal intensity profile shows a fairly uniform fluorescent emission intensity level throughout the whole animal body as shown in **Fig. 6.4a**. The fluorescent emission intensity level rapidly increases from the head, reaches the intensity peak height depicting the animal's nerve ring, then decreases to the level half of the intensity peak. The intensity level covers to the peak height, and stays around the peak height until the three-fourth point of the whole animal. Reaching the tail region of the animal, the intensity level gradually drops to the no-signal level while showing a couple of spikes. Contrary to the healthy animals, the florescent emission intensity profile of the degenerate animals shows frequent fluorescent intensity spikes throughout the whole animal scanning. The intensity spikes originate from the aggregated protein molecules shown in **Fig. 6.4b** as distinctively bright green dots. The heights of the spikes are similar to one another hence, the fluorescent intensity profile shows no other distinctive features apart from the spikes. The difference between the healthy animal intensity profile and the degenerate animal intensity profile is apparent.
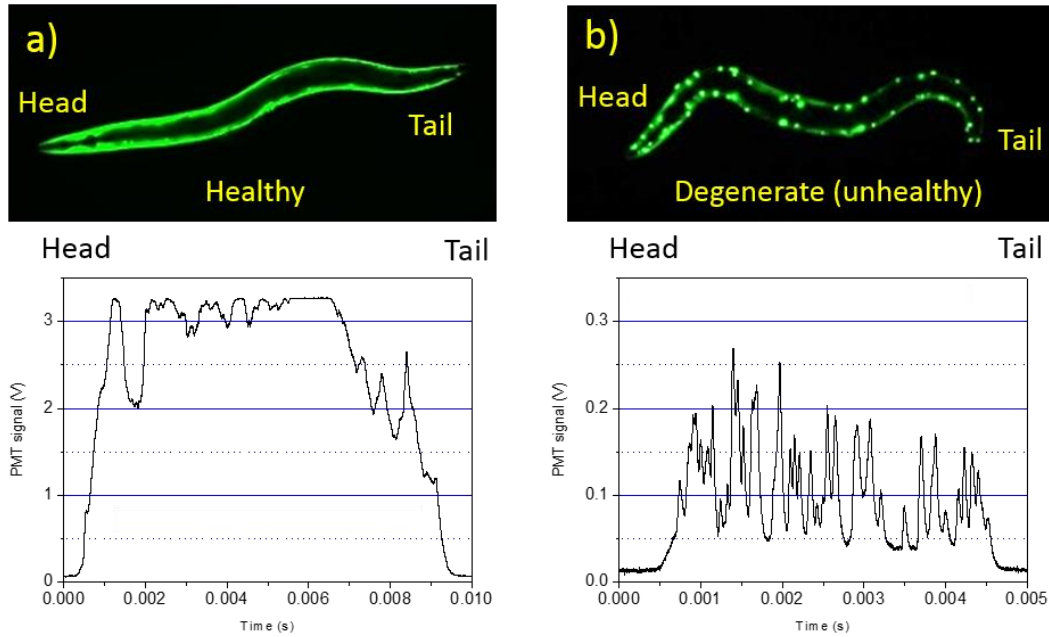
Figure 6.4: Fluorescent emission intensity profiles of healthy and unhealthy *C. elegans*. (a) The image (top) and the fluorescent intensity profile (bottom) of healthy *C. elegans* without protein aggregation. (b) The image (top) and the fluorescent intensity profile (bottom) of degenerate *C. elegans* with protein aggregation.

Having completed the individual characterization of the healthy and degenerate animal fluorescent intensity profile, we examined the scanning discernibility of our PLANS system by scanning a batch of mixed healthy and degenerate animals. We loaded approximately 20 healthy animals and 20 degenerate animals in the microfluidic scanning device, and recorded the fluorescent emission from the animals while delivering the mixed-state population through the scanning channel. We analyzed the recorded fluorescent emission intensity data, and categorized the intensity data into two groups: healthy and degenerate. We counted the numbers of the intensity profiles in the two groups and compared the numbers to the numbers of healthy and degenerate animals we initially loaded in the scanning device. We had 20 for the number of healthy animal intensity

profiles, and 20 for the number of degenerate animal intensity profiles, which match exactly the number of animals we initially loaded in the scanning device. The result confirms our PLANS can easily differentiate two different health-state animals with precision.

We also assessed the scanning speed of our PLANS system. The animal scanning took 9 ms and 5 ms in **Fig. 6.4a, b**. Considering we applied rather a weak pressure to the scanning device inlet, the one-animal scanning time can be easily reduced by applying a higher pressure. We recorded the fluorescent emission intensity with the sampling rate of 2 MS/s, hence, we generated nearly 20,000 and 10,000 data points for the 1 mm animal body length for 9 ms and 5 ms scans, respectively. Both 20,000 and 10,000 data points translate to sampling lengths of 20 nm and 40 nm per point. Even if the one animal scanning time is 1 ms, our scanning will generate 2,000 data points, and provide a sampling length of 200 nm, which is precise enough to resolve the scanning resolution of 1.8 μm FWHM.

6.4. CONCLUSION AND DISCUSSION

We designed, constructed, and characterized PLANS, a high-speed animal scanning platform for drug screening. Currently, PLANS is capable of scanning a single animal in 5 ms with a spatial sampling resolution of 2 μm FWHM. The scanning speed can be improved without sacrificing the spatial sampling resolution by optimizing the microfluidic device, and using a higher sampling rate for scanning.

The next step after improving the scanning speed is to examine various *C. elegans* disease models to select suitable models for drug screening, and to evaluate chemical compounds' effectiveness in preventing age-associated degeneration of specific neurons in the selected *C. elegans* disease models. While assessing the chemical compounds' effectiveness, we will further improve our PLANS system.

103

Current PLANS system acquires only 1D intensity profiles of animal neurons' fluorescent light emission due to the light-sheet dependent 1D scanning nature of PLANS. 1D fluorescent intensity profiles may be sufficient to assess certain disease models, nonetheless, PLANS manifests its intrinsic shortcomings. The performance of PLANS is particularly susceptible to autofluorescent signals within the specimen's body. The point detector such as the PMT used in PLANS collects all of the fluorescent light from the specimen slice excited by the excitation light sheet. Hence, PLANS cannot detect the target cell or neuron of interest if the total autofluorescent light from the excited slice dominates the fluorescent light from the cell or neuron of interest. Even if the autofluorescent light intensity does not dominate the fluorescent light from the target cell or neuron, the autofluorescent still worsens the SNR of PLANS.

In addition, the accuracy of PLANS is sensitive to the orientation of the specimen. PLANS cannot provide adequate information when the target region of the specimen does not pass through the center of the excitation light sheet because the intensity of the excitation light sheet at the edges is significantly lower than that in the center. Thus, invent of a new ultrafast 2D and 3D animal scan methods is greatly desirable. The new 2D and 3D scan methods will still have to scan a *C. elegans* within milliseconds while providing 2D and 3D image information of the neurons. The new 2D and 3D scan method will increase the accuracy and credibility of the animal scan data, and make more readily available *C. elegans* disease models feasible for high-throughput drug screening.

Chapter 7: Conclusions

In summary, we successfully developed high-speed imaging techniques for *C. elegans* nervous system studies. We first developed a high-speed laser scanning confocal microscope. The confocal microscope achieves fast imaging speed, and large field-of-views simultaneously by employing a resonant scanning mirror, and a novel hardware-software hybrid control and synchronization system. The control and synchronization system also enables flexible control of imaging conditions, and effortless system update and modification for various applications using the confocal microscope. We thoroughly explain the optical, electrical, and software principles that we used to design, and build the confocal microscope. We characterized the imaging performance of the confocal microscope. We present sample high-resolution 3-dimensional confocal images of *C. elegans* encoded with green fluorescent protein strains to demonstrate the capability of the confocal microscope.

We developed an *in vivo* functional volumetric imaging platform to study the whole animal *C. elegans* neurons' activities. The imaging platform consists of the high speed laser scanning confocal microscope we constructed, and a microfluidic device for animal immobilization and chemical stimulus delivery. We confirmed the feasibility of using the high-speed confocal microscope for functional volumetric imaging of *C. elegans* with a GFP calcium indicator. We successfully imaged *C. elegans* neurons' fluorescent signal in the whole animal with and without chemical stimulation. We managed to trace 176 neurons' activities in the whole animal for 4 minutes, and calculated the correlations among the neurons. The correlation information suggests convincing connections among neurons.

We developed a high-throughput automated confocal imaging system for *C. elegans* nerve regeneration study. The automated imaging system consists of the high-speed laser scanning confocal microscope, a microfluidic device for multiple animal

trapping, and automation software. The microfluidic device enables the high-throughput automation by simultaneously immobilizing and orienting 20 animals suitably for imaging the target region of interest in straight channels separated at regular spacing. The automation software detects the animals immobilized inside the microfluidic device, compute relative distances between two consecutive target regions, and generate a translational moving sequence for automation. The automated imaging platform completes acquiring high-resolution confocal images of the 20 animals in 10 minutes. The high-resolution confocal images successfully examine the nerve regeneration and reconnection of *C. elegans* axons after ultrafast laser surgery.

We developed the planar laser activated neuronal scanning (PLANS) system, a high-speed fluorescent animal scanning system for drug screening. The PLANS system comprises an optical setup and a microfluidic device. The optical setup excites target animals' fluorescent protein molecules, collect fluorescent signals from the animals, and record the fluorescent signals' intensity. The microfluidic device delivers the accurately defined imaging channel in strictly controlled manners. Thanks to the efficient combination of the optical setup and the microfluidic device, the PLANS system achieves scanning an animal within 5 ms with a spatial sampling resolution of 3 μm. We scanned a mixed batch of healthy and unhealthy animals of Huntington's disease model, and the scanning results demonstrate the PLANS system does screen healthy and unhealthy model animals accurately.

Our *in vivo* functional volumetric imaging platform and PLANS system have their shortcomings though they successfully accomplish their development purposes. The efficiency of the volumetric imaging platform is limited by its z-axis undersampling, and its poor SNR due to shot noise. The line scanning confocal microscope is a convincing candidate to solve the z-axis undersampling issue, and the poor SNR issue of the point

scanning confocal microscope for functional volumetric imaging. The PLANS system's performance drastically depends on the properties of the screening model specimens due to the PLANS' susceptibility to the specimen's orientation, structure, and level of autofluorescence. A new 2D or 3D animal scanning method will resolve the weakness of the current PLANS system, and be compatible with more *C. elegans* disease models.

References

[1]   M. D. Bootman, M. J. Berridge, and H. L. Roderick, "Calcium signalling: More messengers, more channels, more complexity," *Curr. Biol.*, vol. 12, no. 16, pp. 563–565, 2002.

[2]   M. J. Berridge, P. Lipp, and M. D. Bootman, "The versatility and universality of calcium signalling.," *Nat. Rev. Mol. Cell Biol.*, vol. 1, no. 1, pp. 11–21, 2000.

[3]   D. E. Clapham, "Calcium Signaling," *Cell*, vol. 131, no. 6, pp. 1047–1058, 2007.

[4]   O. H. Petersen, M. Michalak, and A. Verkhratsky, "Calcium signalling: Past, present and future," *Cell Calcium*, vol. 38, no. 3–4 SPEC. ISS., pp. 161–169, 2005.

[5]   C. Grienberger and A. Konnerth, "Imaging Calcium in Neurons," *Neuron*, vol. 73, no. 5, pp. 862–885, Mar. 2012.

[6]   R. S. Wilson, E. Segawa, P. A. Boyle, S. E. Anagnos, L. P. Hizel, and D. A. Bennett, "The natural history of cognitive decline in Alzheimer's disease," *Psychol Aging*, vol. 27, no. 4, pp. 1008–1017, 2012.

[7]   American Psychiatric Association, *Diagnostic and Statistical Manual of Mental Disorders, 5th Edition (DSM-5)*. 2013.

[8]   "2015 Alzheimer's disease facts and figures," *Alzheimer's Dement.*, vol. 11, no. 3, pp. 332–384, Mar. 2015.

[9]   L. P. O'Reilly, C. J. Luke, D. H. Perlmutter, G. a. Silverman, and S. C. Pak, "*C. elegans* in high-throughput drug discovery," *Adv. Drug Deliv. Rev.*, vol. 69–70, pp. 247–253, Apr. 2014.

[10]   S. Brenner, "Nature's gift to science (Nobel lecture)," *ChemBioChem*, vol. 4, no. 8, pp. 683–687, May 2003.

[11]   D. L. Riddle, T. Blumenthal, B. J. Meyer, and J. R. Priess, *C. elegans II*, vol. 33. 1997.

[12]   *C. elegans* sequencing consortium, "Genome sequence of the nematode *C. elegans*: a platform for investigating biology.," *Science*, vol. 282, no. 5396, pp. 2012–2018, 1998.

[13]   T. Kaletta and M. O. Hengartner, "Finding function in novel targets: *C. elegans* as a model organism.," *Nat. Rev. Drug Discov.*, vol. 5, no. 5, pp. 387–398, May 2006.

[14]   J. G. White, E. Southgate, J. N. Thomson, and S. Brenner, "The Structure of the Nervous System of the Nematode *Caenorhabditis elegans*," *Philosophical Transactions of the Royal Society B: Biological Sciences*, vol. 314, no. 1165. pp. 1–340, 1986.

[15] T. W. Harris, N. Chen, F. Cunningham, M. Tello-Ruiz, I. Antoshechkin, C. Bastiani, T. Bieri, D. Blasiar, K. Bradnam, J. Chan, C.-K. Chen, W. J. Chen, P. Davis, E. Kenny, R. Kishore, D. Lawson, R. Lee, H.-M. Muller, C. Nakamura, P. Ozersky, A. Petcherski, A. Rogers, A. Sabo, E. M. Schwarz, K. Van Auken, Q. Wang, R. Durbin, J. Spieth, P. W. Sternberg, and L. D. Stein, "WormBase: a multi-species resource for nematode biology and genomics.," *Nucleic Acids Res.*, vol. 32, no. Database issue, pp. D411–D417, 2004.

[16] E. L. Sonnhammer and R. Durbin, "Analysis of protein domain families in *Caenorhabditis elegans*.," *Genomics*, vol. 46, no. 2, pp. 200–216, 1997.

[17] C. H. Lai, C. Y. Chou, L. Y. Ch'ang, C. S. Liu, and W. Lin, "Identification of novel human genes evolutionarily conserved in *Caenorhabditis elegans* by comparative proteomics.," *Genome Res.*, vol. 10, no. 5, pp. 703–713, 2000.

[18] P. E. Kuwabara and N. O'Neil, "The use of functional genomics in *C. elegans* for studying human development and disease.," *J. Inherit. Metab. Dis.*, vol. 24, no. 2, pp. 127–138, 2001.

[19] S. Ogg, S. Paradis, S. Gottlieb, G. I. Patterson, L. Lee, H. a Tissenbaum, and G. Ruvkun, "The Fork head transcription factor DAF-16 transduces insulin-like metabolic and longevity signals in *C. elegans*.," *Nature*, vol. 389, no. 6654, pp. 994–999, 1997.

[20] L. a Harrington and C. B. Harley, "Effect of vitamin E on lifespan and reproduction in *Caenorhabditis elegans*.," *Mech. Ageing Dev.*, vol. 43, no. 1, pp. 71–78, 1988.

[21] K. D. Kimura, H. a Tissenbaum, Y. Liu, and G. Ruvkun, "daf-2, an insulin receptor-like gene that regulates longevity and diapause in *Caenorhabditis elegans*.," *Science*, vol. 277, no. 5328, pp. 942–946, 1997.

[22] C. D. Link, "Transgenic invertebrate models of age-associated neurodegenerative diseases," *Mechanisms of Ageing and Development*, vol. 122, no. 14. pp. 1639–1649, 2001.

[23] B. Westlund, G. Stilwell, and A. Sluder, "Invertebrate disease models in neurotherapeutic discovery.," *Curr. Opin. Drug Discov. Devel.*, vol. 7, no. 2, pp. 169–178, 2004.

[24] D. Levitan and I. Greenwald, "Facilitation of lin-12-mediated signalling by sel-12, a *Caenorhabditis elegans* S182 Alzheimer's disease gene.," *Nature*, vol. 377, no. 6547, pp. 351–354, 1995.

[25] N. Wittenburg, S. Eimer, B. Lakowski, S. Röhrig, C. Rudolph, and R. Baumeister, "Presenilin is required for proper morphology and function of neurons in *C. elegans*.," *Nature*, vol. 406, no. 6793, pp. 306–309, 2000.

[26] M. Lakso, S. Vartiainen, A.-M. Moilanen, J. Sirviö, J. H. Thomas, R. Nass, R. D. Blakely, and G. Wong, "Dopaminergic neuronal loss and motor deficits in

Caenorhabditis elegans overexpressing human alpha-synuclein.," *J. Neurochem.*, vol. 86, no. 1, pp. 165–172, 2003.

[27] R. Nass, D. H. Hall, D. M. Miller, and R. D. Blakely, "Neurotoxin-induced degeneration of dopamine neurons in *Caenorhabditis elegans*.," *Proc. Natl. Acad. Sci. U. S. A.*, vol. 99, no. 5, pp. 3264–3269, 2002.

[28] P. W. Faber, J. R. Alter, M. E. MacDonald, and a C. Hart, "Polyglutamine-mediated dysfunction and apoptotic death of a *Caenorhabditis elegans* sensory neuron.," *Proc. Natl. Acad. Sci. U. S. A.*, vol. 96, no. 1, pp. 179–184, 1999.

[29] E. a a Nollen, S. M. Garcia, G. van Haaften, S. Kim, A. Chavez, R. I. Morimoto, and R. H. a Plasterk, "Genome-wide RNA interference screen identifies previously undescribed regulators of polyglutamine aggregation.," *Proc. Natl. Acad. Sci. U. S. A.*, vol. 101, no. 17, pp. 6403–6408, 2004.

[30] M. F. Yanik, H. Cinar, H. N. Cinar, A. D. Chisholm, Y. Jin, and A. Ben-Yakar, "Neurosurgery: functional regeneration after laser axotomy.," *Nature*, vol. 432, no. 7019, p. 822, Dec. 2004.

[31] A. Gaud, J. M. Simon, T. Witzel, M. Carre-Pierrat, C. G. Wermuth, and L. Ségalat, "Prednisone reduces muscle degeneration in dystrophin-deficient *Caenorhabditis elegans*," *Neuromuscul. Disord.*, vol. 14, no. 6, pp. 365–370, 2004.

[32] D. J. Dickinson, J. D. Ward, D. J. Reiner, and B. Goldstein, "Engineering the *Caenorhabditis elegans* genome using Cas9-triggered homologous recombination.," *Nat. Methods*, vol. 10, no. 10, pp. 1028–34, Oct. 2013.

[33] J. G. White and W. B. Amos, "Confocal microscopy comes of age," *Nature*, vol. 328, no. 6126, pp. 183–184, Jul. 1987.

[34] J. G. White, W. B. Amos, and M. Fordham, "An evaluation of confocal versus conventional imaging of biological structures by fluorescence light microscopy.," *J. Cell Biol.*, vol. 105, no. 1, pp. 41–48, 1987.

[35] R. H. Webb, "Confocal optical microscopy," *Reports Prog. Phys.*, vol. 59, no. 3, pp. 427–471, 1999.

[36] J. B. Pawley, Ed., *Handbook of Biological Confocal Microscopy*, 3rd ed. New York: Springer US, 2006.

[37] P. J. Shaw, "Comparison of Widefield/Deconvolution and Confocal Microscopy for Three-Dimensional Imaging," in *Handbook Of Biological Confocal Microscopy*, 3rd ed., J. B. Pawley, Ed. New York: Springer US, 2006, pp. 453–467.

[38] R. A. Sweet, K. N. Fish, and D. A. Lewis, "Mapping Synaptic Pathology within Cerebral Cortical Circuits in Subjects with Schizophrenia.," *Front. Hum. Neurosci.*, vol. 4, p. 44, Jan. 2010.

[39] R. Y. Tsien, "New tetracarboxylate chelators for fluorescence measurement and photochemical manipulation of cytosolic free calcium concentrations.," *Soc. Gen. Physiol. Ser.*, vol. 40, no. 10, pp. 327–345, Jan. 1986.

[40] B. Q. Mao, F. Hamzei-Sichani, D. Aronov, R. C. Froemke, and R. Yuste, "Dynamics of spontaneous activity in neocortical slices," *Neuron*, vol. 32, no. 5, pp. 883–898, Dec. 2001.

[41] S. Kato, Y. Xu, C. E. Cho, L. F. Abbott, and C. I. Bargmann, "Temporal Responses of *C.elegans* Chemosensory Neurons Are Preserved in Behavioral Dynamics," *Neuron*, vol. 81, no. 3, pp. 616–628, 2014.

[42] J. Larsch, D. Ventimigli, C. I. Bargmann, and D. R. Albrecht, "High-throughput imaging of neuronal activity in *Caenorhabditis elegans*," *Proc. Natl. Acad. Sci. U.S.A.*, vol. 110, no. 45, pp. E4266–73, Nov. 2013.

[43] R. Prevedel, Y.-G. Yoon, M. Hoffmann, N. Pak, G. Wetzstein, S. Kato, T. Schrödel, R. Raskar, M. Zimmer, E. S. Boyden, and A. Vaziri, "Simultaneous whole-animal 3D imaging of neuronal activity using light-field microscopy.," *Nat. Methods*, vol. 11, no. 7, pp. 727–30, 2014.

[44] T. Schrödel, R. Prevedel, K. Aumayr, M. Zimmer, and A. Vaziri, "Brain-wide 3D imaging of neuronal activity in *Caenorhabditis elegans* with sculpted light.," *Nat. Methods*, vol. 10, no. 10, pp. 1013–1020, Oct. 2013.

[45] J. T. Pierce-Shimomura, B. L. Chen, J. J. Mun, R. Ho, R. Sarkis, and S. L. McIntire, "Genetic analysis of crawling and swimming locomotory patterns in *C. elegans*.," *Proc. Natl. Acad. Sci. U. S. A.*, vol. 105, no. 52, pp. 20982–20987, Dec. 2008.

[46] N. Chronis, M. Zimmer, and C. I. Bargmann, "Microfluidics for in vivo imaging of neuronal and behavioral activity in *Caenorhabditis elegans*.," *Nat. Methods*, vol. 4, no. 9, pp. 727–731, Sep. 2007.

[47] J. Ben Arous, Y. Tanizawa, I. Rabinowitch, D. Chatenay, and W. R. Schafer, "Automated imaging of neuronal activity in freely behaving *Caenorhabditis elegans*," *J. Neurosci. Methods*, vol. 187, no. 2, pp. 229–234, 2010.

[48] J. L. Donnelly, C. M. Clark, A. M. Leifer, J. K. Pirri, M. Haburcak, M. M. Francis, A. D. T. Samuel, and M. J. Alkema, "Monoaminergic Orchestration of Motor Programs in a Complex *C. elegans* Behavior," *PLoS Biol.*, vol. 11, no. 4, 2013.

[49] S. Faumont, G. Rondeau, T. R. Thiele, K. J. Lawton, K. E. McCormick, M. Sottile, O. Griesbeck, E. S. Heckscher, W. M. Roberts, C. Q. Doe, and S. R. Lockery, "An Image-Free Opto-Mechanical system for creating virtual environments and imaging neuronal activity in freely moving *Caenorhabditis elegans*," *PLoS One*, vol. 6, no. 9, 2011.

[50] D. a Clark, D. Biron, P. Sengupta, and A. D. T. Samuel, "The AFD sensory neurons encode multiple functions underlying thermotactic behavior in *Caenorhabditis elegans*.," *J. Neurosci.*, vol. 26, no. 28, pp. 7444–7451, 2006.

[51] S. H. Chalasani, N. Chronis, M. Tsunozaki, J. M. Gray, D. Ramot, M. B. Goodman, and C. I. Bargmann, "Dissecting a circuit for olfactory behaviour in *Caenorhabditis elegans*.," *Nature*, vol. 450, no. 7166, pp. 63–70, Dec. 2007.

[52] M. B. Ahrens, M. B. Orger, D. N. Robson, J. M. Li, and P. J. Keller, "Whole-brain functional imaging at cellular resolution using light-sheet microscopy," *Nat Methods*, vol. 10, no. 5, pp. 413–420, 2013.

[53] J. P. Nguyen, F. B. Shipley, A. N. Linder, G. S. Plummer, J. W. Shaevitz, and A. M. Leifer, "Whole-brain calcium imaging with cellular resolution in freely behaving *C. elegans*," vol. 3, p. 33, Jan. 2015.

[54] M. B. Bouchard, V. Voleti, C. S. Mendes, C. Lace, W. B. Grueber, R. S. Mann, R. M. Bruno, and E. M. C. Hillman, "Swept confocally-aligned planar excitation (SCAPE) microscopy for high-speed volumetric imaging of behaving organisms," *Nat. Photonics*, vol. 9, no. 2, pp. 1–22, 2015.

[55] S. X. Guo, F. Bourgeois, T. Chokshi, N. J. Durr, M. a Hilliard, N. Chronis, and A. Ben-Yakar, "Femtosecond laser nanoaxotomy lab-on-a-chip for in vivo nerve regeneration studies.," *Nat. Methods*, vol. 5, no. 6, pp. 531–533, Jun. 2008.

[56] C. Samara, C. B. Rohde, C. L. Gilleland, S. Norton, S. J. Haggarty, and M. F. Yanik, "Large-scale in vivo femtosecond laser neurosurgery screen reveals small-molecule enhancer of regeneration.," *Proc. Natl. Acad. Sci. U. S. A.*, vol. 107, no. 43, pp. 18342–18347, Oct. 2010.

[57] S. K. Gokce, S. X. Guo, N. Ghorashian, W. N. Everett, T. Jarrell, A. Kottek, A. C. Bovik, and A. Ben-Yakar, "A Fully Automated Microfluidic Femtosecond Laser Axotomy Platform for Nerve Regeneration Studies in *C. elegans*," *PLoS One*, vol. 9, no. 12, p. e113917, Dec. 2014.

[58] L. Ségalat, "Drug discovery: here comes the worm.," *ACS chemical biology*, vol. 1, no. 5. pp. 277–278, 2006.

[59] J. Giacomotto and L. Ségalat, "High-throughput screening and small animal models, where are we?," *British Journal of Pharmacology*, vol. 160, no. 2. pp. 204–216, 2010.

[60] T. C. Y. Kwok, N. Ricker, R. Fraser, A. W. Chan, A. Burns, E. F. Stanley, P. McCourt, S. R. Cutler, and P. J. Roy, "A small-molecule screen in *C. elegans* yields a new calcium channel antagonist.," *Nature*, vol. 441, no. 7089, pp. 91–5, May 2006.

[61] T. I. Moy, A. R. Ball, Z. Anklesaria, G. Casadei, K. Lewis, and F. M. Ausubel, "Identification of novel antimicrobials using a live-animal infection model.," *Proc. Natl. Acad. Sci. U. S. A.*, vol. 103, no. 27, pp. 10414–10419, 2006.

112

[62] J. Breger, B. B. Fuchs, G. Aperis, T. I. Moy, F. M. Ausubel, and E. Mylonakis, "Antifungal chemical compounds identified using a *C. elegans* pathogenicity assay," *PLoS Pathog.*, vol. 3, no. 2, pp. 0168–0178, 2007.

[63] M. Petrascheck, X. Ye, and L. B. Buck, "An antidepressant that extends lifespan in adult *Caenorhabditis elegans*.," *Nature*, vol. 450, no. 7169, pp. 553–556, Nov. 2007.

[64] S. J. Gosai, J. H. Kwak, C. J. Luke, O. S. Long, D. E. King, K. J. Kovatch, P. a. Johnston, T. Y. Shun, J. S. Lazo, D. H. Perlmutter, G. a. Silverman, and S. C. Pak, "Automated high-content live animal drug screening using *C. elegans* expressing the aggregation prone serpin ??1-antitrypsin Z," *PLoS One*, vol. 5, no. 11, p. e15460, Jan. 2010.

[65] C. K. Leung, Y. Wang, S. Malany, A. Deonarine, K. Nguyen, S. Vasile, and K. P. Choe, "An Ultra High-Throughput, Whole-Animal Screen for Small Molecule Modulators of a Specific Genetic Pathway in *Caenorhabditis elegans*," *PLoS One*, vol. 8, no. 4, 2013.

[66] L. Luo, C. V Gabel, H.-I. Ha, Y. Zhang, and A. D. T. Samuel, "Olfactory behavior of swimming *C. elegans* analyzed by measuring motile responses to temporal variations of odorants.," *J. Neurophysiol.*, vol. 99, no. 5, pp. 2617–2625, 2008.

[67] W. Shi, H. Wen, Y. Lu, Y. Shi, B. Lin, and J. Qin, "Droplet microfluidics for characterizing the neurotoxin-induced responses in individual *Caenorhabditis elegans*.," *Lab Chip*, vol. 10, no. 21, pp. 2855–2863, 2010.

[68] S. R. Lockery, S. E. Hulme, W. M. Roberts, K. J. Robinson, A. Laromaine, T. H. Lindsay, G. M. Whitesides, and J. C. Weeks, "A microfluidic device for whole-animal drug screening using electrophysiological measures in the nematode *C. elegans*," *Lab Chip*, vol. 12, no. 12, p. 2211, Jun. 2012.

[69] M. Doitsidou, N. Flames, A. C. Lee, A. Boyanov, and O. Hobert, "Automated screening for mutants affecting dopaminergic-neuron specification in *C. elegans*.," *Nat. Methods*, vol. 5, no. 10, pp. 869–872, Oct. 2008.

[70] D. C. Duffy, J. C. McDonald, O. J. A. Schueller, and G. M. Whitesides, "Rapid prototyping of microfluidic systems in poly(dimethylsiloxane)," *Anal. Chem.*, vol. 70, no. 23, pp. 4974–4984, 1998.

[71] M. C. Bélanger and Y. Marois, "Hemocompatibility, biocompatibility, inflammatory and in vivo studies of primary reference materials low-density polyethylene and polydimethylsiloxane: A review," *J. Biomed. Mater. Res.*, vol. 58, no. 5, pp. 467–477, 2001.

[72] A. Piruska, I. Nikcevic, S. H. Lee, C. Ahn, W. R. Heineman, P. A. Limbach, and C. J. Seliskar, "The autofluorescence of plastic materials and chips measured under laser irradiation.," *Lab Chip*, vol. 5, no. 12, pp. 1348–1354, 2005.

[73] M. Hamon and J. W. Hong, "New tools and new biology: Recent miniaturized systems for molecular and cellular biology," *Mol. Cells*, vol. 36, no. 6, pp. 485–506, Dec. 2013.

[74] A. Ben-Yakar, N. Chronis, and H. Lu, "Microfluidics for the analysis of behavior, nerve regeneration, and neural cell biology in *C. elegans*," *Curr. Opin. Neurobiol.*, vol. 19, no. 5, pp. 561–567, Oct. 2009.

[75] N. A. Bakhtina and J. G. Korvink, "Microfluidic laboratories for *C. elegans* enhance fundamental studies in biology," *RSC Adv.*, vol. 4, no. 9, pp. 4691–4709, Dec. 2014.

[76] S. E. Hulme, S. S. Shevkoplyas, J. Apfeld, W. Fontana, and G. M. Whitesides, "A microfabricated array of clamps for immobilizing and imaging *C. elegans*.," *Lab Chip*, vol. 7, no. 11, pp. 1515–1523, Nov. 2007.

[77] T. V. Chokshi, D. Bazopoulou, and N. Chronis, "An automated microfluidic platform for calcium imaging of chemosensory neurons in *Caenorhabditis elegans*.," *Lab Chip*, vol. 10, no. 20, pp. 2758–2763, Oct. 2010.

[78] K. Chung, M. M. Crane, and H. Lu, "Automated on-chip rapid microscopy, phenotyping and sorting of *C. elegans*.," *Nat. Methods*, vol. 5, no. 7, pp. 637–643, Jul. 2008.

[79] M. M. Crane, K. Chung, and H. Lu, "Computer-enhanced high-throughput genetic screens of *C. elegans* in a microfluidic system.," *Lab Chip*, vol. 9, no. 1, pp. 38–40, 2009.

[80] S. Mondal, S. Ahlawat, K. Rau, V. Venkataraman, and S. P. Koushika, "Imaging in vivo neuronal transport in genetic model organisms using microfluidic devices.," *Traffic*, vol. 12, no. 4, pp. 372–385, 2011.

[81] C. L. Gilleland, C. B. Rohde, F. Zeng, and M. F. Yanik, "Microfluidic immobilization of physiologically active *Caenorhabditis elegans*.," *Nat. Protoc.*, vol. 5, no. 12, pp. 1888–1902, Dec. 2010.

[82] F. Zeng, C. B. Rohde, and M. F. Yanik, "Sub-cellular precision on-chip small-animal immobilization, multi-photon imaging and femtosecond-laser manipulation.," *Lab Chip*, vol. 8, no. 5, pp. 653–656, May 2008.

[83] K. Chung and H. Lu, "Automated high-throughput cell microsurgery on-chip.," *Lab Chip*, vol. 9, no. 19, pp. 2764–2766, Oct. 2009.

[84] R. Tsien and B. Bacskai, "Video-Rate Confocal Microscopy," in *Handbook of Biological Confocal Microscopy*, 2nd ed., J. Pawley, Ed. New York: Springer US, 1995, pp. 459–478.

[85] G. Q. Xiao, T. R. Corle, and G. S. Kino, "Real-time confocal scanning optical microscope," *Appl. Phys. Lett.*, vol. 53, no. 8, pp. 716–718, 1988.

[86]   D. Toomre and J. B. B. Pawley, "Disk-Scanning Confocal Microscopy," in *Handbook of Biological Confocal Microscopy*, 3rd ed., J. B. Pawley, Ed. New York, NY: Springer US, 2006, pp. 221–238.

[87]   V. Iyer, B. E. Losavio, and P. Saggau, "Compensation of spatial and temporal dispersion for acousto-optic multiphoton laser-scanning microscopy.," *J. Biomed. Opt.*, vol. 8, no. 3, pp. 460–471, 2003.

[88]   K. H. Kim, C. Buehler, and P. T. So, "High-speed, two-photon scanning microscope.," *Appl. Opt.*, vol. 38, no. 28, pp. 6004–6009, 1999.

[89]   R. H. Webb, G. W. Hughes, and F. C. Delori, "Confocal scanning laser ophthalmoscope.," *Appl. Opt.*, vol. 26, no. 8, pp. 1492–1499, 1987.

[90]   N. Callamaras and I. Parker, "Construction of a confocal microscope for real-time x-y and x-z imaging.," *Cell Calcium*, vol. 26, no. 6, pp. 271–279, Dec. 1999.

[91]   M. Rajadhyaksha, S. González, J. M. Zavislan, R. R. Anderson, and R. H. Webb, "In vivo confocal scanning laser microscopy of human skin II: advances in instrumentation and comparison with histology.," *J. Invest. Dermatol.*, vol. 113, no. 3, pp. 293–303, Sep. 1999.

[92]   Q. T. Nguyen, N. Callamaras, C. Hsieh, and I. Parker, "Construction of a two-photon microscope for video-rate Ca(2+) imaging.," *Cell Calcium*, vol. 30, no. 6, pp. 383–393, Dec. 2001.

[93]   M. J. Sanderson and I. Parker, "Video-rate confocal microscopy," *Methods Enzymol.*, vol. 360, pp. 447–481, 2003.

[94]   M. J. Sanderson, "Acquisition of multiple real-time images for laser scanning microscopy," *Microsc. Anal.*, vol. 18, no. 4, pp. 17–23, 2004.

[95]   P. S. Tsai, N. Nishimura, E. J. Yoder, A. White, E. Dolnick, and D. Kleinfeld, "Principles, design and construction of a two-photon scanning microscope for in vitro and in vivo studies," *Methods for In Vivo Optical Imaging*. pp. 113–171, 2002.

[96]   E. H. K. Stelzer, "The intermediate optical system of laser-scanning confocal microscopes," in *Handbook of Biological Confocal Microscopy: Third Edition*, 2006, pp. 207–220.

[97]   A. J. Nichols and C. L. Evans, "Video-rate Scanning Confocal Microscopy and Microendoscopy," *J. Vis. Exp.*, no. 56, pp. 1–10, Jan. 2011.

[98]   L. Leybaert, a. De Meyer, C. Mabilde, and M. J. Sanderson, "A simple and practical method to acquire geometrically correct images with resonant scanning-based line scanning in a custom-built video-rate laser scanning microscope," *J. Microsc.*, vol. 219, no. 3, pp. 133–140, Sep. 2005.

[99] G. Y. Fan, H. Fujisaki, a Miyawaki, R. K. Tsay, R. Y. Tsien, and M. H. Ellisman, "Video-rate scanning two-photon excitation fluorescence microscopy and ratio imaging with cameleons.," *Biophys. J.*, vol. 76, no. 5, pp. 2412–2420, May 1999.

[100] M. Rajadhyaksha, R. R. Anderson, and R. H. Webb, "Video-rate confocal scanning laser microscope for imaging human tissues in vivo.," *Appl. Opt.*, vol. 38, no. 10, pp. 2105–2115, Apr. 1999.

[101] N. D. Kirkpatrick, E. Chung, D. C. Cook, X. Han, G. Gruionu, S. Liao, L. L. Munn, T. P. Padera, D. Fukumura, and R. K. Jain, "Video-rate resonant scanning multiphoton microscopy: An emerging technique for intravital imaging of the tumor microenvironment," *IntraVital*, vol. 1, no. 1, pp. 31–39, Jan. 2012.

[102] M. Born, E. Wolf, A. B. Bhatia, P. C. Clemmow, D. Gabor, A. R. Stokes, A. M. Taylor, P. A. Wayman, and W. L. Wilcock, *Principles of Optics: Electromagnetic Theory of Propagation, Interference and Diffraction of Light*, 7th ed. Cambridge University Press, 1999.

[103] A. Lipson, S. G. Lipson, and H. Lipson, *Optical Physics*, 4th ed. Cambridge University Press, 2010.

[104] S. G. Clark and C. Chiu, "*C. elegans* ZAG-1, a Zn-finger-homeodomain protein, regulates axonal development and neuronal differentiation.," *Development*, vol. 130, no. 16, pp. 3781–3794, Aug. 2003.

[105] K.-M. Chiu and C. Shu, "Simple configuration to generate short bursts of picosecond optical pulses," *Appl. Opt.*, vol. 34, no. 18, pp. 3431–3435, 1995.

[106] N. Ji, J. C. Magee, and E. Betzig, "Passive Pulse Splitters," *Pulse*, vol. 5, no. 2, pp. 197–202, 2008.

[107] N. Ji, J. C. Magee, and E. Betzig, "High-speed, low-photodamage nonlinear imaging using passive pulse splitters.," *Nat. Methods*, vol. 5, no. 2, pp. 197–202, Feb. 2008.

[108] Y. Wu, a. Ghitani, R. Christensen, a. Santella, Z. Du, G. Rondeau, Z. Bao, D. Colon-Ramos, and H. Shroff, "Inverted selective plane illumination microscopy (iSPIM) enables coupled cell identity lineaging and neurodevelopmental imaging in *Caenorhabditis elegans*," *Proc. Natl. Acad. Sci.*, vol. 108, no. 43, pp. 17708–17713, 2011.

[109] T. Panier, S. A. Romano, R. Olive, T. Pietri, G. Sumbre, R. Candelier, and G. Debrégeas, "Fast functional imaging of multiple brain regions in intact zebrafish larvae using selective plane illumination microscopy.," *Front. Neural Circuits*, vol. 7, p. 65, Jan. 2013.

[110] R. K. Chhetri, F. Amat, Y. Wan, B. Hockendorf, W. C. Lemon, P. J. Keller, B. Höckendorf, W. C. Lemon, and P. J. Keller, "Whole-animal functional and developmental imaging with isotropic spatial resolution," *Nat Meth*, vol. 12, no. 12, pp. 1171–1178, Dec. 2015.

[111] J. P. Nguyen, F. B. Shipley, A. N. Linder, G. S. Plummer, M. Liu, and S. U. Setru, "Whole-brain calcium imaging with cellular resolution in freely behaving *Caenorhabditis elegans*," pp. 1–8, 2015.

[112] V. Venkatachalam, N. Ji, X. Wang, C. Clark, J. K. Mitchell, M. Klein, C. J. Tabone, J. Florman, H. Ji, J. Greenwood, A. D. Chisholm, J. Srinivasan, M. Alkema, M. Zhen, and A. D. T. Samuel, "Pan-neuronal imaging in roaming *Caenorhabditis elegans*," *Proc. Natl. Acad. Sci.*, p. 201507109, 2015.

[113] L. Kong, J. Tang, J. P. Little, Y. Yu, T. Lämmermann, C. P. Lin, R. N. Germain, and M. Cui, "Continuous volumetric imaging via an optical phase-locked ultrasound lens.," *Nat. Methods*, vol. 12, no. 8, pp. 759–62, Aug. 2015.

[114] M. a Unger, H. P. Chou, T. Thorsen, a Scherer, and S. R. Quake, "Monolithic microfabricated valves and pumps by multilayer soft lithography.," *Science*, vol. 288, no. 5463, pp. 113–116, Apr. 2000.

[115] J. Melin and S. R. Quake, "Microfluidic large-scale integration: the evolution of design rules for biological automation.," *Annu. Rev. Biophys. Biomol. Struct.*, vol. 36, pp. 213–231, Jan. 2007.

[116] T. Stiernagle, "Maintenance of *C. elegans*," *C. elegans*, vol. 2, pp. 51–67, 1999.

[117] P. Kaifosh, M. Lovett-Barron, G. F. Turi, T. R. Reardon, and A. Losonczy, "Septo-hippocampal GABAergic signaling across multiple modalities in awake mice.," *Nat. Neurosci.*, vol. 16, no. 9, pp. 1182–4, Sep. 2013.

[118] P. Kaifosh, J. D. Zaremba, N. B. Danielson, and A. Losonczy, "SIMA: Python software for analysis of dynamic fluorescence imaging data.," *Front. Neuroinform.*, vol. 8, p. 80, Jan. 2014.

[119] D. A. Dombeck, A. N. Khabbaz, F. Collman, T. L. Adelman, and D. W. Tank, "Imaging large-scale neural activity with cellular resolution in awake, mobile mice.," *Neuron*, vol. 56, no. 1, pp. 43–57, Oct. 2007.

[120] N. Campbell, "The study of discontinuous phenomena," in *Proc. Camb. Phil. Soc*, 1909, vol. 15, no. 117, p. 310.

[121] W. Schottky, "Regarding spontaneous current fluctuation in different electricity conductors," *Ann. Phys.*, vol. 57, no. 23, pp. 541–567, 1918.

[122] C. M. Caves, "Quantum limits on noise in linear amplifiers," *Phys. Rev. D*, vol. 26, no. 8, p. 1817, 1982.

[123] R. Wolleschensky, B. Zimmermann, and M. Kempe, "High-speed confocal fluorescence imaging with a novel line scanning microscope.," *J. Biomed. Opt.*, vol. 11, no. 6, p. 064011, Jan. 2006.

[124] T. Tojo and T. Uetake, "Objective lens system for microscopes," U.S. Patent: 4,227,773, 1980.

[125] J. F. Morley, H. R. Brignull, J. J. Weyers, and R. I. Morimoto, "The threshold for polyglutamine-expansion protein aggregation and cellular toxicity is dynamic and influenced by aging in *Caenorhabditis elegans*.," *Proc. Natl. Acad. Sci. U. S. A.*, vol. 99, no. 16, pp. 10417–10422, 2002.